

Universidade de São Paulo
Instituto de Astronomia, Geofísica e Ciências Atmosféricas
Departamento de Astronomia

Lucas Barreto Mota dos Santos

**Star Forming Regions and
Magnetohydrodynamic Turbulence
Connections**

São Paulo

2020

Lucas Barreto Mota dos Santos

Star Forming Regions and Magnetohydrodynamic Turbulence Connections

Tese/Dissertação apresentada ao Departamento de Astronomia do Instituto de Astronomia, Geofísica e Ciências Atmosféricas da Universidade de São Paulo como requisito parcial para a obtenção do título de Mestre/Doutor em Ciências. Versão corrigida. O original encontra-se disponível na unidade.

Área de Concentração: Astronomia

Orientador(a): Prof.^(a) Dr.^(a) Elisabete M. de Gouveia Dal Pino

São Paulo

2020

To my parents.

Acknowledgements

I would like to thank, first and foremost, my parents, Humberto and Cibele, for all the love and support without which this work would not be possible.

I want to thank my colleagues, especially Luis Kadowaki, for all the constructive discussions, and Professor Blakesly Burkhart for welcoming me to the Center for Computational Astrophysics (CCA) and for allowing me to use their resources. I also thank Professors Reinaldo Santos-Lima, and Claudio Melioli for providing the modified version of the code AMON including self-gravity.

I want to thank my advisor, Prof. Elisabete M. de Gouveia Dal Pino, for her patience, guidance and understanding.

Also, I want to thank CAPES and FAPESP, under project number: 2013/10559-5, for the financial support.

Resumo

Sabe-se que estrelas se formam dentro de nuvens moleculares, a partir do colapso gravitacional. Ao mesmo tempo, acredita-se que a formação e manutenção destas estruturas seja feita pelos movimentos turbulentos do fluido magnetizado dentro destas nuvens. Neste trabalho nós exploramos, através de simulações numéricas tridimensionais (3D) e diferentes métodos estatísticos, incluindo PDF (Função Densidade de Probabilidade), PRS (Estatística de Rayleigh Projetada), e o espectro de potências, como a turbulência magnetohidrodinâmica (MHD) está conectada à formação de nuvens moleculares. Nós inicialmente introduzimos turbulência em um meio homogêneo isotérmico permeado por um campo magnético uniforme, considerando diferentes regimes que vão desde transônico até supersônico, e de sub-Alfvénico a super-Alfvénico. Nós consideramos duas principais famílias de modelos, uma sem auto-gravidade e outra incluindo a auto-gravidade no gás, a fim de explorar o colapso das estruturas no domínio da nuvem molecular. Nossos principais resultados podem ser resumidos da seguinte forma: (i) Há uma clara correlação entre os gradientes de densidade (e densidade colunar) com o campo magnético em sistemas sub-Alfvénicos com e sem auto-gravidade, com regiões menos densas aparecendo mais alinhadas com o campo magnético e regiões mais densas aparecendo mais perpendiculares com o campo magnético. Esta diferença é maior para números de Mach sônicos maiores, que causam uma maior fragmentação das nuvens; (ii) Modelos super-Alfvénicos sem auto-gravidade apresentam a maioria das estruturas paralelas ao campo magnético, devido à predominância dos efeitos de compressão, sem uma dependência importante com o número de Mach sônico; (iii) Em modelos sub-Alfvénicos, verificou-se que a direção da linha de visada (em inglês, LOS) influencia a distribuição das componentes projetadas do campo magnético no plano céu (\mathbf{B}_\perp). Este mostra menos coerência quando a LOS é paralela ao

campo magnético inicial. Ainda assim, regiões menos densas aparecem predominantemente paralelas a \mathbf{B}_\perp e regiões mais densas aparecem mais perpendiculares a ele, especialmente quando auto-gravidade é considerada; (iv) Para modelos super-Alfvénicos, as estruturas presentes nos mapas de densidade colunar aparecem maioritariamente alinhadas a \mathbf{B}_\perp e os mapas apresentam um comportamento bastante similar em diferentes LOS (i.e., paralelo a, perpendicular, ou com um ângulo de 45° em relação ao campo inicial); (v) A introdução da auto-gravidade aumenta a formação de estruturas densas perpendiculares ao campo magnético (já que forças gravitacionais forçam o colapso da matéria mais facilmente ao longo das linhas), principalmente em modelos sub-Alfvénicos. Este efeito em modelos super-Alfvénicos fica mais aparente apenas para números de Mach sônicos maiores; (vi) A comparação dos resultados obtidos em nossos modelos com observações feitas por *Planck*, *Herschel* e BLASTPol, indicam que os nossos modelos sub-Alfvénicos podem, qualitativamente, reproduzir melhor as características de nuvens observadas. Não apenas o comportamento do PRS observado, mas também a coerência geral do campo do campo magnético projetado \mathbf{B}_\perp é compatível com nossos modelos sub-Alfvénicos para a maior parte das nuvens. Há nuvens em que as torções de \mathbf{B}_\perp observadas podem ser explicadas com efeitos relacionados à direção da LOS. Nuvens como Aquila, por exemplo, podem ser bem representadas por modelos sem auto-gravidade ou em estágios iniciais de colapso, enquanto que Taurus e Vela C possuem similaridades com modelos em um estágio mais avançado de colapso gravitacional.

Abstract

Stars are known to form inside molecular clouds, out of gravitational collapse. On the other hand, the formation and maintenance of these interstellar structures is believed to be driven by turbulent motions of the magnetized fluid inside these clouds. In this work we explore, by means of three-dimensional (3D) numerical simulations and different statistical methods, including PDF (Probability Density Function), PRS (Projected Rayleigh Statistics), and power-spectrum analyses, how magnetohydrodynamical (MHD) turbulence is connected to the formation of star forming regions. We drive turbulence in an initially homogeneous isothermal environment permeated by uniform magnetic field, considering different regimes that go from transonic to supersonic, and sub-Alfvénic to super-Alfvénic turbulence. We consider two main families of models, one without self-gravity and the other including self-gravity in the gas in order to explore the collapse of structures into the molecular cloud domain. Our main results can be summarized as follows: (i) There is a clear correlation between the gradients of density (and column density) with the magnetic field orientation for sub-Alfvénic systems with and without self-gravity, with less dense regions appearing more aligned to the magnetic field and denser regions appearing more perpendicular to magnetic field. This difference is enhanced for higher sonic Mach numbers, which cause more fragmentation of the clouds; (ii) Super-Alfvénic models without self-gravity show structures mostly aligned to the magnetic field, due to dominance of the compression effects, with no important dependence with the sonic Mach number; (iii) In sub-Alfvénic models, the direction of the line-of-sight (LOS) of the integrated column density is found to influence the distribution of the projected component of the magnetic field on the plane of the sky (\mathbf{B}_\perp). This shows less coherence when the LOS is parallel to the initial magnetic field. Still, less dense regions appear predominantly parallel to \mathbf{B}_\perp and

denser regions appear more perpendicular to it, specially when self-gravity is considered; (iv) For the super-Alfvénic models, column density structures also appear mostly aligned to \mathbf{B}_\perp and maps yield very similar behaviour for different LOS (i.e., parallel, perpendicular, or making an angle of 45° with the initial field); (v) The introduction of self-gravity enhances the formation of dense structures perpendicular to the magnetic field (as gravitational forces enforce the collapse of matter more easily along the lines), mainly in sub-Alfvénic models. This effect in super-Alfvénic models only becomes more pronounced for high sonic Mach numbers; (vi) The comparison of the results obtained from our models with observations by *Planck*, *Herschel* and BLASTPol, indicates that our sub-Alfvénic models can qualitatively better reproduce the characteristics of observed clouds. Not only the behaviour of the observed PRS, but also the general coherence of the projected magnetic field \mathbf{B}_\perp is compatible with our sub-Alfvénic models for most clouds. There are clouds where twists of \mathbf{B}_\perp could be explained with effects related to the direction of the LOS. Clouds like Aquila, for instance, can be well represented by models with no self-gravity or in earlier stages of collapse, while Taurus and Vela C have some similarities with models at a more advanced stage of gravitational collapse.

List of Figures

2.1	Scheme of the vectors that are considered to calculate the angle ϕ between the density gradient of N_H and the polarization pseudo-vector (\mathbf{E}) for column density maps. (Adapted from Planck Collaboration et al. (2016)) . . .	42
2.2	Comparison of column density distribution for two models with same initial conditions and different resolution. On the left side, 256^3 cells were used. On the right side 512^3 cells were used. Note that the higher resolution allows for a higher fragmentation of the structures, but the results are still similar. The dashed lines represent the direction of the projected magnetic field onto the plane of the sky (see more details on the text).	44
2.3	Comparison of the power spectrum for the same models of Figure 2.2. On the left side, 256^3 cells were used. On the right side, 512^3 cells were used. The red dashed line represents the Kolmogorov power-law ($k^{[Pleaseinsertintopreamble]11/3}$, in the 3D case) for reference.	44
3.1	Column density maps of the initial ($t = 0.0t_{ff}$) and final ($t = 0.3t_{ff}$) states of model <i>Ms7.0_Ma0.6_grav</i> with $\mathcal{M}_s = 7$ and $\mathcal{M}_A = 0.6$ along three different LOS. From top to bottom the LOS is perpendicular, makes an angle of 45° , and is parallel to the initial magnetic field, respectively. The magnetic field is represented by the line pattern using a LIC method. $t = 0.0t_{ff}$ (on the left) corresponds to the time when turbulence has fully developed in the system and is in nearly steady state, right before gravity is turned-on in the system. Thus, the left diagrams correspond to the system without gravity, while the right-diagrams represent the system with self-gravity at an evolved time.	48

3.2	The same as in Figure 3.1, but for the super-Alfvénic model with $\mathcal{M}_A = 2$.	49
3.3	Comparison of the 3D PDF of density between turbulent models with no self-gravity (solid lines) and the initial state of the corresponding model with self-gravity (dashed line). The sub-Alfvénic models are presented on the left and the super-Alfvénic ones are presented on the right side.	50
3.4	Comparison of the 3D distribution of density and magnetic fields for the initial ($t = 0.0t_{ff}$)(without self-gravity) and final ($t = 0.3t_{ff}$) states (with gravity) for models <i>Ms7.0_Ma0.6_grav</i> (top) and <i>Ms7.0_Ma2.0_grav</i> (bottom). See text for details.	51
3.5	Time evolution of the density PDF for models <i>Ms7.0_Ma0.6_grav</i> (left) and <i>Ms7.0_Ma2.0_grav</i> (right). The green vertical dashed line indicates the critical density for star formation (eq. 2.14). The magenta vertical dashed line represents the transition density as defined in eq. 2.11. The black dashed line and the red dashed-dotted line are the fitted lognormal and power-law to $t = 0.3t_{ff}$, respectively.	53
3.6	3D power spectrum of density for models with $\mathcal{M}_s = 7.0$ that do consider self-gravity. On the left we have $\mathcal{M}_A = 0.6$ and on the right we have $\mathcal{M}_A = 2.0$. The red dashed line represents the Kolmogorov power-law ($k^{-11/3}$) for reference.	55
3.7	1D power spectrum of column density for models with $\mathcal{M}_s = 7.0$ that do consider self-gravity along three LOS. The direction along which the map was integrated is indicated above each plot. On the left we have $\mathcal{M}_A = 0.6$ and on the right we have $\mathcal{M}_A = 2.0$. The red dashed line represents the Kolmogorov power-law ($k^{-5/3}$) for reference.	56
3.8	PRS time evolution for all sub-Alfvénic models (with $\mathcal{M}_A = 0.7$) without self-gravity. From left to right the PRS is applied to the LOS along Z (the direction perpendicular to the initial field), XZ (45° with regard to the initial field) and X (perpendicular to the initial field) directions. From top to bottom initial $\mathcal{M}_s = 2.0, 4.0, 7.0$, respectively.	59

3.9	Column density maps with LIC method applied to \mathbf{B}_\perp for the same models presented in Figure 3.8. The time $t = 600c.u.$ was used to illustrate what is seen in these integrated maps of Figure 3.8. From left to right the integrated LOS is along Z (the direction perpendicular to the initial field), XZ (45° with regard to the initial field) and X (perpendicular to the initial field) directions. From top to bottom initial $\mathcal{M}_s = 2.0, 4.0$ and 7.0 , respectively.	60
3.10	PRS time evolution for all super-Alfvénic (with $\mathcal{M}_A = 2.0$) models without self-gravity. From left to right the PRS is applied along Z (the direction perpendicular to the initial field), XZ (45° with regard to the initial field) and X (perpendicular to the initial field) directions. From top to bottom initial $\mathcal{M}_s = 2.0, 4.0$ and 7.0 , respectively.	61
3.11	Column density maps with LIC method applied to \mathbf{B}_\perp for the same models presented in Figure 3.10. The time $t = 600c.u.$ was used to illustrate what is seen in these integrated maps. From left to right the column density distribution is integrated along Z (the direction perpendicular to the initial field), XZ (45° with regard to the initial field) and X (perpendicular to the initial field) defined directions. From top to bottom initial $\mathcal{M}_s = 2.0, 4.0$ and 7.0 , respectively.	62
3.12	Z_B analysis (equation 2.21) applied to the 3D distribution of density and magnetic fields for all simulated models without self-gravity (see table 2.1) for 3 different. On the left are presented the sub-Alfvénic (initial $\mathcal{M}_A = 0.7$), and on the right super-Alfvénic (initial $\mathcal{M}_A = 2.0$) models. From top to bottom initial $\mathcal{M}_s = 2.0, 4.0$ and 7.0 , respectively.	63
3.13	Histograms of $\cos(\phi)$ (eq. 2.15, section 2.2) for different bins of density for the sub-Alfvénic (left) and super-Alfvénic (right) models without self-gravity. Only bins 1^{st} , 10^{th} , 17^{th} , 18^{th} , 19^{th} and 20^{th} are shown.	66
3.14	Z_B analysis (equation 2.21) applied to the 3D distribution of density and magnetic fields for all simulated models with self-gravity (see table 2.1). On the left are presented the sub-Alfvénic (initial $\mathcal{M}_A = 0.6$) and on the right, super-Alfvénic (initial $\mathcal{M}_A = 2.0$) models. From top to bottom initial $\mathcal{M}_s = 2.0, 4.0$ and 7.0 , respectively. The green dashed line indicates the critical density for star-formation (eq. 2.14).	68

3.15	Histograms of $\cos(\phi)$ (eq. 2.15, see section 2.2) for different bins of density for the sub-Alfvénic (initial $\mathcal{M}_A = 0.6$, left) and super-Alfvénic (initial $\mathcal{M}_A = 2.0$, right) models with self-gravity. Only bins 1 st , 10 th , 17 th , 18 th , 19 th and 20 th are shown.	69
3.16	PRS time evolution for all sub-Alfvénic (with $\mathcal{M}_A = 0.6$) models with self-gravity. From left to right the PRS is applied along Z (the direction perpendicular to the initial field), XZ (45° with regard to the initial field) and X (perpendicular to the initial field) directions. From top to bottom initial $\mathcal{M}_s = 2.0, 4.0$ and 7.0 , respectively.	70
3.17	Column density maps with LIC method applied to \mathbf{B}_\perp for the same sub-Alfvénic models with self-gravity presented in Figure 3.16. The time considered for each map is indicated above each diagram. From left to right the integration is along X (the direction perpendicular to the initial field), XZ (45° with regard to the initial field) and Z (perpendicular to the initial field) defined directions. From top to bottom initial $\mathcal{M}_s = 1.8, 4.0$ and 7.0 , respectively.	72
3.18	PRS time evolution for all super-Alfvénic (with $\mathcal{M}_A = 2.0$) models with self-gravity. From left to right the PRS is applied along Z (the direction perpendicular to the initial field), XZ (45° with regard to the initial field) and X (perpendicular to the initial field) directions. From top to bottom initial $\mathcal{M}_s = 2.0, 4.0$ and 7.0 , respectively.	73
3.19	Column density maps with LIC method applied to \mathbf{B}_\perp for the same super-Alfvénic models with self-gravity presented in Figure 3.18. The time considered for each map is indicated above each diagram. From left to right the integration is along X (the direction perpendicular to the initial field), XZ (45° with regard to the initial field) and Z (perpendicular to the initial field) defined directions. From top to bottom initial $\mathcal{M}_s = 1.8, 4.0$ and 7.0 , respectively.	74

3.20	Histograms of $\cos(\phi)$ (eq. 2.15, see section 2.2) for different bins of density for the sub-Alfvénic (initial $\mathcal{M}_A = 0.6$, top) and super-Alfvénic (initial $\mathcal{M}_A = 2.0$, down) models with self-gravity. The initial time $t = 0.0t_{ff}$ is presented on the left, and the final state $t = 0.3t_{ff}$ on the right side. Only bins 1 st , 10 th , 17 th , 18 th , 19 th and 20 th are shown.	77
3.21	Density PDF's of all models with self-gravity. The top diagrams show the sub-Alfvénic and the bottom ones, the super-Alfvénic models. On the left, $t = 0.0t_{ff}$ is shown. On the right, $t = 1.2t_{ff}, 0.4t_{ff}$ and $0.3t_{ff}$ is considered for $\mathcal{M}_s = 1.8, 4.0$ and 7.0 , respectively. The dashed vertical lines are the critical density for star formation according to equation 2.14 for each of the models.	78
4.1	Column density map of the entire sky observed by <i>Planck</i> at 353 GHz. Black squares indicate the location of the molecular clouds observed. Extracted from Planck Collaboration et al. (2016).	83
4.2	Column density map of Vela C observed by Herschel using SPIRE and PACS instruments and projected magnetic (line pattern produced using a LIC method) field derived from BLAST-Pol observations. Extracted from Soler et al. (2017).	84
4.3	Top: Z_E (eq. 2.21) calculated from observations (Planck Collaboration et al. (2016); Soler et al. (2017)). Bottom: Z_E (eq. 2.21) calculated from our simulated models considering all LOS for models with $\mathcal{M}_s = 4$ and 7 . The PRS when only turbulence is presented on the left. The PRS calculated for the final state of models that consider self-gravity is shown on the right. The Alfvénic Mach number of the models is indicated above each plot. . .	86
4.4	Left: Column density maps overlaid with the estimated magnetic field direction estimated from the polarization observations at 353 GHz from <i>Planck</i> Satellite from Aquila and Chamaeleon-Musca. Right: Histogram of relative orientations similar to what was presented in Figure 3.20. Extracted from Planck Collaboration et al. (2016).	87

4.5	Left: Column density maps overlaid with the estimated magnetic field direction estimated from the polarization observations at 353 GHz from <i>Planck</i> Satellite from Taurus and Ophiuchus. Right: Histogram of relative orientations similar to what was presented in Figure 3.20. Extracted from Planck Collaboration et al. (2016).	88
4.6	Left: Column density map along LOS XZ for our model <i>Ms1.8-Ma2.0-grav</i> (top) and the PRS calculated for the respective map (bottom). Right: Same map, but convolved with a Gaussian kernel in a similar processes to the one made for observations from Planck Collaboration et al. (2016) (top) and the PRS of the respective map (bottom) (see also Soler et al. (2013) for further details).	91
4.7	<i>Herschel</i> /SPIRE 250 μm image of B211/B213/L1495 region in Taurus. On the left-hand side, filaments B211 and B213 are highlighted by the light blue and purple curves. On the right-hand side, the green lines represent the magnetic field direction derived from optical and infrared polarization vectors. Blue curves represents striations, less dense filaments perpendicular to the main filament B211/B213, which is represented by the black line. The diagram on the lower right corner represent the average position of the polarization angles, low-density striations and the main filament, respectively. Extracted from Palmeirim et al. (2013)	92
4.8	Time evolution of zoomed-in regions extracted from models <i>Ms7.0-Ma0.6-grav</i> (left) and <i>Ms7.0-Ma2.0-grav</i> (right). Both maps were integrated along LOS XZ (45° inclined with respect to the initial magnetic field). The time considered is indicated above each map.	93
4.9	Time evolution of the PRS analysis (Z_E , eq. 2.21) for the same maps presented in Figure 4.8. Solid lines represent the PRS along time calculated from our models, sub-Alfvénic on the left-hand side and super-Alfvénic on the right hand side. Dashed lines represent the observed PRS of some regions presented in the top diagram of Figure 4.3.	94

A.1	Multigrid cycle scheme. S denotes the smoothing process, E denotes the exact solution in the coarsest grid. Starting on the left, each line downwards represents a restriction (\mathcal{R}) and each line upwards represents a prolongation (\mathcal{P}). For V-cycles ($\gamma = 1$), E represents one two-grid iteration each time the number of grid levels is increased by one. For the W-cycles ($\gamma = 2$), each E step gets replaced by two two-grid iterations. Extracted from Press et al. (2002).	116
B.1	Comparison of the 3D PDF of density between turbulent models with no self-gravity (solid lines) and the initial state of the corresponding model with self-gravity (dashed line). The sub-Alfvénic models are presented on the left and the super-Alfvénic ones are presented on the right side. Similar to what is presented in Figure 3.3	118
B.2	3D power spectrum of density for models with $\mathcal{M}_s = 1.8$ and 4.0 that consider self-gravity. On the left we have $\mathcal{M}_a = 0.6$ and on the right we have $\mathcal{M}_a = 2.0$. The red dashed line represents the Kolmogorov power-law ($k^{-11/3}$) for reference. Similar to Figure B.3.	119
B.3	3D power spectrum of density for models all the models that do not consider gravity, similar to Figures B.3 and B.2. On the left we have $\mathcal{M}_a = 0.6$ and on the right we have $\mathcal{M}_a = 2.0$. The red dashed line represents the Kolmogorov power-law ($k^{-11/3}$) for reference.	120

List of Tables

2.1	Initial conditions for all simulated models, with and without self-gravity . . .	46
-----	--	----

Contents

1. <i>Introduction</i>	23
1.1 Molecular Clouds	23
1.2 MHD turbulence in Molecular Clouds	27
1.2.1 Hydrodynamic Turbulence	27
1.2.2 MHD turbulence	29
1.3 The aim of this work	31
2. <i>Methodology</i>	33
2.1 Turbulence vs Gravity - Triggering star formation	35
2.2 Quantifying the relative orientation between structures and the magnetic field	38
2.2.1 Projected Rayleigh statistics (PRS)	41
2.3 Boundary and initial conditions	43
3. <i>Results of the numerical simulations</i>	47
3.1 General characteristics of the simulated models	47
3.2 Simulations without self-gravity	58
3.3 Simulations with self-gravity	66
3.3.1 Turbulence, gravity and magnetic field interlinks	74
3.4 Summary of the results	78
4. <i>Comparison of the models with Observations</i>	83
4.1 Introduction	83
4.2 PRS and angular distribution analysis	85
4.3 A closer look inside the Molecular Clouds	90

5. <i>Conclusions and Future Perspectives</i>	97
5.1 A summary of our findings	97
5.2 Results from previous studies in the literature	99
5.3 Future perspectives	100
<i>Bibliography</i>	101
<i>Appendix</i>	109
A.	111
A.1 Godunov Method	111
A.2 Multigrid Method to solve th Poisson equation	113
B. <i>Other models</i>	117

Introduction

In our galaxy, it is known that stars form inside molecular clouds. Over the decades, many observations have been made, but the processes related both to the formation of these clouds and the stars are not yet fully understood. In this chapter, it will be discussed the main characteristics of these regions and what mechanisms are believed to be dominant during their formation.

1.1 Molecular Clouds

When looking at the sky, there are several dark structures opaque to optical light throughout our galaxy. These giant clouds come in various shapes and sizes, often being associated with the birth of stars. Clouds like Perseus, Ophiucus and Taurus, for instance, are mostly composed by molecules and opaque due to the presence of dust grains that absorb optical starlight.

The dust has a temperature that varies between $\sim 12\text{K}$, inside cores, and $\sim 20\text{K}$, in less dense regions, while the gas temperature in the less dense regions has a temperature $\sim 5\text{K}$ to $\sim 10\text{K}$. In the low density regions, dust temperature is mainly regulated by the equilibrium between the heating coming from the interstellar radiation field and the cooling due to thermal radiation in the far-IR. At the same time, the low density gas temperature is balanced by the heating from the ionization of cosmic rays and the cooling due to line emission of molecules, mainly from CO. At higher densities, $\gtrsim 10^4\text{cm}^{-3}$, the coupling of gas and dust becomes important due to collisions and the temperature of both components may change, cooling or heating the gas depending on the temperature differences of the two components. Still, the temperature estimated inside cores are around 10-15K (see

Section 3.2 from Bergin and Tafalla (2007) and references therein).

There are several processes that could lead to the formation of Giant Molecular Clouds (GMCs) and there is a long way to go before reaching the scales where stars are born. For a deeper discussion of some of these mechanisms and formation of GMCs we refer to Bergin and Tafalla (2007); McKee and Ostriker (2007); Hennebelle and Inutsuka (2019) and references therein, below a summarized discussion will be made.

At first, there are two main roads to form a GMC. In a bottom-up approach, it is considered that the cloud results from several inelastic collisions of cold HI clouds¹. However, even in the best of scenarios, if only the collision of clouds is taken into account, it would take too long to form a GMC and clouds would most likely be destroyed by supernova explosions, since the life cycle of more massive stars would occur much faster than this process (the lifetime for a $10M_{\odot}$ star is about $30Myr$). On the other hand, the top-down approach considers large scale instabilities, such as Parker², magneto-Jeans instabilities³ or the passage of a spiral arm, which could then create clouds in a time-scale closer to what is expected, but this also needs careful consideration since we also need to explain the presence of turbulence in the clouds (see section 3.2.1 from McKee and Ostriker (2007) for further discussion).

For several decades now, it has been inferred that molecular clouds are turbulent environments. The formation of cold dense HI gas clouds in the interstellar medium (ISM) should be a phase transition from the WNM (Warm Neutral Medium) that increases the density abruptly. The result of this phase transition results in long lasting turbulent motions, which appear to be supersonic with regard to the the CNM (Cold Neutral Medium), but subsonic with regard to the WNM (see Chapter 3 of Hennebelle and Inutsuka (2019) and references therein). As an example, this turbulence appears subsonic with regard to WNM, but supersonic with regard to the CNM. Ossenkopf and Mac Low (2002) compared

¹ These are cold clouds, with densities $1 - 100cm^{-3}$ and temperature $100K$. They are mostly composed by neutral hydrogen and are detected through the 21cm line emission.

² Given that the interstellar gas in the Galactic disk is supported against gravity mainly by a large scale horizontal magnetic field and cosmic-ray pressure, this environment can become unstable to vertical motions of the plasma, leading to magnetic “loops” rising from the initial configuration and creating “valleys” where the material accumulates in the disk. We refer to Parker (1966); Mouschovias (1974) for further details.

³ Magneto-Jeans instability refers to the Jeans instability in the presence of magnetic, which also introduces a new magnetic pressure and tension components that can prevent the collapse.

velocity structures from the MC Polaris with a set of hydrodynamic and MHD simulations and found that these structures should be consistent with super-sonic turbulence driven at scales of about, or larger than the size of the cloud. However, the lifetime of a molecular cloud (MC) can be of several Myr, while turbulence is expected to decay in ~ 1 flow crossing time (L/σ_v , where L is characteristic length of the system and σ_v is the velocity dispersion; Mestel and Spitzer (1956)). Simulations of MCs that do not include energy injection, generally evolve into a free-fall collapse of the material, which is not observed. The characteristic free fall time of a homogeneous cloud can be calculated as:

$$t_{ff} = \sqrt{\frac{3\pi}{32G\rho}} \quad (1.1)$$

where G is the gravitational constant and ρ is the density of the cloud (for a cloud with $\rho \sim 500\text{cm}^{-3}$, $t_{ff} \sim 3.5\text{Myr}$, which is compatible with 1 flow crossing time. See Table 1 from Bergin and Tafalla (2007)). With that in mind, either clouds are young objects and turbulence is still decaying, or there is one or more sources of energy that replenish turbulent motions continuously, or turbulence is actually decaying slower than expected.

When it comes to a continuous injection of energy, some possibilities arise. Inside the clouds, protostars can be important, even though they are unlikely to be able to explain the ubiquity of turbulence. The turbulence cascade generally provides a flattening in the spectrum on scales above the injection one, which means that the turbulence provided by the early stages of star-formation might be important in the scales of clumps and cores, but would not be able to affect the scales of the parenting cloud. At the same time, several other events may occur in the vicinity of molecular clouds, which can drive turbulence. In the diffuse ISM, supernova explosions are the dominant source of energy injection, whilst inside spiral arms instabilities also make a significant contribution. But, considering that clouds are characterized by the fact that they are denser than the medium around them, energy coming from the outside is more likely to be reflected rather than to be transmitted to inside of the cloud. This does not mean that these sources do not have an influence over MCs.

Melioli et al. (2006) and Leão et al. (2009), for instance, analyzed the interaction of supernova remnants (SNRs) with molecular clouds and derived the conditions under which the clouds should be destroyed or induced to collapse. They conclude that this mechanism is not sufficient to drive alone star formation in our galaxy, even though it is

very potent and able to drive fragmentation. Another possibility of energy injection are the HII regions, which are able to drive turbulence at the scales of the GMC (see McKee and Ostriker (2007)) but also quench the star formation process. Spiral arms have also been considered to drive turbulence, e.g. Falceta-Gonçalves et al. (2015) performed 3D hydrodynamic simulations and found the spiral arms are able to drive turbulence in the scales of MCs ($\sim 100pc$), converting about 10 to 25 per of the potential energy of gas into turbulence per arm crossing. This seems to be of higher efficiency compared to other models of turbulence driving and is also in agreement with observations of nearby galaxies.

Even though the origin of turbulence is not completely clear, its consequences are easier to see. MCs are known to show filamentary structures, inside which about 70-80% of stars are formed. Past works have shown that filaments can be formed even on pure hydrodynamic simulations of MCs, but the consideration of the presence of magnetic fields and self-gravity could enhance the formation of elongated structures (Hennebelle and Inutsuka (2019) and references therein).

Several authors (e.g. Melioli et al. (2006); Hall et al. (2006); Mac Low et al. (2004); Santos-Lima et al. (2010); Leão et al. (2013); Hennebelle (2013)) performed hydrodynamical and MHD simulations of the ISM and analysed the aspect of the structures formed. Among their findings, they verified that the presence of magnetic fields helps to create more filamentary clumps and allows for structures to survive for longer. As we are going to see in the next section, the nature of MHD turbulence naturally leads to anisotropy, specially at smaller scales.

Previous studies have also concluded that, at least in the absence of self-gravity, magnetic fields and the velocity of the flow are preferentially aligned with each other in dense regions (Banerjee et al. (2009); Iffrig and Hennebelle (2017)) and more recently, observations and numerical studies are indicating that the gradient of density is also correlated to the magnetic field (Soler et al. (2013); Planck Collaboration et al. (2016); Soler and Hennebelle (2017)).

The better understanding of the interlinks between magnetic fields, turbulence and the formation and evolution of these IS structures can give clues on how the clumps are formed and may help us to understand, for instance, why the star formation rate (SFR) in our galaxy is low ($\sim 3 - 5M_{\odot}yr^{-1}$; Shu et al. (1987)). Federrath and Klessen (2012) studied different theories to estimate the star formation rate and compared with simulations and

observation. They found their best fit for the estimations using a modified version of Krumholz and McKee (2005) and Padoan and Nordlund (2011) theories and concluded that the SFR is primarily dependent on interstellar turbulence, but magnetic field effects can also be important.

In this work, we intend to further contribute to these studies and explore, by means of 3D MHD simulations, the evolution of turbulent MCs including the effects of self-gravity, in different regimes of turbulence. Given this, in the subsequent sections we are going to discuss the main aspects of hydrodynamical and MHD turbulence, and how these are related to the gravity, star forming regions, and past works like those mentioned above (Krumholz and McKee (2005); Padoan and Nordlund (2011)).

1.2 MHD turbulence in Molecular Clouds

Turbulence is a process present through several orders of magnitude in the ISM, e.g. see the 3D estimated spectrum of the ISM from Chepurnov and Lazarian (2010); Lazarian (2011). In this section it will be discussed the main characteristics of the hydrodynamic and magnetohydrodynamic (MHD) turbulence.

1.2.1 Hydrodynamic Turbulence

A fully mathematical theory of turbulence does not exist, but through the decades, some important qualitative results became known. A fully developed turbulence in a fluid happens when there is an extremely irregular and disordered variation in the velocity in time and space. This velocity continually fluctuates around a mean value. If this fluid, however, has an ordered velocity field, the flow is laminar (Landau and Lifshitz (1959)).

Before discussing the properties of the MHD turbulence, we will begin with the hydrodynamical case. The flow's velocity must obey the following equation for an incompressible fluid ($\nabla \cdot \mathbf{v} = 0$):

$$\frac{\partial \mathbf{v}}{\partial t} + (\mathbf{v} \cdot \nabla) \mathbf{v} = -\frac{\nabla p}{\rho} + \nu \nabla^2 \mathbf{v} \quad (1.2)$$

The second term on the right hand side of the equation is related to viscosity, which helps to diminish the randomness in the velocity. If viscosity dominates the equation, the flow becomes laminar. On the left hand side of the equation, however, the advection term

highlights the non-linearity of the equation. When this term is more important, turbulence can develop. If we compare these two terms, an important quantity can be calculated, the Reynold's number:

$$Re = \frac{lv}{\nu} \quad (1.3)$$

where l is a characteristic length at which gradients are calculated and v is a characteristic velocity of the flow. Turbulent flows may arise when $Re \gg 1$, but the exact value of Re that distinguishes a laminar flow can vary from one system to another.

Turbulence can be seen as the superposition of several eddies of different sizes. With that, Re can be defined for eddies of different sizes, $Re_\lambda = \lambda v_\lambda / \nu$. Larger eddies have bigger values of Re_λ , with λ of the order of the size of system. As we go to smaller and smaller eddies, this value becomes of the order of unity. This means that on these small scales, viscosity becomes important and the flow becomes laminar.

Therefore, there is a “cascading” of energy, coming all the way from the *injection* scale, with larger eddies, that will be dissipated at certain rate ϵ in the smaller scales, also referred as the *dissipative* scale. This rate of dissipation of energy will be of the order of (Landau and Lifshitz (1959)):

$$\epsilon \sim v_\lambda^3 / \lambda \quad (1.4)$$

where v_λ is the velocity associated to the scale λ in the flow. This relation (Kolmogorov and Obukhov's scaling law) can be interpreted as in the following, v_λ^2 gives the order of magnitude of the total kinetic energy per mass in eddies with all scales of the order of λ or less. The energy is dissipated at a rate ϵ , after cascading to the dissipative scales, in the turnover time λ/v_λ .

In the dissipative scale, Re_λ is of order unity, which gives the order of magnitude of the scale where viscosity becomes important. This value can be estimated as:

$$\lambda_\nu \sim v_\nu^3 / \epsilon \quad (1.5)$$

$$\lambda_\nu \sim \nu / v_\nu \quad (1.6)$$

$$v_\nu \sim \nu/\lambda \quad (1.7)$$

$$\lambda_\nu^4 \sim \nu^3/\varepsilon \quad (1.8)$$

The range of scales λ between the injection and dissipative scales, $\lambda_0 \leq \lambda \leq \lambda_\nu$, is usually referred as the *inertial range*. Kolmogorov and Obukhov's law can be expressed in an equivalent spatial spectrum form. Replacing the scales by the corresponding wave number $k \sim 1/\lambda$, we can write:

$$E(k) \propto \varepsilon^{2/3} k^{-5/3} \quad (1.9)$$

where $E(k)dk$ represents the kinetic energy per unit mass of fluid in eddies with k values in the range dk . This is Kolmogorov spectrum for the incompressible hydrodynamic turbulence.

However, turbulence in the ISM can be also supersonic, as we have seen in Section 1.1. With the sonic Mach number being defined as:

$$\mathcal{M}_s = \frac{v}{c_s} \quad (1.10)$$

where c_s is the sound speed of the environment. When $\mathcal{M}_s > 1.0$ fluid motions travel faster than the sound speed of the media, which leads to shocks. The presence of compressible modes alter the spectrum since the energy transfer can occur directly between large and small scales instead of decaying through the interaction of the eddies. A better description of this scenario is given by the Burgers turbulence (Burgers (1974); Menon and Pego (2007)) with the energy spectrum following:

$$E(k) \propto k^{-2} \quad (1.11)$$

Another ingredient we are going to take into account is the presence of magnetic fields that can also alter the cascade of energy. The different MHD turbulence regimes will be discussed in the next section.

1.2.2 MHD turbulence

There are excellent reviews on MHD turbulence in Elmegreen and Scalo (2004); Scalo and Elmegreen (2004); Lazarian et al. (2012); Falceta-Gonçalves et al. (2014). Here, we

will present just a brief description.

In the case of a MHD environment the cascading of energy is influenced by the strength of the magnetic field (\mathbf{B}). The importance of \mathbf{B} will be characterized by the Alfvén velocity:

$$v_A = \frac{\mathbf{B}}{\sqrt{4\pi\rho}} \quad (1.12)$$

When the non-linear interaction of the perturbations is strong enough, Alfvénic turbulence can also be described by vortices (Lazarian et al. (2012)). The presence of a strong field however, can elongate the vortex and the cascade of energy becomes different in the directions parallel and perpendicular to the field.

Following Goldreich and Sridhar (1995), the strength of the perturbations can be characterized by a non-linearity parameter:

$$\zeta_{\lambda_{\perp}} \sim \frac{k_{\perp} v_{\lambda}}{k_{\parallel} v_A} \quad (1.13)$$

where $k_{\parallel}^{-1} \sim \lambda_{\parallel}$ and $k_{\perp}^{-1} \sim \lambda_{\perp}$, with λ_{\parallel} and λ_{\perp} being the size of the perturbation (the eddy) in the parallel and perpendicular directions to the magnetic field, respectively. In the case of critical balance, $\zeta_{\lambda_{\perp}} \sim 1$, which means that the period of an Alfvén wave ($\sim \lambda_{\parallel}/v_A$) is similar to the turnover time of the eddy ($\lambda_{\perp}/v_{\lambda}$).

The cascade of energy can now proceed until a scale λ_{η} is reached. This is the resistive dissipation scale and is associated to the magnetic Reynolds number $Rm_{\lambda} = \lambda v_{\lambda}/\eta$, where η is the magnetic resistivity (e.g. de Gouveia Dal Pino (1995)). The dissipative scale is now defined by whatever is greater, either λ_{ν} or λ_{η} .

The cascading of energy occurs mostly in the perpendicular direction, with the inertial range in this direction being similar to Kolmogorov's spectrum (eq. 1.4). With the assumption of critical balance, this yields:

$$\lambda_{\parallel} \sim \frac{v_A}{\epsilon^{1/3}} \lambda_{\perp}^{2/3} \quad (1.14)$$

which indicates that the eddies become more and more elongated as we progress through the cascade.

At this point we are going to define the Alfvénic Mach number as:

$$\mathcal{M}_A = \frac{v}{v_A} \quad (1.15)$$

Goldreich and Sridhar (1995) considers $\mathcal{M}_A \sim 1.0$ and so the turbulence injection is trans-Alfvénic.

If $\mathcal{M}_A > 1.0$ at the injection scale L , magnetic fields are not dynamically important and the system behaves similarly to the hydrodynamical case as discussed in the previous section. However, as the cascade proceeds to smaller scales, the magnetic field eventually becomes important at a scale λ_A , that can be estimated as (Lazarian et al. (2012)):

$$\lambda_A \sim L(v_A/v_L)^3 = L\mathcal{M}_A^{-3} \quad (1.16)$$

In the case of weak MHD turbulence, $\mathcal{M}_A < 1.0$ at the injection scale, the cascade occurs through the interaction of wave packets traveling parallel to the magnetic field, and higher number of interactions is needed for the cascading to occur. In this scenario, turbulence can become strong at a scale:

$$\lambda_{strong} \sim L(v_L/v_A)^2 = L\mathcal{M}_A^2 \quad (1.17)$$

For isotropic weak turbulence, the scaling follows the Iroshnikov and Kraichnan spectrum, in this case, $E(k) \propto k^{-3/2}$.

In the case of the ISM, Goldreich and Sridhar (1997) proposed that weak turbulence is irrelevant. For the strong cascade, $E_{\perp}(k) \propto k_{\perp}^{-5/3}$, while the anisotropy of the eddies follows the relation $k_{\parallel} \propto k_{\perp}^{2/3}$ (1.14).

1.3 The aim of this work

As stressed before, the aim of this work is to try to improve our understanding of how IS clouds and star forming regions are produced and how this is influenced by turbulence, magnetic fields, and self-gravity. For this purpose, we have performed 3D MHD simulations of these systems considering models with and without self-gravity, forced supersonic turbulence, with $\mathcal{M}_s \sim 2.0, 4.0$ and 7.0 (eq. 1.10). We also consider two different initial

conditions with regard to the strength magnetic field, i.e. models with sub-Alfvénic (initial $\mathcal{M}_a \sim 0.7$) and super-Alfvénic (initial $\mathcal{M}_a \sim 2.0$) Mach numbers (eq. 1.15).

The chapters of this dissertation are organized as follows: in Chapter 2, we describe the numerical methodology we employ in this dissertation, including a description of the MHD code, as well as the statistical methods we employ in the analysis of the simulated models; in Chapter 3, we describe the results of our numerical simulations. In Chapter 4, we present a brief comparison of our results with observations; and finally in Chapter 5, we compare our results with former numerical studies, draw our conclusions, and present the prospects for continuing this work.

Methodology

In order to study the evolution of molecular cloud environments and the initial stages of star formation, and explore how these are affected by turbulence, magnetic fields and self-gravity, we consider three-dimensional MHD simulations of two families of models. First, considering only the presence of MHD turbulence, with no self-gravity, we take the numerical simulations of isothermal molecular clouds performed by Cho and Lazarian (2003) and Burkhart et al. (2009). In a second part, we consider isothermal models with self-gravity, based on MHD simulations performed by ourselves using a modified version of the code developed by Kowal et al. (2007)(see also Leão et al. (2009); Santos-Lima et al. (2010)). Both sets of simulations have the same initial conditions, as it will be described below.

The second set of simulations were only possible thanks to professor Blakesley Burkhart and the Center for Computational Astrophysics in New York, that allowed us to use their infrastructure to perform the simulations.

To study how the initial stages of star formation behaviour, the ideal MHD equations will be numerically solved in their conservative form:

$$\frac{\partial \rho}{\partial t} + \nabla \cdot (\rho \mathbf{v}) = 0 \quad (2.1)$$

$$\frac{\partial}{\partial t}(\rho \mathbf{v}) + \nabla \cdot [\rho \mathbf{v} \mathbf{v} + (P + \frac{B^2}{8\pi})\mathbf{I} - \frac{\mathbf{B}\mathbf{B}}{4\pi}] = \rho \mathbf{g} + \mathbf{F} \quad (2.2)$$

$$\frac{\partial \mathbf{B}}{\partial t} + \nabla \cdot (\mathbf{v}\mathbf{B} - \mathbf{B}\mathbf{v}) = 0, \quad \nabla \cdot \mathbf{B} = 0 \quad (2.3)$$

where ρ , \mathbf{v} and \mathbf{B} are density, velocity and magnetic field, respectively, P is the thermal pressure of the gas, \mathbf{g} is gravity, E is the total energy, \mathbf{I} is the identity dyadic tensor and \mathbf{F} is the source term for the turbulence driving. Tests performed by our group considering the

radiative cooling of an optically thin gas, revealed that the turbulent system quickly evolves to an isothermal state reaching the minimum temperature allowed in the simulation. For this reason, we are considering a cold cloud with a temperature of 10K, which is of the order of the estimated temperature from cold dust emission inside cold dark clouds (see Chapter 1).

With this isothermal assumption, we do not have to integrate the energy conservation above in our simulations. An ideal isothermal equation of state will be considered to close our system of equations, so that the pressure can be written as $P = \rho c_s^2$, where $c_s = \sqrt{k_b T / \bar{m}}$ is the isothermal sound speed of the gas, where \bar{m} is the average mass of the gas, and in this work it will be given by $\bar{m} = \mu m_H$, with $\mu = 2.3$.

In eq. 2.2, $\rho \mathbf{g} = -\rho \nabla \Psi$ is the gravitational force of the gas due to self-gravity, which is considered in the second family of models of our study, and obeys the Poisson equation:

$$\nabla^2 \Psi = 4\pi G \rho \quad (2.4)$$

Finally, the source term \mathbf{F} is responsible for the turbulence injection. Turbulence is driven solenoidally. The forcing is introduced in the Fourier space around a characteristic wavelength that defines the injection scale ($l_{inj} = 1/4L$, where L is the size of the domain). The turbulence is then allowed to cascade down to the (numerical) dissipation scale while being continuously injected in the system. This process continues for around one dynamical time, L/c_s . Once the turbulence has cascaded down, only then self-gravity is turned on, in the models where it is considered. No condition to stop the simulation was imposed and no feedback from star formation was considered, which means that later snapshots, after gravity takes hold of the system, can be discarded (this will be further discussed in Section 3.1).

The first set of models, which neglects self-gravity, has $\psi = 0$ in the equations above. These simulations were built using a second order accurate hybrid essentially non-oscillatory (ENO) scheme to solve the MHD equations (Cho and Lazarian (2003); Burkhart et al. (2009)), while the set of models with self-gravity employed a total variation diminishing (TVD) method (Kowal et al. (2009); Leão et al. (2009); Santos-Lima et al. (2010)). Both codes are based on the Godunov method (Appendix A.1) and use a Runge-Kutta procedure (e.g. Londrillo and Del Zanna (2000); Del Zanna, L. et al. (2003)) for time

integration. To solve the Poisson equation, a multigrid method was used (see more details about the numerical method in Appendix A.2).

2.1 Turbulence vs Gravity - Triggering star formation

To start, let us remember that the simplest (and ultimate) condition for a cloud or clump to collapse under the action of gravity is given by the Jeans criterion (Jeans and Darwin (1902)):

$$R_J = \left(\frac{3}{4\pi G} \right)^{1/2} \frac{c_s}{\rho^{-1/2}} \quad (2.5)$$

And in the presence of a strong magnetic support against gravity, this changes to:

$$R_J = \left(\frac{3}{4\pi G} \right)^{1/2} \rho^{-1/2} \left(c_s^2 + \frac{v_A}{2} \right)^2 \quad (2.6)$$

But, as discussed before, GMCs are very turbulent regions. Supersonic turbulence in these systems can create over-dense regions that may achieve the condition for collapse at the same time that it may destroy these structures. The density in turbulent regions can generally be well represented by a lognormal distribution. If we define $s \equiv \ln(\rho/\rho_0)$, the density distribution should follow (e.g. Burkhart (2018)):

$$p(s) = \frac{1}{\sqrt{2\pi\sigma_s^2}} \exp\left(-\frac{(s-s_0)^2}{2\sigma_s^2} \right) \quad (2.7)$$

where σ_s is the standard deviation of the lognormal, s_0 gives the value of s for the mean density. The characteristics of the turbulence are related to these values according to the following relations:

$$s_0 = -\frac{1}{2}\sigma_s^2 \quad (2.8)$$

$$\sigma_s^2 = \ln[1 + b^2 M_s^2] \quad (2.9)$$

where b is a dimensionless turbulent forcing parameter (Federrath et al. (2008)) related to the solenoidal¹ and compressive modes of the turbulence. For purely solenoidal turbulence

¹ For solenoidal turbulence driving, $\nabla \cdot v = 0$. For compressive turbulence driving, $\nabla \times v = 0$ (Federrath et al. (2008)).

driving, we have $b = 1/3$ while for purely compressive driving, $b = 1.0$. \mathcal{M}_s is the sonic Mach number (eq. 1.10).

The presence of self-gravity, however, introduces a second trend at higher densities. The collapse of dense structures leads to a power-law like distribution. For $s > s_t$, where s_t is transitional value between the lognormal distribution and the power-law tail, we can consider (e.g. Burkhardt (2018)):

$$p_{PL}(s) \propto \exp(-\alpha s) \quad \text{for } s > s_t \quad (2.10)$$

$$s_t = \frac{1}{2}(2|\alpha| - 1)\sigma_s^2 \quad (2.11)$$

where α is the power-law index.

The collapse of structures is not immediate and therefore, the power-law changes along time as collapsed material accumulates at the smaller scales of the cloud. However, as previously discussed, many filaments inside MCs are not bound by gravity and the characteristics of the turbulence that is being driven in the cloud can change the evolution and efficiency in which stars are formed (Federrath and Klessen (2012)).

It is important to highlight that the lognormal probability density function (PDF, eq. 2.7) is also important for a number of analytic models of star formation. The action of turbulence inside MCs is surely an important factor in setting the core mass function (CMF) and the stellar initial mass function (IMF). A similarity between the two may be an indication that the same process that fragments gas at smaller scales is responsible for setting the formation of stars. However, different observational tracers have been used for different scales, and the power-law distribution for the CMF, $dN/dM \sim M^{-\alpha}$, has different indices for different frequency bands (being $\sim 1.4 - 1.8$ for CO observations, which traces larger structures, and $\sim 2.0 - 2.5$ for millimeter/sub-millimeter dust continuum, which traces regions around dense cores). From this, it is hard to conclude what are the different levels of structure in a cloud (see Bergin and Tafalla (2007) and references therein for further discussion).

At this point, we know that turbulent gas generally follows a lognormal distribution, that MHD turbulence may introduce anisotropy, specially at small scales, and that magnetic fields can most likely help in setting the initial distribution of filaments. Also, we know that once collapse starts a power-law like distribution for higher densities is seen.

This brings the question, how much of the gas can actually contribute to form stars? How much of the distribution is actually gravitationally bound?

To evaluate this, past studies have assumed that above a certain critical value of density, all material would contribute to form stars. This critical value however, can depend on several parameters, such as the mean density of the clouds, the sonic Mach number, the strength of the magnetic field, and so on. Since we want to study in this work the influence of gravity over the filamentary structure inside molecular clouds, the discussion below will be important to set the initial conditions of our models and to help differentiate the regions where turbulence dominates and where gravity dominates.

We will consider that above a density ρ_c all matter contributes to star formation. The critical density depends on the assumptions taken hence, we shall discuss some of the proposed models in the literature.

We will begin with Krumholz and McKee (2005). To evaluate the relative importance of turbulence compared to gravity, we will define the virial parameter, α_{vir} , following Bertoldi and McKee (1992):

$$\alpha_{vir} \sim \frac{2E_k}{E_g} = \frac{5v_0^2 c_s^2 R}{GM} \quad (2.12)$$

where E_k and E_g are the kinetic and gravitational energies of the system, respectively, v_0 is the one-dimensional rms velocity and M is the mass evaluated over a sphere of radius R .

Krumholz and McKee (2005) calculated the critical density for star formation based on the idea of pressure support. In their model, the critical density is calculated comparing the sonic scale (λ_s), which is the scale where the turbulent velocity differences are of the order of the speed of sound, with the Jeans' length (eq. 2.5). They define the critical density for collapse as being the same as a critical Bonnor-Ebert sphere of size λ_s . For this model:

$$\frac{\rho_c}{\rho_0} = \frac{\pi^2 \phi_x^2}{15} \alpha_{vir} \mathcal{M}_s^{2/m-2} \quad (2.13)$$

where ϕ_x was calibrated from smoothed-particle-hydrodynamical (SPH) simulations and is of order unity, and m comes from the velocity-size relation, $v \propto l^m$. Krumholz and

McKee (2005) assume $m = 0.5$, however, as Padoan and Nordlund (2011) briefly discuss, this value may be different for supersonic turbulence.

The next model to be discussed considers that turbulence triggers collapse through its dynamical pressure. Also, Padoan and Nordlund (2011) takes into account the contribution of the magnetic field for the determination of the critical density for star formation. The critical density in this case is defined as:

$$\frac{\rho_c}{\rho_0} = 0.067 \zeta^{-2} \alpha_{vir} \mathcal{M}_s^2 \frac{(1 + 0.925 \beta^{-3/2})^{2/3}}{(1 + \beta^{-1})^{2/3}} \quad (2.14)$$

where $\zeta \leq 1$ and ζL_0 is the turbulence integral scale (L_0 being the size of the system), and β is the ratio between thermal pressure and magnetic pressure. Note that in the limit $\beta \rightarrow \infty$, i.e. the hydrodynamical case, the dependence of ρ_c with the Mach number is the same as in equation 2.13 for $m = 0.5$. The numerical difference comes from the physical derivation of ρ_c .

2.2 *Quantifying the relative orientation between structures and the magnetic field*

One of the aims of this work is to quantify the relative orientation between the IS structures and the embedded magnetic fields, since this is something that we may compare directly with observations and, in doing so, we may infer about general properties of the observed structures.

In this section we describe how to quantify the angular distribution between density gradient and magnetic field vectors within the simulated molecular clouds.

This method is described in detail in Soler et al. (2013). The idea is to build histograms of relative orientation between the quantities above (HRO). Given a density structure, gradients of density will be obviously perpendicular to the iso-density contours. In this sense, density structures, like filaments, will be aligned in the direction normal to these gradients. Comparing the density gradient with the magnetic field orientation, it is possible to evaluate how the filamentary structures are aligned with the background magnetic fields and thus to extract information about the formation of these structures (see below). One can obtain this relative orientation through:

$$\phi = \arctan\left(\frac{\mathbf{B} \times \nabla\rho}{\mathbf{B} \cdot \nabla\rho}\right) \quad (2.15)$$

With ϕ as defined above, we can evaluate the histogram of $\cos\phi$ within different density bins (or intervals). A peak in this histogram around $\cos\phi = 0$ means that most of the field is perpendicular to the density gradient, in other words, the field is aligned to the structures. Similarly, $\cos\phi = \pm 1$ means the density gradient is parallel to the field, hence the field is perpendicular to the structures. A possible interpretation for a field line predominantly perpendicular to the density gradient (i.e., aligned to the filaments), in turn, may be an indication of compression of the field lines along the structure by thermal pressure gradients (which are aligned with density, gradients in general, and specially in the present work, where temperature is constant and therefore, $\nabla p \propto \nabla\rho$). On the other hand, a field line predominantly parallel to the density gradient (or perpendicular to the filament), may be an indication of the prevalence of magnetic forces (which are always normal to \mathbf{B}) and/or gravitational forces (if present) which cause the collapse of plasma predominantly along the lines, since in the normal direction to the lines, magnetic pressure gradients and tension difficult the plasma motion.

This method can also be applied to the column density ($\int \rho dl$, where dl is an element along the line of sight, LOS) gradients, much in the same way, the only difference is the fact that the histogram is generally evaluated for $\phi + 90^\circ$. In three dimensions, two random vectors have a higher probability of being perpendicular to each other rather than being parallel, that is why we choose to use $\cos\phi$ in 3D. This is not the case in two dimensions and we can use simply the information from ϕ . This is also what is used in observations.

The angles are calculated between the gradient of column density vector and the estimated B_\perp , the later one being the projected magnetic field in the plane of the sky, which is obtained from the Stokes parameters, i.e., a set of values that characterize the polarization of electromagnetic waves (see below).

In order to compute these parameters for polarized radiation from the simulations, we will use the same assumptions as Falceta-Gonçalves et al. (2008). In other words, we assume that only thermal emission is emitted by grains that are perfectly aligned with the magnetic field. The dust abundance (which is not explicitly considered in our simulations) is considered to be proportional to the gas density, as well as the intensity of its emission. Finally, we consider that all grains emit at a single temperature, as in our domain. With

these assumptions, for each cell of the computational domain we calculate:

$$\begin{aligned} q_{ijk} &= \rho_{ijk} \cos 2\psi_{ijk} \sin^2 i_{ijk} \\ u_{ijk} &= \rho_{ijk} \sin 2\psi_{ijk} \sin^2 i_{ijk} \end{aligned} \quad (2.16)$$

where the sub-indices i, j and k refer to the cartesian coordinates x, y and z , ρ is the local density, ψ is the local angle of alignment, determined by the projection of the local magnetic field into the plane of the sky, and i is the angle between the magnetic field and the line of sight (LOS). Integrating q , u and ρ along a chosen line of sight results on the Stokes parameters Q , U :

$$\begin{aligned} Q &= \sum_0^k q_{ijk} \delta x \\ U &= \sum_0^k u_{ijk} \delta x \end{aligned} \quad (2.17)$$

and the column density:

$$N_H = \sum_0^k \rho_{ijk} \delta x \quad (2.18)$$

where δx is the size of the cell, given the resolution of the simulation. This way, the intensity of E and its direction will be calculated as:

$$\begin{aligned} E &= \sqrt{Q^2 + U^2} \\ \Phi_B &= 1/2 \arctan(U/Q) \end{aligned} \quad (2.19)$$

Now, we can use equation 2.15, where $\nabla\rho$ can also be replaced by ∇N_H and \mathbf{B} by \mathbf{B}_{pos} if we use column density and polarization maps, respectively, to build a histogram to evaluate the angular distribution.

To analyze the behaviour of filaments inside molecular clouds means that we need to evaluate a wide range of density values that spans across 2 to 3 orders of magnitude. To check how the alignment between density structures and the magnetic field occurs at different scales, we are going to split the system into several bins. To guarantee a comparable statistics for each density bin, the density range will be divided into bins with the same numbers of cells and then the HRO will be calculated for each bin. The information of the angles can then be applied into a more sophisticated method of analysis.

2.2.1 Projected Rayleigh statistics (PRS)

To study the column density behaviour, a more sophisticated method can be used, namely, the projected Rayleigh Statistics, which later on will also be employed to compare the results of the numerical simulations with observations of several molecular clouds. Below, it follows a summarized description of this method from Jow et al. (2018).

The PRS is based on the Rayleigh test (e.g. Mardia and Jupp (1999)), which can be used to check if a set of angles is uniform. Given a set θ_i of n angles, with $\theta_i \in [0, 2\pi]$, the Rayleigh test is calculated as

$$Z = \frac{(\sum_i^n \cos \theta_i)^2 + (\sum_i^n \sin \theta_i)^2}{n} \quad (2.20)$$

However, our distribution is not uniform and the angle distribution is initially between $[-\pi/2, \pi/2]$. To apply the Rayleigh test, first the angles need to be multiplied by two, mapping our axial angle distribution to a circular distribution. Since the purpose of using this tool is to analyze if there is a preferential alignment that is parallel ($\theta = 0$) or perpendicular ($\theta = \pi$), it is possible to see how the data compare to a specified mean direction. In this case, taking the mean direction as $\theta = 0$, we calculate the Projected Rayleigh Statistics as

$$Z_x = \frac{\sum_i^n \cos \theta_i}{\sqrt{n/2}} \quad (2.21)$$

where positive values of Z_x are indicative of strong parallel alignment between two vectors while negative values indicate a strong perpendicular alignment between two vectors.

Jow et al. (2018) argue that, in the limit of $n \rightarrow \infty$, the PRS approximates the standard normal distribution. Therefore, for a general distribution of angles the variance of Z_x can be estimated as

$$\sigma_{Z_x}^2 = \frac{2 \sum_i^n (\cos \theta_i)^2 - (Z_x)^2}{n} \quad (2.22)$$

The error of each measurement of Z_X will be given by the equation above. Later on, this tool will be also used to compare our simulations to observational data taken from molecular clouds with Herschel telescope and Planck satellite.

We are going to make a differentiation between the PRS applied to the density distribution of our 3D simulated cube and the PRS applied to the integrated simulated column

density maps along a given line of sight. When analyzing a 3D distribution, we will calculate the PRS values for the angles between the gradient of density ($\nabla\rho$) and the magnetic field (\mathbf{B}). In this case, eq. 2.21 will be referred as Z_B . For the integrated density maps along a given line of sight (column density) however, what is being evaluated is the angle between the polarization pseudo-vector (\mathbf{E}) (instead of the projected plane of the sky magnetic field, \mathbf{B}_\perp) and the gradient of column density (∇N_H)(see Figure 2.1), in this case eq. 2.21 will be referred as Z_E .

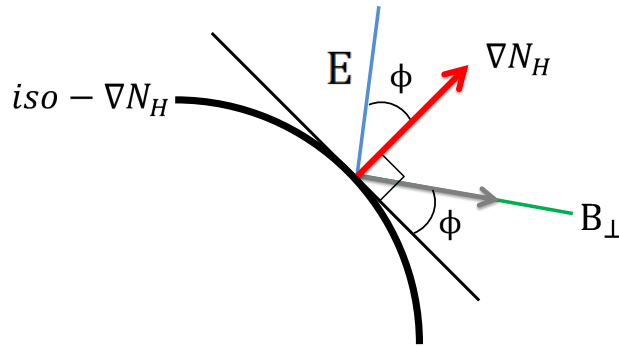


Figure 2.1: Scheme of the vectors that are considered to calculate the angle ϕ between the density gradient of N_H and the polarization pseudo-vector (\mathbf{E}) for column density maps. (Adapted from Planck Collaboration et al. (2016))

It is important to make clear what positive and negative values of Z_E and Z_B mean. For the integrated column density maps, Z_E estimates the average angle between the gradient of column density, ∇N_H , and the direction of the polarization pseudo-vector, \mathbf{E} . Given an iso-contour of column density, since ∇N_H is perpendicular to it and \mathbf{E} is perpendicular to the projected magnetic field in the plane of the sky, \mathbf{B}_\perp , the same angle ϕ will be also between \mathbf{B}_\perp and the direction of the density structure (iso-contour). Fig. 2.1 was adapted from Planck Collaboration et al. (2016) and shows what is described above. With this, Z_E measures if \mathbf{E} is parallel ($Z_E > 0$) or perpendicular ($Z_E < 0$) to the gradient of column density, ∇N_H .

When it comes to Z_B , we are comparing directly the magnetic field direction (\mathbf{B}) with

the density gradient ($\nabla\rho$), so positive values of Z_B indicate parallel alignment between the two vectors while negative values indicate that the two vectors are perpendicular.

2.3 Boundary and initial conditions

To simulate the clouds, we consider a cubic Cartesian domain with periodic boundaries, which perfectly mimic a slice of these systems in the ISM. Both codes run in code units. For the first family of models, the unity of length is the size of the injection scale (L_{inj}). The rms velocity (δV) is kept close to unit so that the velocity can be seen as in units of δV , and $\mathbf{B}/(4\pi\rho)^{1/2}$ is the Alfvén velocity in the same units. The unit of time is the turnover time of the largest eddy, $L_{inj}/\delta V$. The injection of turbulence is made in a scale about 1/4 of the size of domain ($L_{inj} = L/4$). Also, for density unit we take the initial ambient density ρ_0 . The remaining quantity units are all derived from these ones.

In the second set, we take for unity of length the size of the domain (L), and for velocity unit we take the isothermal sound speed (c_s), which implies time unit L/c_s . The magnetic field is scaled such that $\mathbf{B}_{c.u.} = \mathbf{B}/(4\pi)^{1/2}$. Also, for density unit we take the initial ambient density ρ_0 . The remaining quantity units are all derived from these ones.

Initially, the simulation starts with a homogeneous distribution of density (ρ_0) and uniform magnetic field distribution along the z direction, with an isothermal equation of state inside a $10pc \times 10pc \times 10pc$ domain.

The simulations were performed using resolutions of 64^3 , 256^3 and 512^3 cells in the three directions of a uniform grid. Our lower resolution simulations were mainly used for testing and calibration of the initial conditions of the models that consider self-gravity. With that said, previous works have used similar resolutions of 256^3 to 512^3 for studying molecular clouds with good statistical convergence of the results already in 256^3 resolution, at least for non self-gravitating turbulent models (e.g. Kowal and Lazarian (2007); Burkhart et al. (2009); Santos-Lima et al. (2010)). Figure 2.2 shows a comparison of column density maps integrated along a line of sight (LOS) parallel to the initial magnetic field for two models with the same initial conditions (initial sonic Mach number $\mathcal{M}_s = 7$, and Alfvénic Mach number $\mathcal{M}_A = 0.6$), and 256^3 and 512^3 resolutions, for two different times (see Table 2.1 for initial conditions, and Chapter 3 for more details). Figure 2.3 shows the 3D power spectrum time evolution for the same models. On the left side it is presented the model

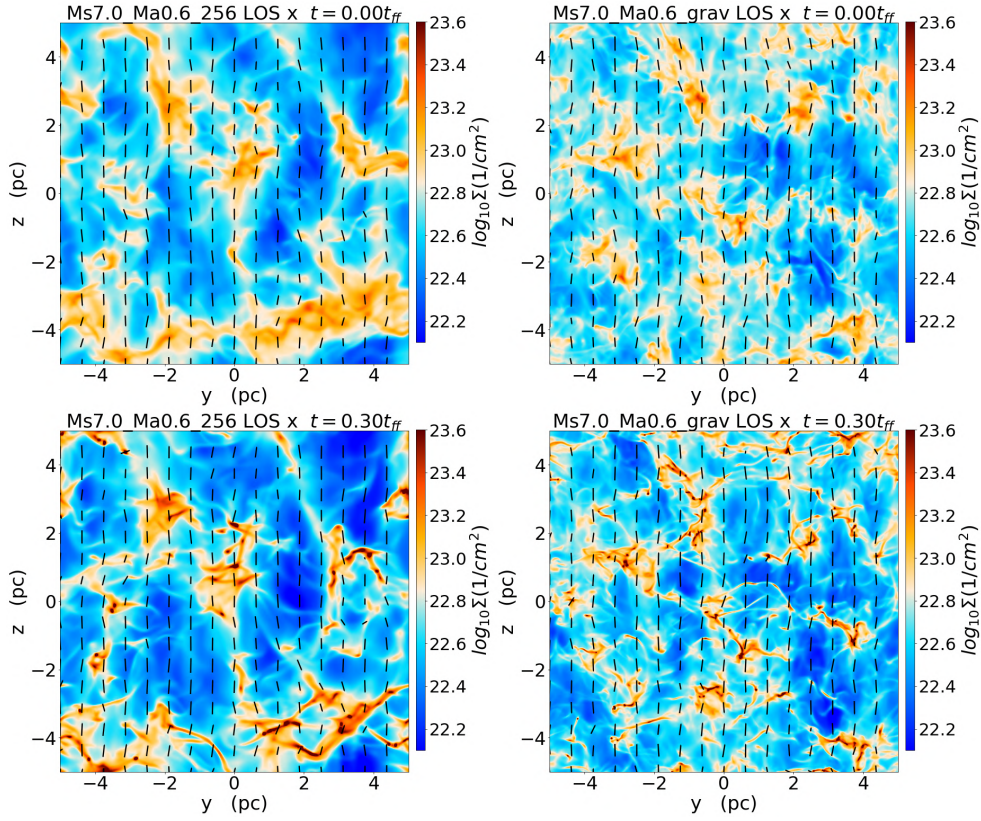


Figure 2.2: Comparison of column density distribution for two models with same initial conditions and different resolution. On the left side, 256^3 cells were used. On the right side 512^3 cells were used. Note that the higher resolution allows for a higher fragmentation of the structures, but the results are still similar. The dashed lines represent the direction of the projected magnetic field onto the plane of the sky (see more details on the text).

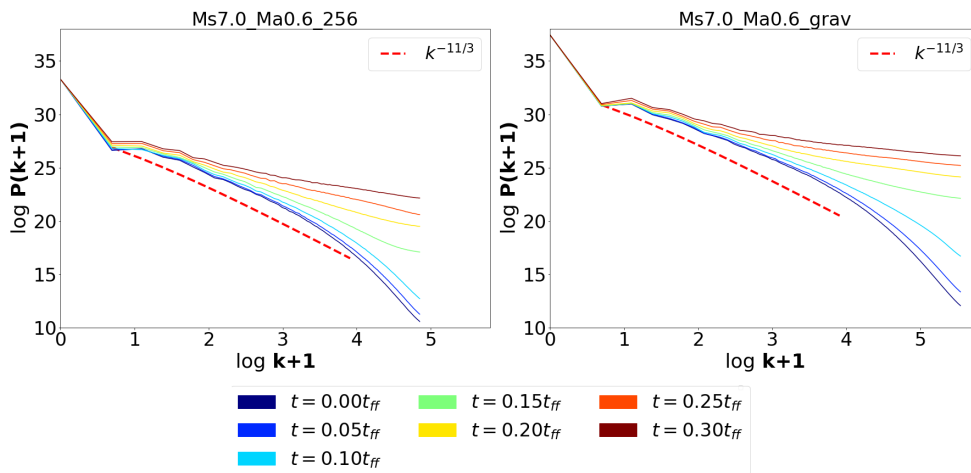


Figure 2.3: Comparison of the power spectrum for the same models of Figure 2.2. On the left side, 256^3 cells were used. On the right side, 512^3 cells were used. The red dashed line represents the Kolmogorov power-law ($k^{-11/3}$, in the 3D case) for reference.

with resolution 256^3 , and on the right side the model with resolution 512^3 . Note that the column density maps show similar behaviour. The power spectrum of both models is initially compatible with the Kolmogorov cascade, and show a flattening at later times. Obviously, the higher resolution model shows more details at smaller scales (bigger values of k , Figure 2.3), but the statistical behaviour is very similar for both resolutions, as long as turbulent motions are dominating. Since gravitational forces affect primarily smaller scales, in order to study its effects, we will consider here the higher resolution models when self-gravity is present.

Also, since part of the objective of this work is to study the influence of self-gravity on the formation of the clouds and their collapsing sub-structures, the initial setup is built to ensure the minimum condition for collapse, such that $\alpha_{vir} \sim 0.5$ (eq. 2.12).

Our simulations are characterized by three parameters, the sonic Mach number \mathcal{M}_s , the Alfvénic Mach number \mathcal{M}_A and the ambient density ρ_0 , which depends on α_{vir} (eq. 2.12). These parameters are described in table (2.1). The table also gives corresponding thermal to magnetic pressure (β_0) for each model, the initial free-fall time (eq. 1.1) calculated for the initial ρ_0 , for the simulations that consider self-gravity. This will be used as a time scale to compare the evolution of different self-gravitating models.

Models without self-gravity are identified by the suffix *turb* and models that consider self-gravity are identified by the suffix *grav*. It is important to remark that there is a small difference in the parameters considered for the purely turbulent models and the ones that consider self-gravity. Some of the models without self-gravity have $\mathcal{M}_A \sim 0.7$, while corresponding models with self-gravity have $\mathcal{M}_A \sim 0.6$. Also, some models without self-gravity have $\mathcal{M}_s \sim 2.0$, while the corresponding models with self-gravity, have $\mathcal{M}_s \sim 1.8$. However, the differences are so small that the comparison between them is not compromised.

We consider an initial temperature $T=10\text{K}$ for all simulations, which is characteristic of molecular clouds, as described in Chapter 1.

In the following Chapter, we present the results of our simulations and comparison between the models with and without self-gravity.

Table 2.1 - Initial conditions for all simulated models, with and without self-gravity

Simulation	\mathcal{M}_s	\mathcal{M}_A	$n(cm^{-3})$	$\beta_0 = \frac{P_{th}}{P_{mag}}$	$t_{ff}(Myears)$	Resolution	Turbulence	Gravity
Ms2.0_Ma0.7_turb	2.0	0.7	117,65	0.302	—	256	yes	no
Ms4.0_Ma0.7_turb	4.0	0.7	444,81	0.080	—	256	yes	no
Ms7.0_Ma0.7_turb	7.0	0.7	1779,25	0.020	—	256	yes	no
Ms2.0_Ma2.0_turb	2.0	2.0	117,65	2.469	—	256	yes	no
Ms4.0_Ma2.0_turb	4.0	2.0	444,81	0.653	—	256	yes	no
Ms7.0_Ma2.0_turb	7.0	2.0	1779,25	0.163	—	256	yes	no
Ms1.8_Ma0.6_256	1.8	0.6	117,65	0.302	7.23	256	yes	yes
Ms7.0_Ma0.6_256	7.0	0.6	1779,25	0.020	1.86	256	yes	yes
Ms1.8_Ma2.0_64	1.8	2.0	117,65	2.469	7.23	64	yes	yes
Ms4.0_Ma2.0_64	4.0	2.0	444,81	0.653	3.72	64	yes	yes
Ms7.0_Ma2.0_64	7.0	2.0	1779,25	0.163	1.86	64	yes	yes
Ms1.8_Ma0.6_grav	1.8	0.6	117,65	0.302	7.23	512	yes	yes
Ms4.0_Ma0.6_grav	4.0	0.6	444,81	0.080	3.72	512	yes	yes
Ms7.0_Ma0.6_grav	7.0	0.6	1779,25	0.020	1.86	512	yes	yes
Ms1.8_Ma2.0_grav	1.8	2.0	117,65	2.469	7.23	512	yes	yes
Ms4.0_Ma2.0_grav	4.0	2.0	444,81	0.653	3.72	512	yes	yes
Ms7.0_Ma2.0_grav	7.0	2.0	1779,25	0.163	1.86	512	yes	yes

Results of the numerical simulations

In this chapter we discuss the results from the 3D numerical simulations performed for this study of turbulent molecular clouds. The parameters of the models are presented in table 2.1. We start by presenting an overview of the general characteristics of the models and then we will separate our discussion between the models without and with self-gravity.

3.1 *General characteristics of the simulated models*

In this section we are going to present two of the models, one sub-Alfvénic and one super-Alfvénic, both with supersonic Mach number $\mathcal{M}_s = 7$, to describe the general evolution of systems that may represent a turbulent molecular cloud environment. These models have a 512^3 resolution.

In Figure 3.1 we show the initial (left column) and final states (right column) of the integrated column density maps of the self-gravitating sub-Alfvénic model with $\mathcal{M}_A = 0.6$, along three different LOS. Figure 3.2 depicts the same for the super-Alfvénic model with $\mathcal{M}_A = 2$. The direction of the projected magnetic field in the plane of the sky (\mathbf{B}_\perp , which is the direction normal to the chosen LOS in each diagram) is also shown and has been produced using a linear integral convolution method (LIC, Cabral and Leedom (1993)). The integrated maps are considered taking the directions perpendicular, at 45° (which will be referred as the XZ line of sight), and parallel to the initial magnetic field (first, second and third lines of the figures), respectively.

In these models, $t = 0.0t_{ff}$ (eq. 1.1) corresponds to the time when the turbulence has completely evolved throughout the domain and reached a nearly steady state regime, before we turn-on self-gravity. Therefore, we can use these models at this stage (which

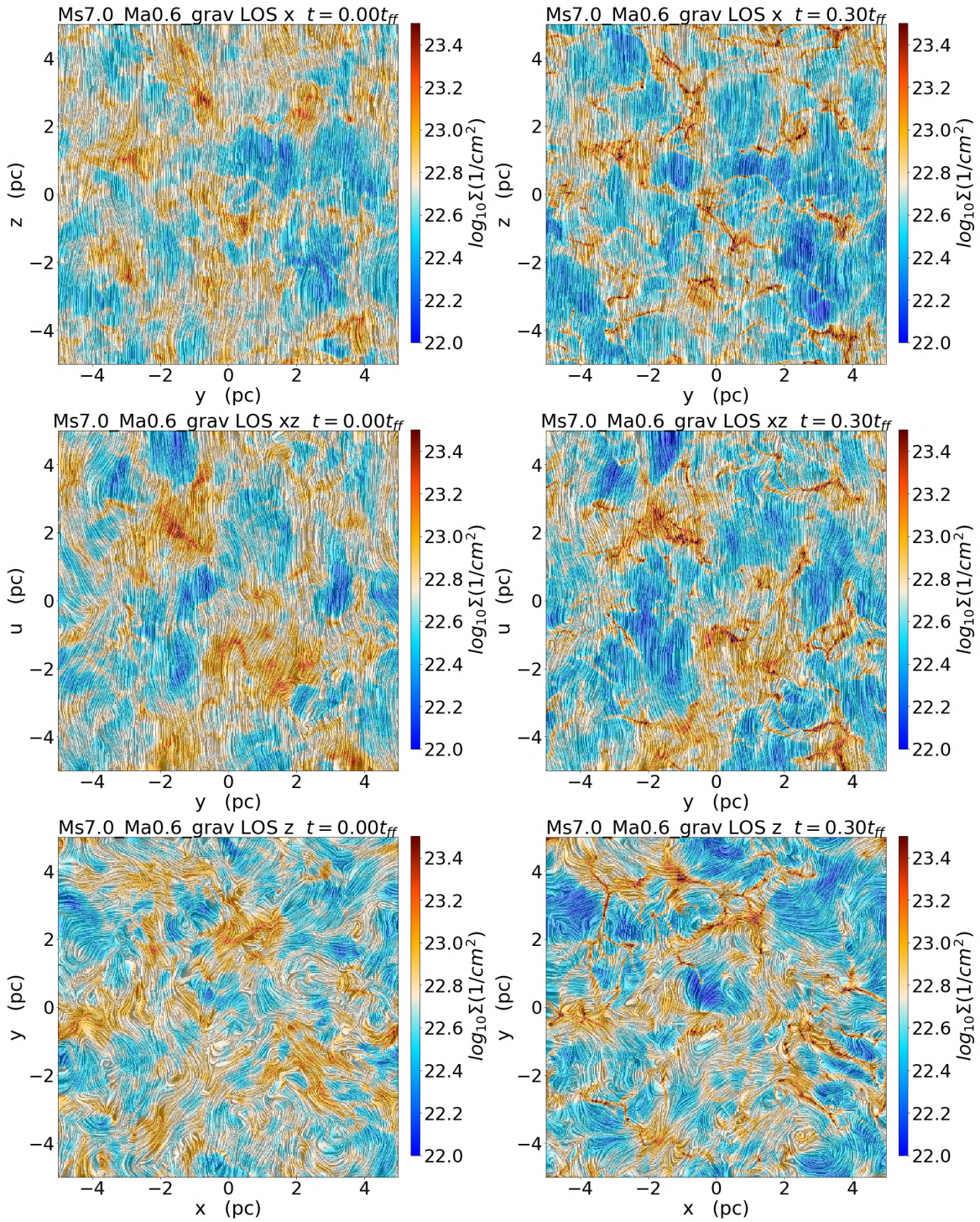


Figure 3.1: Column density maps of the initial ($t = 0.0t_{ff}$) and final ($t = 0.3t_{ff}$) states of model *Ms7.0_Ma0.6_grav* with $\mathcal{M}_s = 7$ and $\mathcal{M}_A = 0.6$ along three different LOS. From top to bottom the LOS is perpendicular, makes an angle of 45° , and is parallel to the initial magnetic field, respectively. The magnetic field is represented by the line pattern using a LIC method. $t = 0.0t_{ff}$ (on the left) corresponds to the time when turbulence has fully developed in the system and is in nearly steady state, right before gravity is turned-on in the system. Thus, the left diagrams correspond to the system without gravity, while the right-diagrams represent the system with self-gravity at an evolved time.

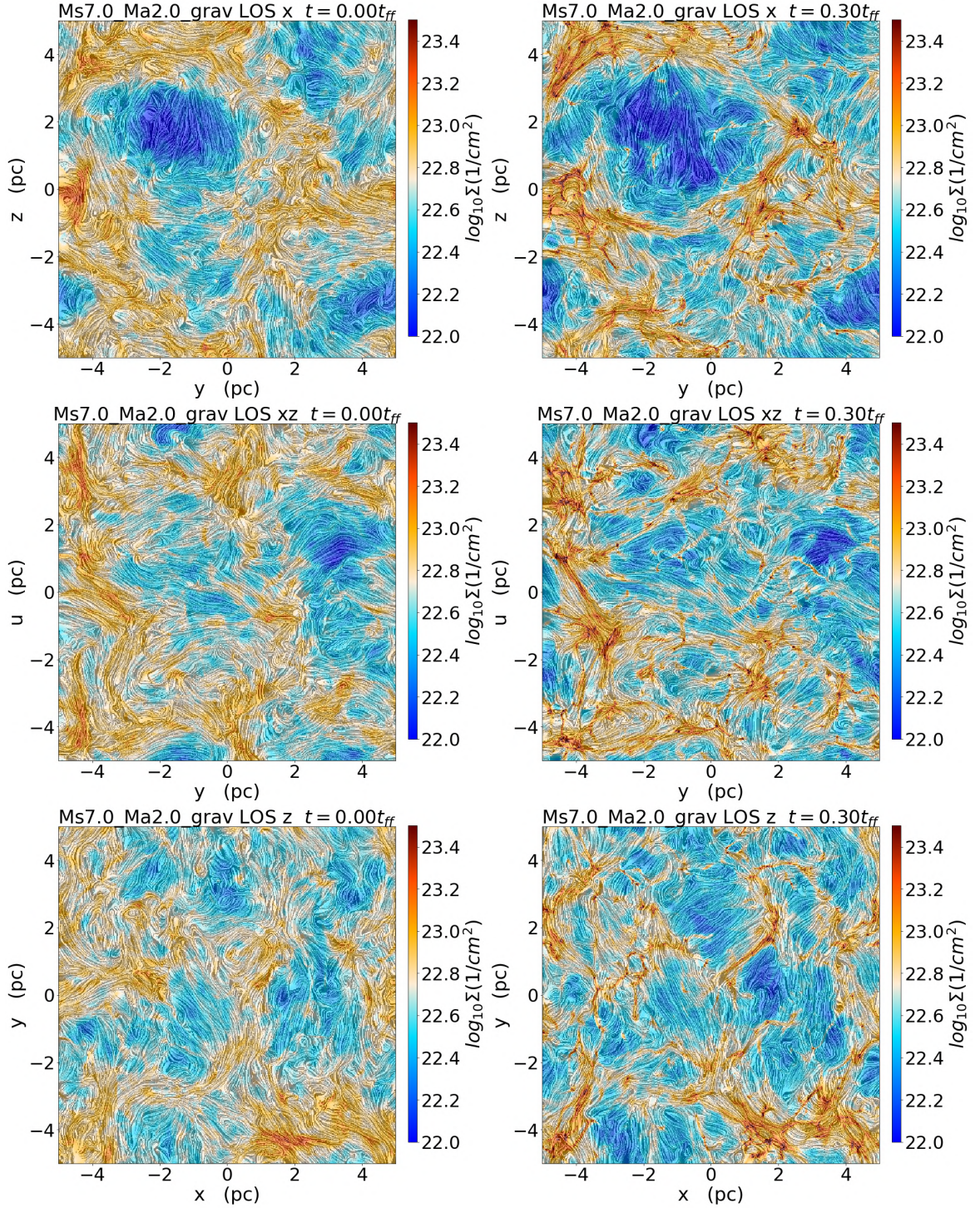


Figure 3.2: The same as in Figure 3.1, but for the super-Alfvénic model with $\mathcal{M}_A = 2$.

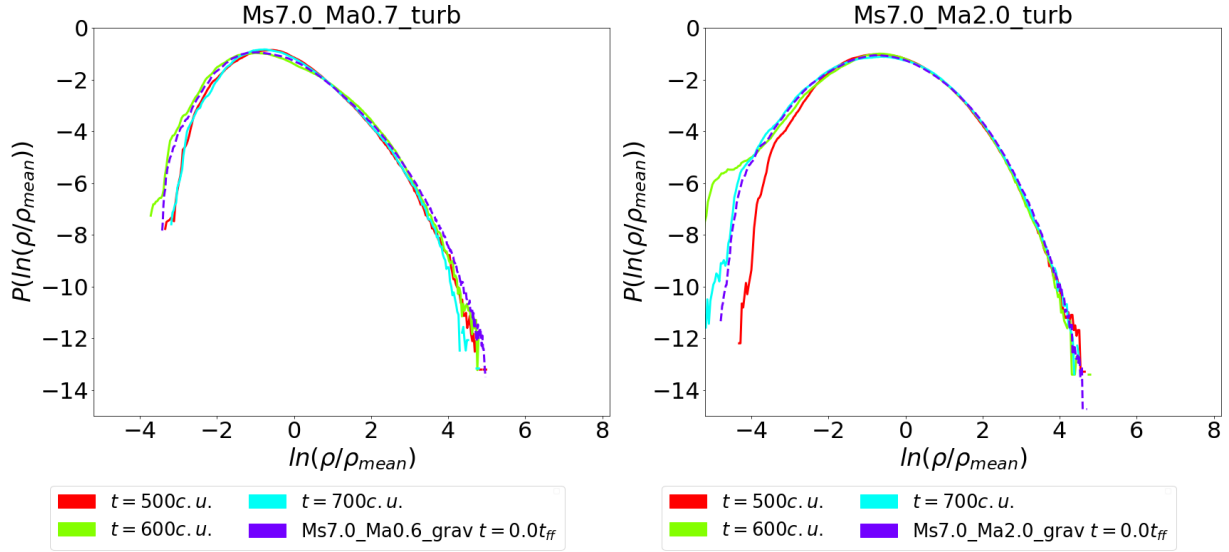


Figure 3.3: Comparison of the 3D PDF of density between turbulent models with no self-gravity (solid lines) and the initial state of the corresponding model with self-gravity (dashed line). The sub-Alfvénic models are presented on the left and the super-Alfvénic ones are presented on the right side.

are shown in the left columns of Figures 3.1 and 3.2), as representative of models without self-gravity. In fact, Figure 3.3 shows the probability distribution function (PDF) for the density (eq. 2.7) of evolved supersonic sub-Alfvénic, and super-Alfvénic models with same initial conditions as those of Figures 3.1 and 3.2, but without gravity. These PDFs are compared to their counterparts of the models of Figure 3.1 and 3.2 at $t = 0.0t_{ff}$ (before self-gravity is set in). We see that they are completely equivalent, therefore justifying our statement above.

Figure 3.4 depicts three-dimensional views of the models of Figures 3.1 and 3.2 before (left) and after (right) self-gravity is turned on. On the top of figure 3.4, it is shown the supersonic, sub-Alfvénic model *Ms7.0_Ma0.6_grav* and in the bottom the supersonic super-Alfvénic model *Ms7.0_Ma2.0_grav*. Once gravity is considered (right-diagrams), fragmentation and filamentary structure formation is enhanced and the collapse of the densest regions (clumps) of these filaments leads to star formation.

A closer inspection of the models of Figure 3.4 shows that the distribution of the lines is determined mainly by turbulence, and this effect is more pronounced in the case of super-Alfvénic turbulence. What determines if the lines become almost parallel or perpendicular to a given structure, or if they are twisted inside the domain is whether the turbulence is sub-Alfvénic or super-Alfvénic. The twisting of the lines is stronger in the super-Alfvénic

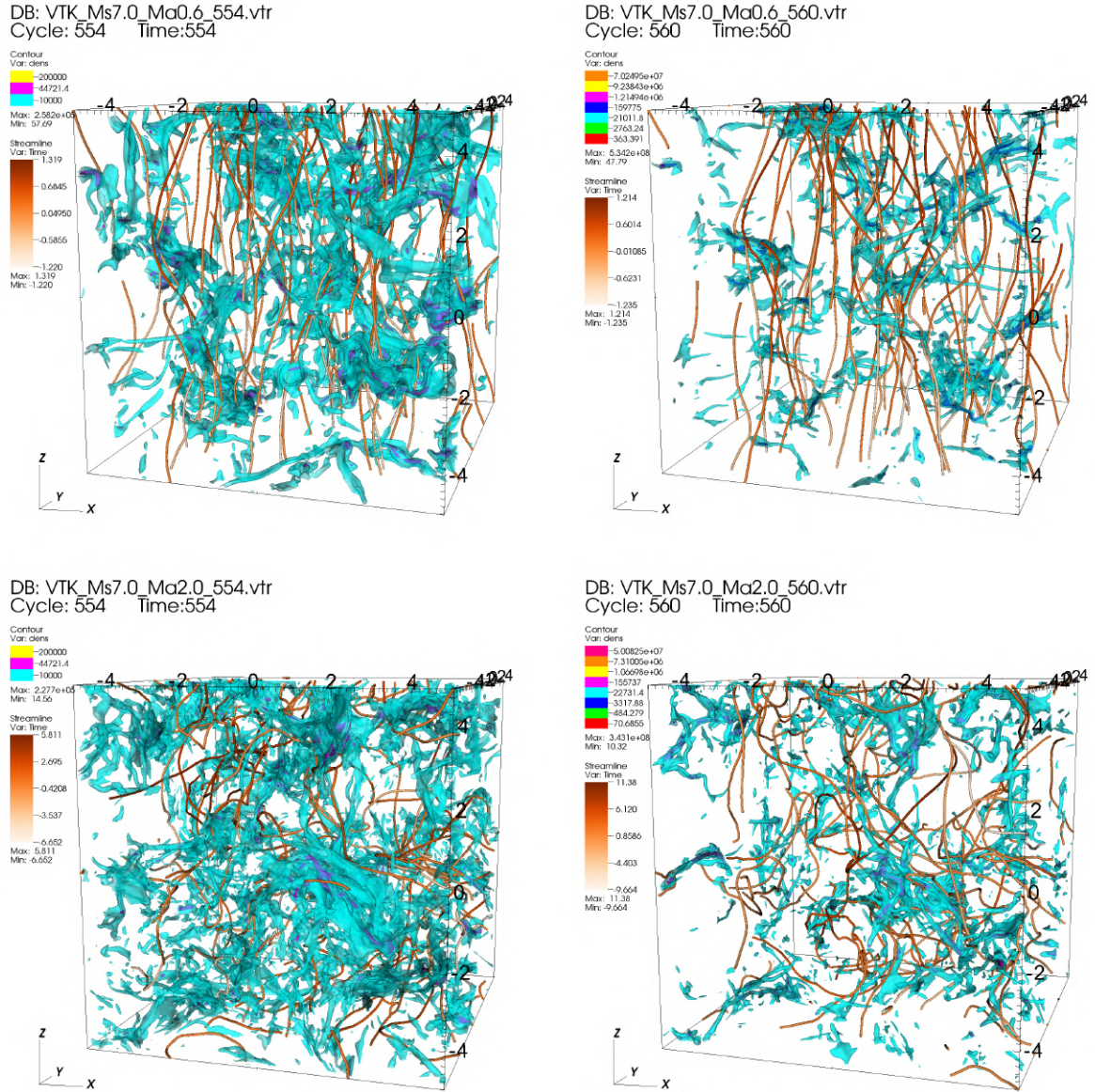


Figure 3.4: Comparison of the 3D distribution of density and magnetic fields for the initial ($t = 0.0t_{ff}$)(without self-gravity) and final ($t = 0.3t_{ff}$) states (with gravity) for models *Ms7.0-Ma0.6_grav* (top) and *Ms7.0-Ma2.0_grav* (bottom). See text for details.

case due to the larger turbulent motions relative to magnetic field strength. This also affects filaments, which appear more chaotically distributed with respect to the magnetic field lines when magnetic field is weaker. In the case of the sub-Alfvénic model, we see that the lines are less distorted by turbulence and later on, when self-gravity becomes dominant, most of the filaments seem to be nearly normal to the magnetic field lines (right top diagram), as the collapse is easier along the lines (since in the perpendicular direction magnetic pressure gradients try to prevent it).

Back to Figures 3.1 and 3.2, as they present the integrated density distribution along given LOS, they are more suitable to compare directly with observations (as we will see in Chapter 4). In particular, the top diagrams of these figures (which show the column density integrated in a LOS perpendicular to the initial 3D magnetic field, \mathbf{B}), reflect directly the integration of the multiple layers we see in the 3D diagrams of density distribution of Figure 3.4, while the bottom diagrams (of Figures 3.1 and 3.2) show this integration in the normal direction to the initial \mathbf{B} .

The comparison between Figures 3.1 and 3.2 also shows that both depict dense filaments separated by diffuse interstellar gas, but these structures when seen integrated along a LOS are clearly larger in the super-Alfvénic models (this can be also realized in Figure 3.4 in the earlier phase, when only turbulence is present, bottom left panel). This effect is more pronounced in the LOS perpendicular to the initial \mathbf{B} . Supersonic turbulence leads to shocks and compression of the fluid and of the magnetic field lines, particularly in the early phase, before self-gravity sets in. In the case of the super-Alfvénic models, these effects are more efficient in the building-up of larger structures because the magnetic field strength is smaller than in the sub-Alfvénic models. In the latter, the larger magnetic field strength results stronger magnetic pressure gradients, that offer larger resistance to the accumulation of the structures by shock compression. When self-gravity becomes important (right panels), fragmentation and collapse will eventually dominate over the support provided by magnetic fields and turbulence in both cases, but the general imprints left earlier in the formation of the large scale filaments by turbulence and magnetic fields (left panels) remain.

In the sub-Alfvénic models (Figure 3.1) there is a clear difference between different LOS, with \mathbf{B}_\perp being almost completely parallel to the Z axis for the first LOS, and with no preferential direction for the last one. In the super-Alfvénic models of Figure 3.2, on

other hand, \mathbf{B}_\perp does not have a clear difference for different LOS. This is equally due to the effects described above, i.e., to the fact that the magnetic forces offer less resistance to the turbulent motions and collapsing of the structures in the super-Alfvénic case.

While turbulence is important to create structures that will become gravitationally unstable regions, it can also act against star formation, destroying cores that could later form stars.¹ The magnetic field has then a role of shielding matter against turbulence and allowing it to accumulate for a longer time forming numerous dense structures, as we see in the sub-Alfvénic model when gravity is present (right side top diagram). For the super-Alfvénic model the weaker magnetic field is less effective to keep the coherence of the structures during collapse and the filaments are more easily fragmented by turbulence, leading to smaller and more numerous clumps. Though not so obvious in Figures 3.1, 3.2, and 3.4, this effect will be highlighted in the next sections. This has been particularly realized in previous works (e.g. Myers et al. (2014); Ntormousi and Hennebelle (2019)).

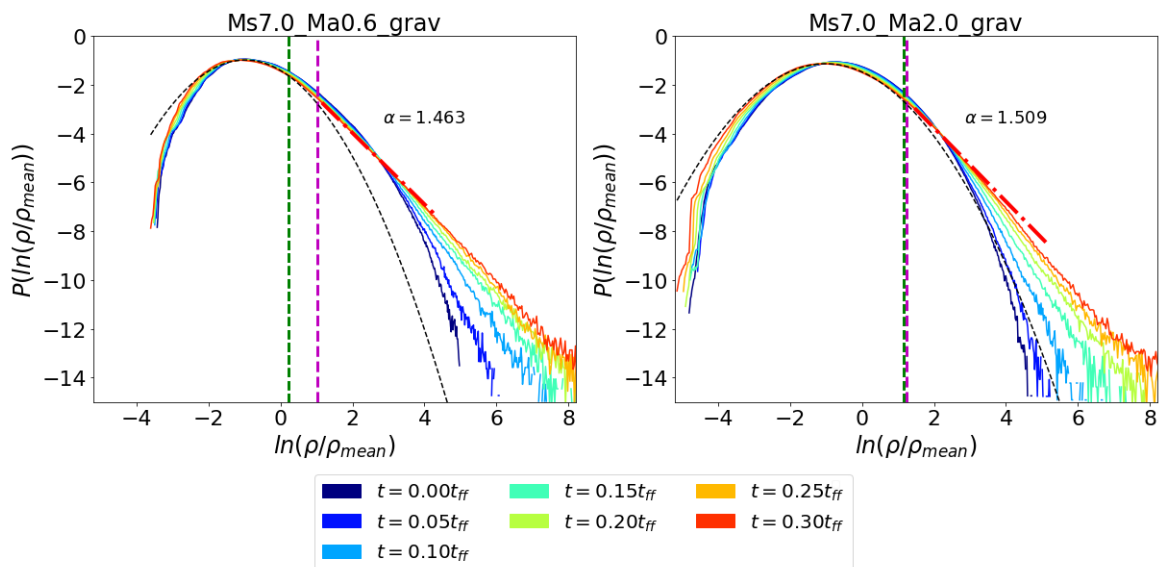


Figure 3.5: Time evolution of the density PDF for models *Ms7.0_Ma0.6_grav* (left) and *Ms7.0_Ma2.0_grav* (right). The green vertical dashed line indicates the critical density for star formation (eq. 2.14). The magenta vertical dashed line represents the transition density as defined in eq. 2.11. The black dashed line and the red dashed-dotted line are the fitted lognormal and power-law to $t = 0.3t_{\text{ff}}$, respectively.

Figure 3.5 compares the evolution of the PDF of the density (eq. 2.7) for the two models analysed in the previous figures. The sub-Alfvénic model is presented in the left

¹ The turbulence drive is continuous and random. This can lead to turbulence being driven in cells that could result in collapsed cores, therefore destroying or at least reducing the final mass of these cores.

and the super-Alfvénic one, in the right panel. The blue dark curve represents $t = 0.0t_{ff}$. Initially, the super-Alfvénic model shows a wider spread of density values when compared to the sub-Alfvénic model.

The sub-Alfvénic model shows earlier a small tail that deviates from the lognormal distribution, which is not present in the super-Alfvénic case. Since at this stage, gravity is not acting in the system, this deviation from the lognormal is most likely caused by the presence of a strong magnetic field. At later times, the power-law reflects of the action of gravity, as discussed in Chapter 1.

Since our version of the code does not support any treatment of adaptive mesh refinement or sink particles, we consider that our results are valid until the power-law index reaches a value $\alpha \sim 1.5$. This has been chosen in accordance to previous studies that indicate power-law tails from observed clouds with an index up to this value (see table 1 from Burkhart (2018) and references therein). In fact, the evolution of the cloud should result in a power-law with an index that converges to -1 . However, effects due to the lifetime of the MC or to the LOS may yield higher values for the observed power-law index (Girichidis et al. (2014); Guszejnov et al. (2018)).

The black dotted line is the fitted lognormal PDF (P, eq. 2.7) for $t = 0.3t_{ff}$ and the red dashed-dotted line is the power-law fitted for the same time. The fitted index, and the region where the fit was considered, are indicated in the plot. The magenta vertical dashed line is the estimated s_t (eq. 2.11) for the fitted power-law index and the green vertical dashed line is the critical density for the magnetized case, equation 2.14. We note that both coincide in the case of the super-Alfvénic model. As the material collapses and the power-law becomes shallower, s_t (eq. 2.11) should also go to smaller densities, eventually approaching ρ_c (Burkhart (2018)).

Although this may not be a very strict condition, we want to investigate the influence of gravity over filaments and magnetic field distribution in the early stages of star formation. This condition coupled with the information from the power spectrum, that will be discussed below, will allow us to identify how much the system is being affected by gravity and to estimate how long the dense regions are taking to collapse.

Figure B.3 shows the 3D power spectrum of density evolution in time for the same two models. The dotted red line is a reference to the expected power-law from a Kolmogorov cascade ($P(k)dk^3 \propto k^{-11/3}$, see section 1.2.1). Initially, in both simulations it is possible to

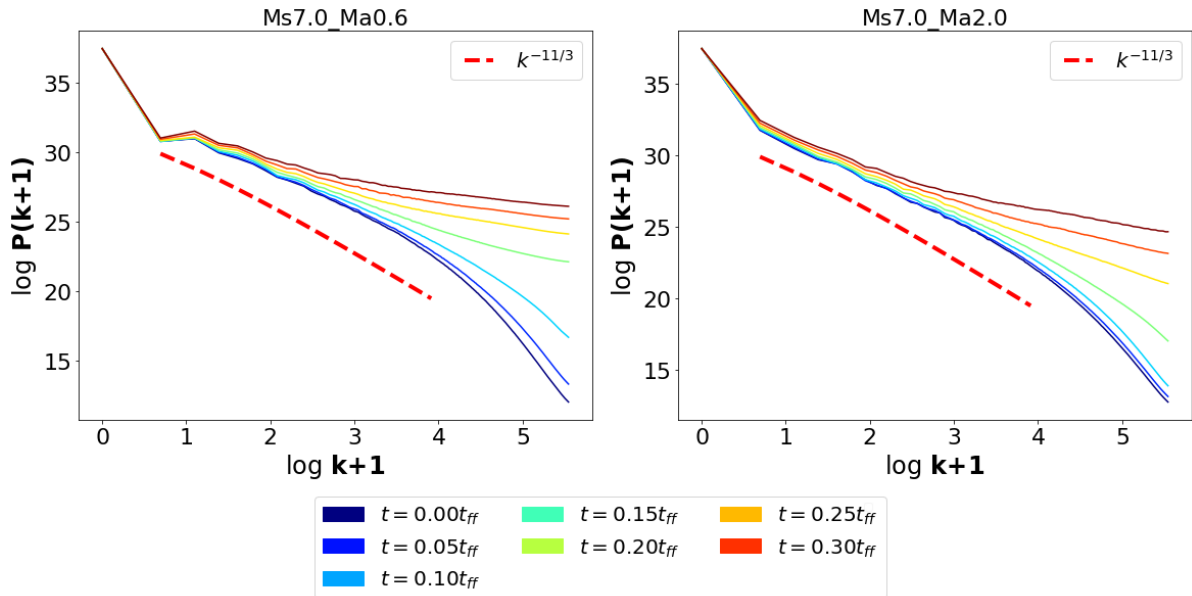


Figure 3.6: 3D power spectrum of density for models with $\mathcal{M}_s = 7.0$ that do consider self-gravity. On the left we have $\mathcal{M}_A = 0.6$ and on the right we have $\mathcal{M}_A = 2.0$. The red dashed line represents the Kolmogorov power-law ($k^{-11/3}$) for reference.

identify a inertial region in the spectrum that roughly follows the same Kolmogorov slope. As time goes by, as it is seen from the PDFs of Figure 3.5, gravity becomes important at denser regions, which are also the smallest scales in the system. As matter accumulates around these overdense regions, the power spectrum at higher wavenumbers (k) (or smaller length scales) starts to flatten.

This flattening can also be seen in Figure 3.7, where the one-dimensional power spectrum of the column density maps is shown for three different LOS. Although for $t = 0.0t_{ff}$ the power spectrum seems a little bit steeper than $k^{-5/3}$ (which is compatible with a one-dimensional Kolmogorov spectrum), at latter times it becomes almost completely flat. Previous studies (e.g. Burkhardt et al. (2015)), actually found positive slopes due to gravity acting at the smallest scales. That is not the case in our models, but as it was mentioned before, since we cannot follow the later evolution of collapsing structures because of the lack of an adaptive mesh refinement, we have stopped our simulations at earlier times of the cloud’s evolution than those achieved in the studies of Burkhardt et al. (2015).

Other authors have studied in detail the statistical properties like the PDF and power spectrum of structure formation in star forming regions in the ISM and obtained similar results (e.g., Federrath and Klessen (2013); Burkhardt et al. (2015)) and we refer to these

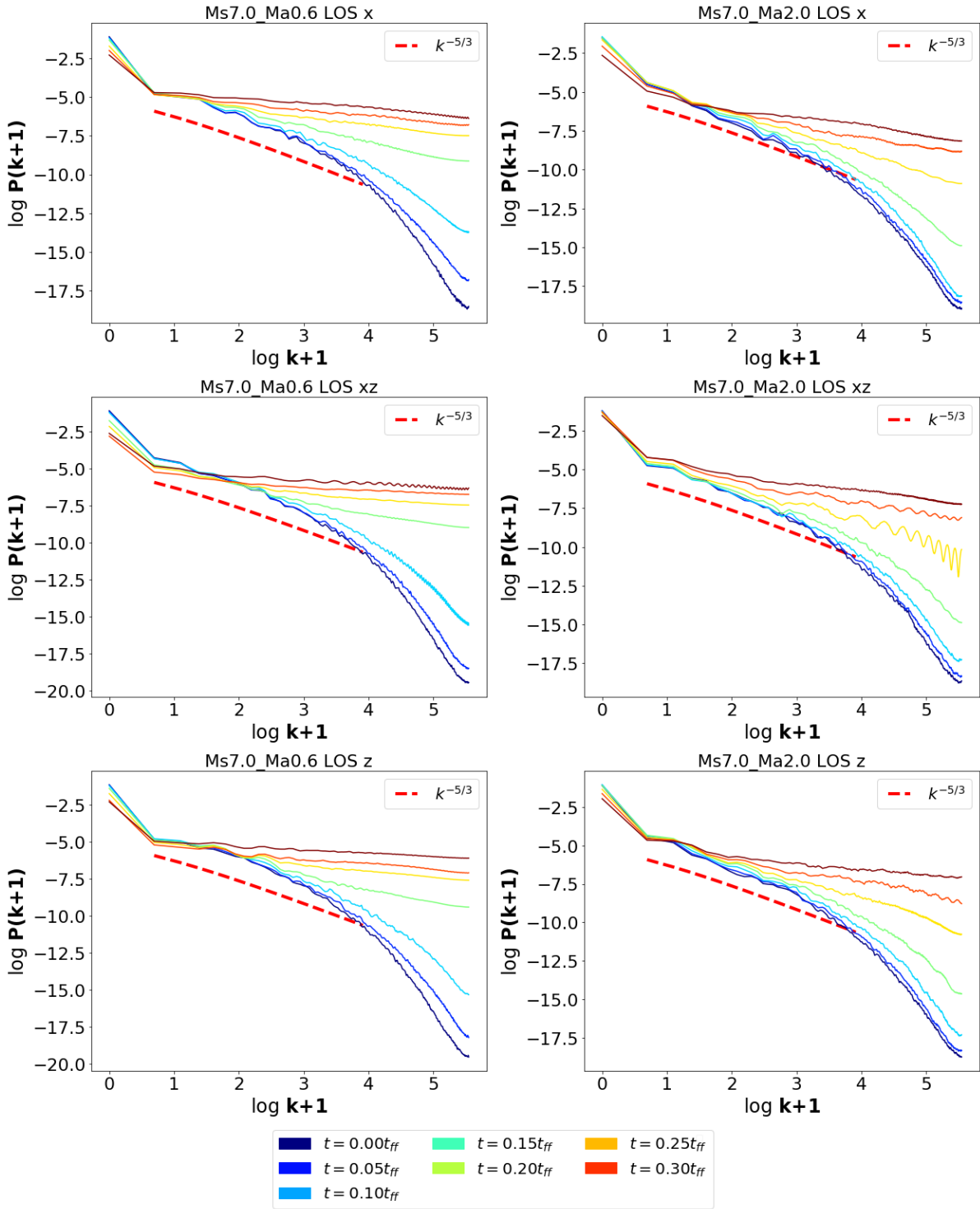


Figure 3.7: 1D power spectrum of column density for models with $\mathcal{M}_s = 7.0$ that do consider self-gravity along three LOS. The direction along which the map was integrated is indicated above each plot. On the left we have $\mathcal{M}_A = 0.6$ and on the right we have $\mathcal{M}_A = 2.0$. The red dashed line represents the Kolmogorov power-law ($k^{-5/3}$) for reference.

studies for more details. In Appendix B we show the PDFs and power-spectrum of other models investigated in this work.

In the next section we are going to analyse the morphology of the filaments and how they distribute with respect to the magnetic fields and the turbulence.

3.2 Simulations without self-gravity

The results presented below (simulations performed by Cho and Lazarian (2003); Burkhart et al. (2009)) were taken after the run of several turnover times of the entire turbulence development, when then the system attained a nearly steady state. The initial conditions for these models are described on table 2.1. As stressed on Chapter 2, no self-gravity is included in this set of simulations, only turbulence and thermal motions can modify the magnetic field and vice-versa. Also, we remark that the models considered in this section use a resolution of 256^3 Cho and Lazarian (2003); Burkhart et al. (2009), which is enough to study the effects of turbulence, as stressed in Section 2.3. Higher resolution (512^3) models are used to study the effects of self-gravity in Section 3.3.

In the previous section, it was presented the general behaviour of the models. Below we are going to analyze in detail how the magnetic field distribution is affected by the turbulence. We will begin with integrated maps obtained from the simulations.

Figure 3.8 shows the PRS analysis for all the sub-Alfvénic models and for the three different lines of sight (LOS) (see section 2.2.1). First, when the LOS is perpendicular to the initial field, Z_E has a steeper variance for higher densities. In the case of the models with the line of sight parallel to the initial field, the values have a smaller variance with density growing for all the sub-Alfvénic models. Positive values of Z_E indicate that \mathbf{E} is parallel to ∇N_H , which indicates that the projected magnetic field in the plane of sky (\mathbf{B}_\perp) is parallel to the iso-contours of N_H . When the LOS is along X , i.e. parallel to the initial magnetic field, the PRS analysis returns only positive values for most densities with very little variation. This happens because \mathbf{B}_\perp in this case results from motions perpendicular to the main component of the field and this results in a random field distribution as seen in Figure 3.9 (see more below).

In Figure 3.9, the Linear Integral Convolution (LIC) method was applied to \mathbf{B}_\perp and the resulting image was superimposed on the column density maps of the same models of Figure 3.8, but only for $t = 600c.u.$. Comparing the maps integrated along X with their respective PRS (right diagrams in both figures), Z_E indicates that \mathbf{E} is parallel to the gradient of density and so \mathbf{B}_\perp is mostly parallel to the filaments. The maps for LOS along X from Figure 3.9 show that \mathbf{B}_\perp has a spatial distribution quite different from the other two LOS. The coherence length is smaller in this LOS. Since we are projecting only

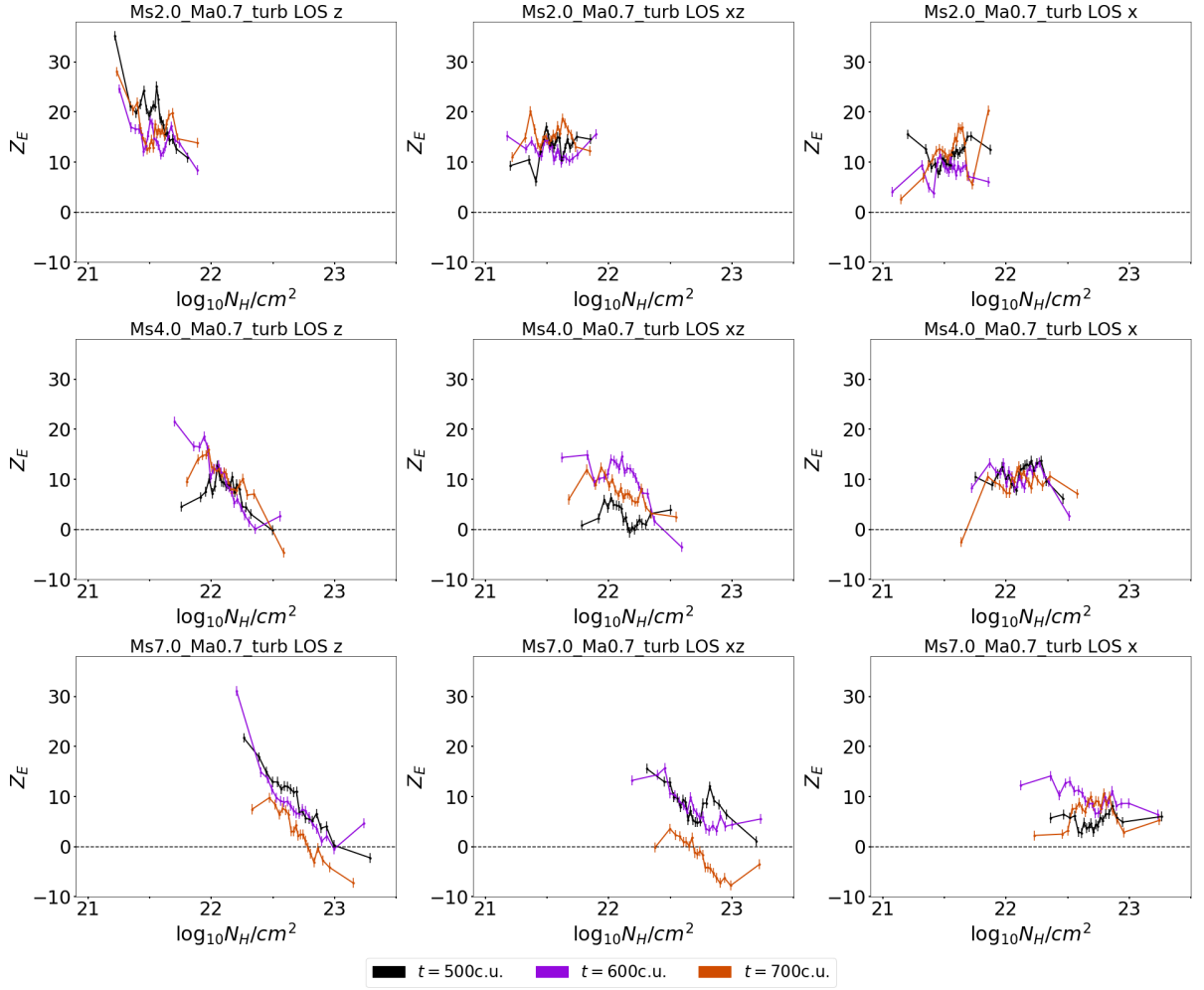


Figure 3.8: PRS time evolution for all sub-Alfvénic models (with $\mathcal{M}_A = 0.7$) without self-gravity. From left to right the PRS is applied to the LOS along Z (the direction perpendicular to the initial field), XZ (45° with regard to the initial field) and X (perpendicular to the initial field) directions. From top to bottom initial $\mathcal{M}_s = 2.0, 4.0, 7.0$, respectively.

the plane of the sky component of the field, we do not see the main component, only perturbations perpendicular to it.

In the other LOSs of Figure 3.9, as the sonic Mach number is increased (keeping the same $\mathcal{M}_A = 0.7$), and specially at later times when denser structures form, we identify some negative values in the PRS, for the largest column densities. This indicates that, when observed from these LOS, the densest structures tend to be more aligned with the local projected magnetic field to the plane of sky. This seems to be counter-intuitive to what one should expect, since this effect seems to be larger for larger turbulent motions (larger \mathcal{M}_s) relative to the magnetic field strength, where compression effects should be even stronger. However, looking at the column density maps of Figure 3.9, we note that

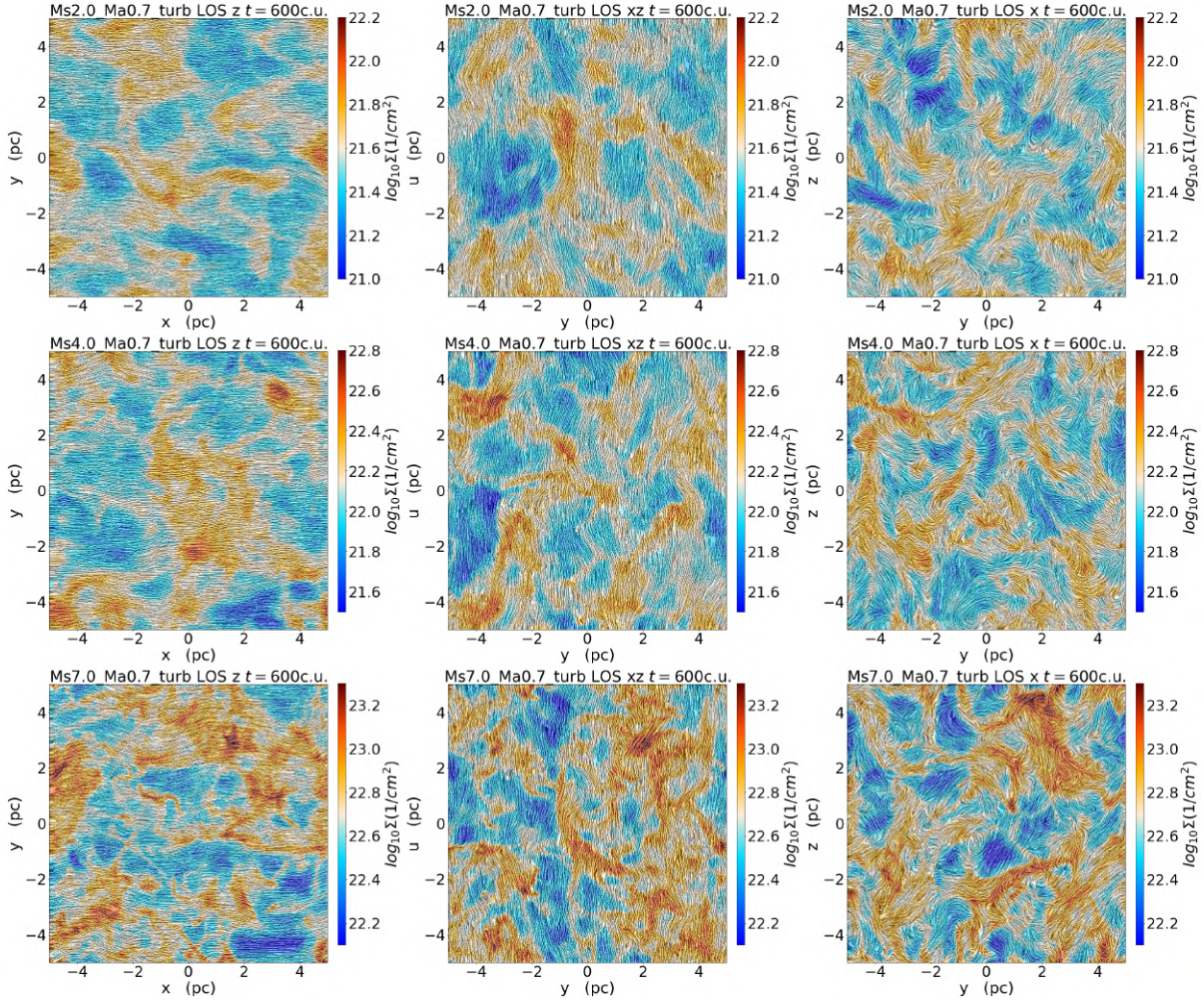


Figure 3.9: Column density maps with LIC method applied to \mathbf{B}_\perp for the same models presented in Figure 3.8. The time $t = 600c.u.$ was used to illustrate what is seen in these integrated maps of Figure 3.8. From left to right the integrated LOS is along Z (the direction perpendicular to the initial field), XZ (45° with regard to the initial field) and X (perpendicular to the initial field) directions. From top to bottom initial $\mathcal{M}_s = 2.0, 4.0$ and 7.0 , respectively.

the increase of turbulence (increase of \mathcal{M}_s) causes more fragmentation and the formation of more numerous smaller and denser structures. This effect is more pronounced for the LOS along Z (where the projected magnetic field to the sky has a larger component aligned to the original magnetic field) and less pronounced as we go to the LOS along X (where the projected magnetic field to the sky has a smaller component aligned to the original magnetic field). In other words, in these sub-Alfvénic models, only the densest and smallest structures that develop from increased fragmentation in the more turbulent models (larger \mathcal{M}_s) at latter stages of evolution, tend to align with the intrinsic magnetic fields, and this effect is observable only for LOS perpendicular or with angles around 45° to the original

field.

When $\mathcal{M}_A = 2.0$ (therefore, decreasing the strength of the magnetic field relative to the turbulent motions), the PRS does show positive values and thus aligned structures to the projected magnetic field for all LOS (see Figure 3.10). In this case the magnetic field is not strong enough and it wanders due to the turbulence, it is compressed by it, and thus cannot keep a large coherence, mostly following the fragmented filaments. For most of the super-Alfvénic cases the behaviour the PRS is closer to what is seen in the maps integrated along X in the sub-Alfvénic case. Therefore, in general, the magnetic field presents itself parallel to the filaments. In some cases, it is possible to see a behaviour that is completely opposite to the sub-Alfvénic case (Figure 3.8), with Z_E actually increasing with N_H .

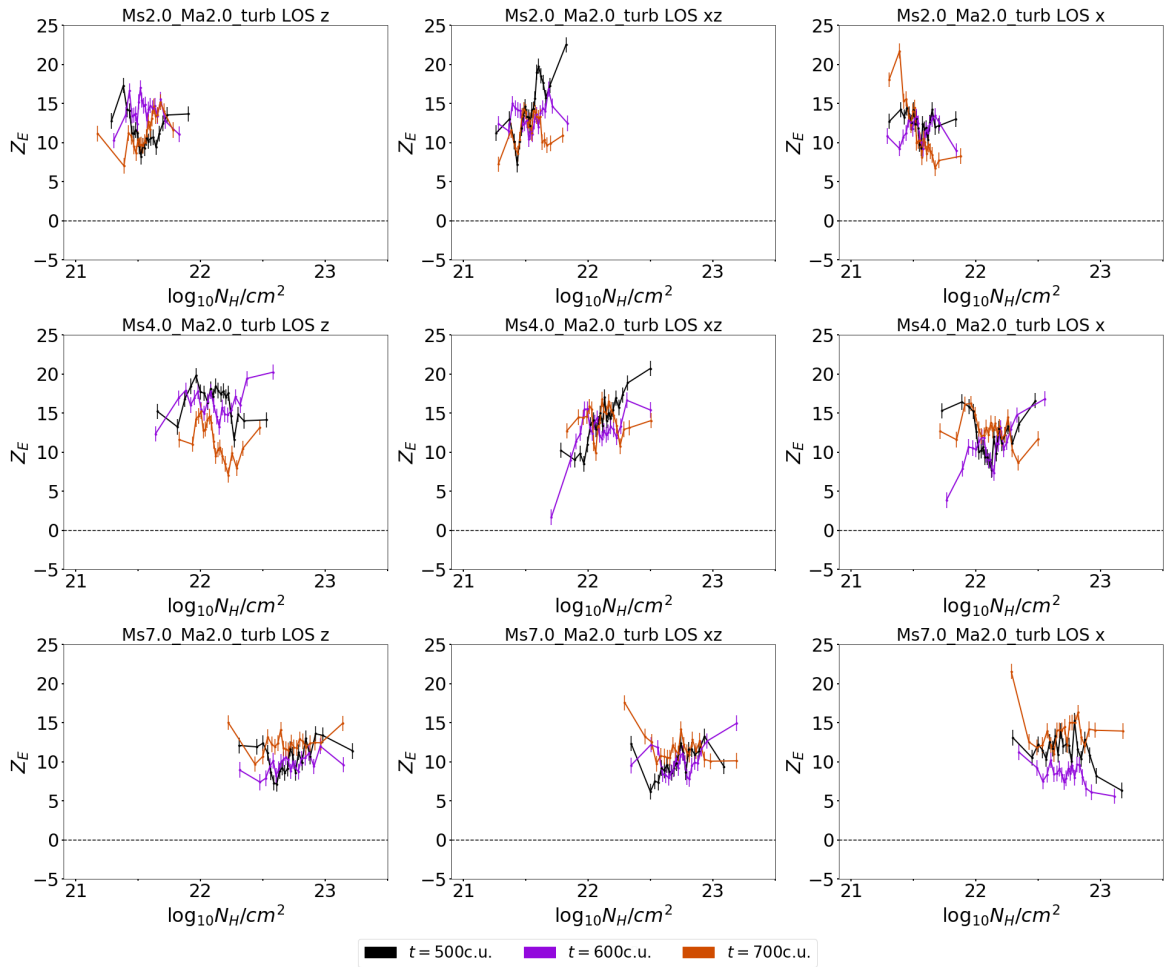


Figure 3.10: PRS time evolution for all super-Alfvénic (with $\mathcal{M}_A = 2.0$) models without self-gravity. From left to right the PRS is applied along Z (the direction perpendicular to the initial field), XZ (45° with regard to the initial field) and X (perpendicular to the initial field) directions. From top to bottom initial $\mathcal{M}_s = 2.0, 4.0$ and 7.0 , respectively.

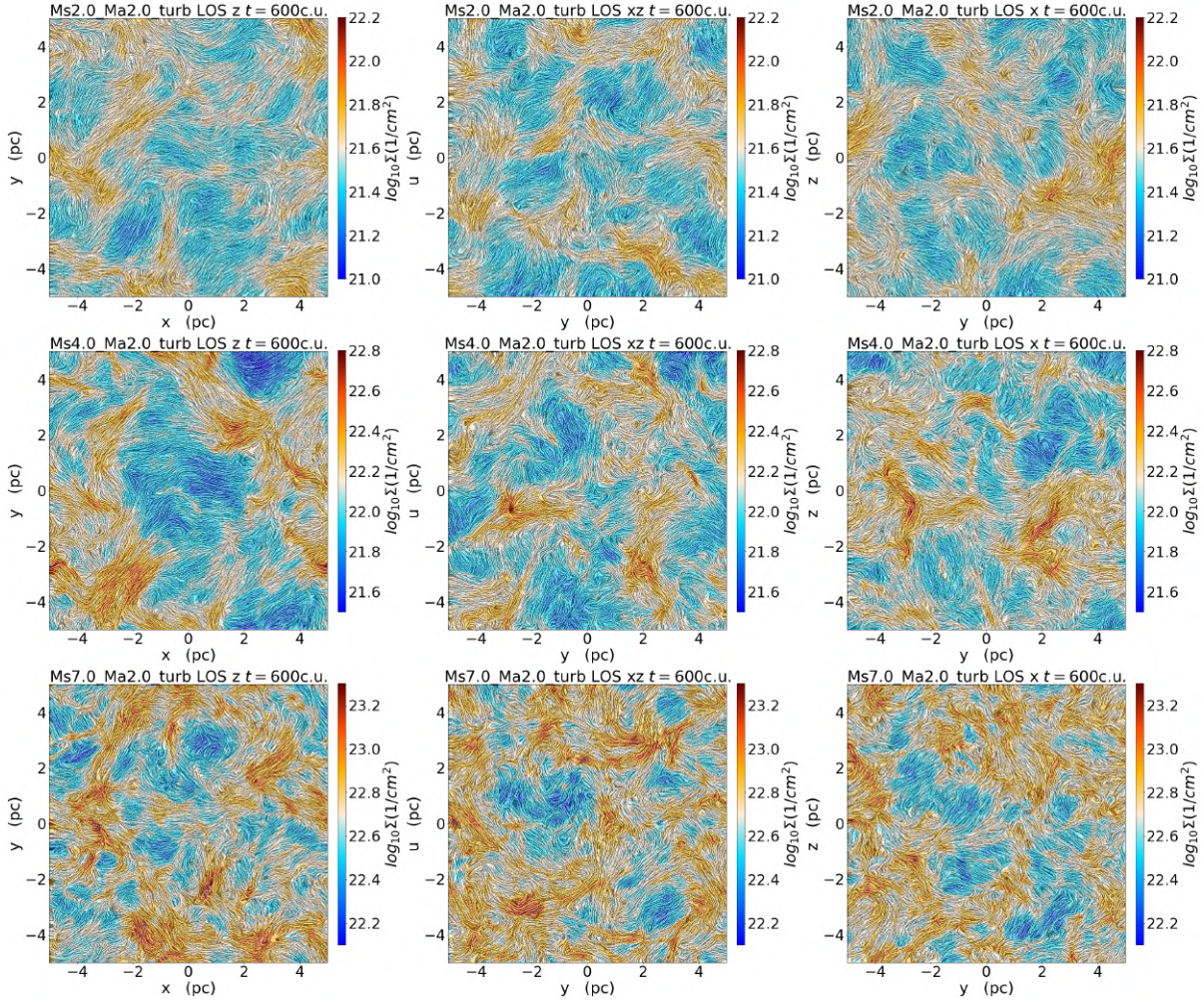


Figure 3.11: Column density maps with LIC method applied to \mathbf{B}_\perp for the same models presented in Figure 3.10. The time $t = 600c.u.$ was used to illustrate what is seen in these integrated maps. From left to right the column density distribution is integrated along Z (the direction perpendicular to the initial field), XZ (45° with regard to the initial field) and X (perpendicular to the initial field) defined directions. From top to bottom initial $\mathcal{M}_s = 2.0, 4.0$ and 7.0 , respectively.

Figure 3.11 shows the column density maps and the LIC method applied along \mathbf{B}_\perp direction for the super-Alfvénic models, similar to Figure 3.9. Comparing both images, it becomes clear how the LOS direction is important in the sub-Alfvénic cases (Figure 3.9), but when it comes to the super-Alfvénic simulations the influence is not as clear. We also identify another important difference with regard to Figure 3.9, where we can see that the coherence length of \mathbf{B}_\perp is smaller for all LOS in Figure 3.11.

Figure 3.12 depicts Z_B analysis (see section 2.2.1) for all models without self-gravity. This analysis method indicates that the overall gradient of density is mostly perpendicular to \mathbf{B} (and hence, structures are mostly aligned with the intrinsic magnetic fields), since

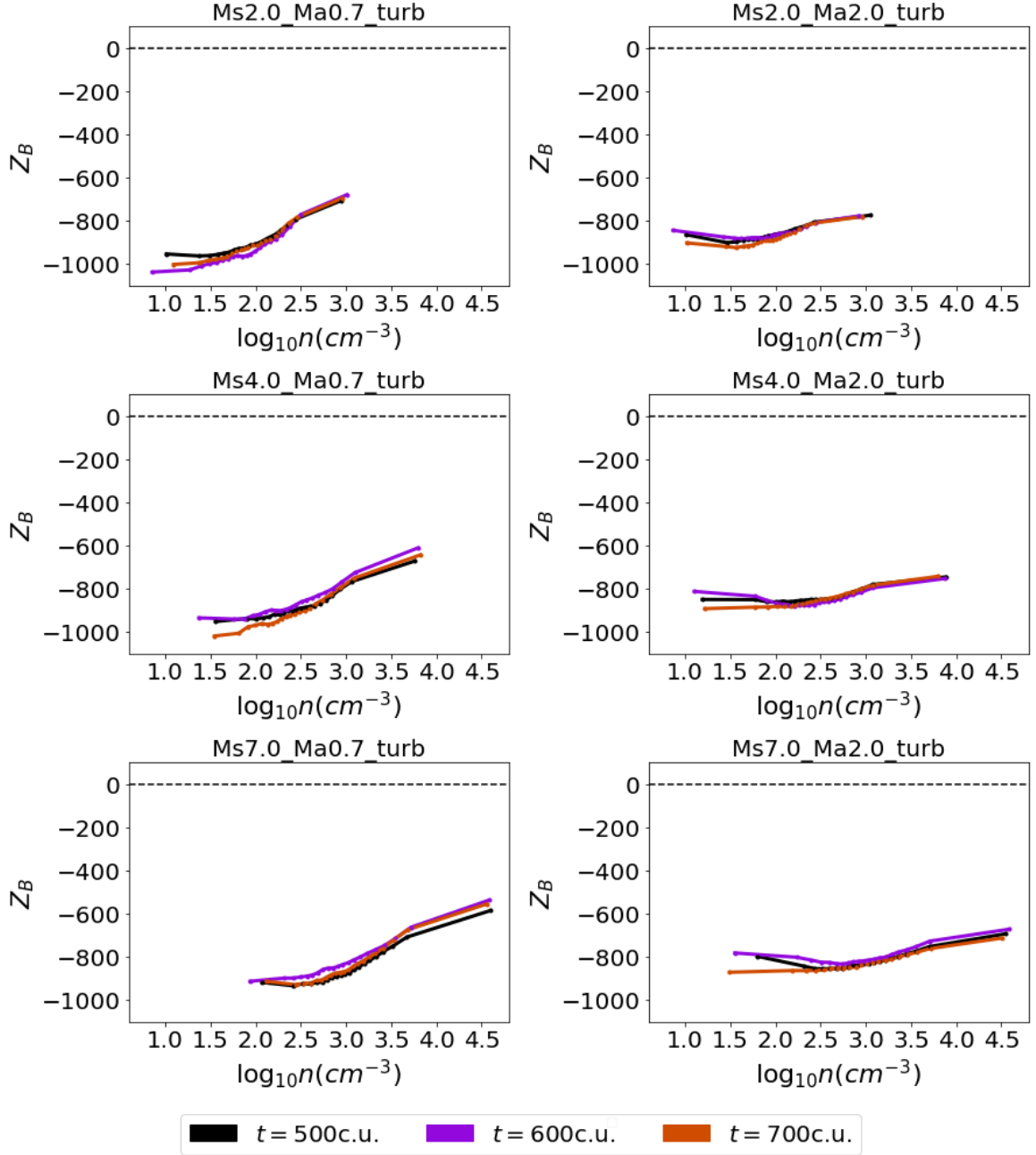


Figure 3.12: Z_B analysis (equation 2.21) applied to the 3D distribution of density and magnetic fields for all simulated models without self-gravity (see table 2.1) for 3 different. On the left are presented the sub-Alfvénic (initial $\mathcal{M}_A = 0.7$), and on the right super-Alfvénic (initial $\mathcal{M}_A = 2.0$) models. From top to bottom initial $\mathcal{M}_s = 2.0, 4.0$ and 7.0 , respectively.

Z_B is negative for all densities. This applies to both set of simulations, sub-Alfvénic and super-Alfvénic. The sub-Alfvénic models show slightly higher values of Z_B towards denser regions compared to their super-Alfvénic counterparts. These results indicate that the compression of the lines by the gradient of pressure is the dominant factor due to the supersonic turbulence. Higher sonic Mach numbers mean a higher compression of the lines in the direction parallel to the gradient of density (pressure) and perpendicular to \mathbf{B} , resulting the alignment of the magnetic field with the density filament. Now, as the system gets more and more sub-Alfvénic, \mathbf{B} will be more intense and offer a greater resistance to compression. Besides, as we go to higher densities, we see that Z_B in the super-Alfvénic is more negative than in the sub-Alfvénic systems.

The conclusion obtained from the Z_B analysis performed above over the density distributions, seems to be at first sight, a little in contradiction with the Z_E analysis performed before for the column density distributions of the turbulent models without self-gravity, at least for the densest structures. However, the fact that no positive values of Z_B appear does not mean that there are no regions where $\nabla\rho$ is parallel to \mathbf{B} (i.e., where dense filaments are normal to the intrinsic magnetic fields). The first step to calculate the PRS (both for density and for column density distributions) is to divide the density distribution into bins (density intervals) with the same number of cells (see Soler et al. (2013)) and then Z_B (for density) and Z_E (for column density) are calculated inside each bin. Since at very high densities we have fewer structures, the last bin includes structures that have very different values of density and therefore may have very different alignment with the field. As we will see below, the HRO can help to distinguish the presence of perpendicular filaments in the densest regions.

In this work, all the PRS calculations have considered 20 bins, both for Z_B and Z_E . As we will see below, the information provided by both criteria Z_E and Z_B must be seen as complementary to provide a whole picture of the relative distributions of the structures and their magnetic fields.

To exemplify the distribution of angles at different density bins, Figure 3.13 shows the histograms of relative orientations (HRO) (histogram of eq. 2.15, section 2.2) for two different models, *Ms7.0-Ma0.7_turb* (left) and *Ms7.0-Ma2.0_turb* (right). With ϕ being the angle between the gradient of density and the local magnetic field (eq. 2.15), $\cos(\phi) = 0$ means that \mathbf{B} is perpendicular to the gradient while $\cos(\phi) = \pm 1$ indicates that these two

vectors are parallel. The 3D distribution of the density structures in space for these models is similar to what is seen in the left side of Figure 3.4 for the respective sub and super-Alfvénic models. In the histograms, we can understand how the filaments and density structures behave at different density intervals.

Both plots in fig. 3.13 show 6 density bins for each model. In the sub-Alfvénic case (left) the distribution of $\cos \phi$ shows a clear peak around zero for every bin, except for the densest one, where the histogram is almost flat, meaning that there are more or less the same number of structures parallel and perpendicular to the field lines at this density bin (this is compatible with our previous analysis of Figures 3.8 and 3.9). At the same time, when we look to the super-Alfvénic model (right), even when for the densest regions in the domain there is a higher count of $\cos \phi$ around zero, i.e. with the structures mostly aligned to \mathbf{B} at all densities (which is also compatible with the previous analysis).

The change in alignment at different densities, specially for the sub-Alfvénic models, reflects in the PRS analysis, as there are less negative values for Z_B as we go to denser regions (Figure 3.12). However, these regions are not numerous enough nor big enough to bring Z_B to positive values.

The different colors of the lines in fig. 3.12 indicate 3 different snapshots at which each simulation was analyzed ($t=500\text{c.u.}, 600\text{c.u.}$ and 700c.u.). For both sub-Alfvénic and super-Alfvénic sets, as time goes by, the density variations are only caused by compression and rarefaction due to turbulent motions. Z_B values do not change much along time, but they do change with different \mathcal{M}_A and \mathcal{M}_s values. For $\mathcal{M}_A = 0.7$, stronger magnetic fields become dynamically more important and force the motion of the turbulent flow along the magnetic field lines, thus increasing the values of Z_B at higher densities, specially as the sonic Mach number increases causing the formation of smaller denser structures. This does not occur at same degree in the super-Alfvénic case.

While the density distribution shows only a change in the values of Z_B as the Alfvénic Mach number changes (Figure 3.12), for the column density along a given LOS, this behaviour is realized only partially in Z_E (in Figures 3.8 and 3.10). To see how much the LOS direction influences the observations, we have considered the three LOS discussed in Figures 3.8 to 3.11 for all models with no self-gravity. These models and all the information gathered from the analyses above will be useful to discuss the influence of magnetic fields in observed systems, which we perform in Chapter 4.

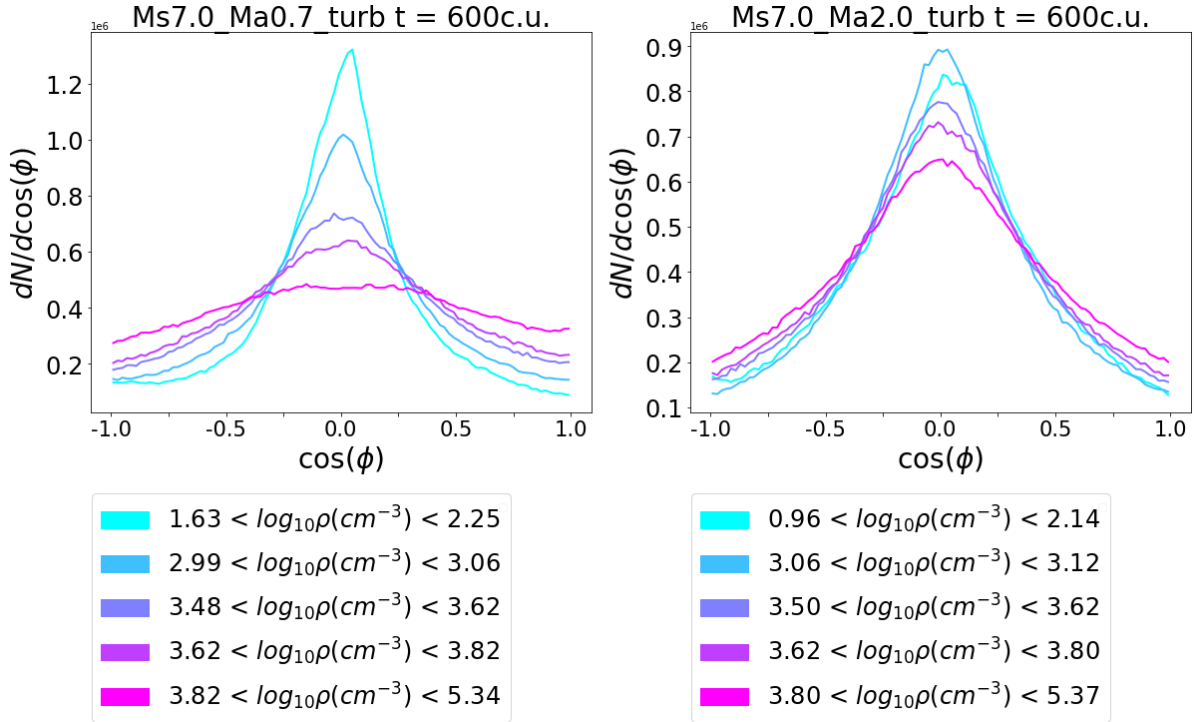


Figure 3.13: Histograms of $\cos(\phi)$ (eq. 2.15, section 2.2) for different bins of density for the sub-Alfvénic (left) and super-Alfvénic (right) models without self-gravity. Only bins 1st, 10th, 17th, 18th, 19th and 20th are shown.

In the next section, the influence of self-gravity in the systems and its interaction with both, magnetic fields and turbulence will be discussed.

3.3 Simulations with self-gravity

The simulations presented in this section have initial conditions similar to models shown before. The detailed initial conditions are described in table 2.1. As remarked before (Chapter 2), this set of simulations was made using a modified version of the code described in Kowal et al. (2007); Santos-Lima et al. (2012); Leão et al. (2013).

While in models with no self-gravity the turbulent motion is the main agent modifying the magnetic field distribution, particularly in the supersonic regime investigated here, now gravitational forces will also become important when overdense regions start to grow and become gravitationally unstable. In accordance to previous studies (André et al. (2010); Hennebelle and Falgarone (2012); André et al. (2014)), these overdense regions are usually located along filaments. Matter can flow along these structures and also influenced by the presence of magnetic field.

To evaluate how filaments evolve in the presence of self-gravity, we will once again use the PRS analysis. Figure 3.14 shows the calculated values of Z_B for all models. As time passes and self-gravitating regions grow, the gradient of the density becomes less perpendicular to the magnetic field at denser regions (i.e., \mathbf{B} tends to become more perpendicular to these collapsing regions). This result is similar to what was seen in the previous section (Figure 3.12) when no self-gravity was present. The addition is that, higher densities are achieved as time passes. As the fluid streams more easily along the magnetic field lines (since in the normal direction magnetic pressure gradients will inhibit the motion and provide support against gravity), dense structures will accumulate by gravity action mainly perpendicularly to the field direction. This can happen for both, the sub and super-Alfvénic cases, since at smaller scales magnetic fields become more and more important, as they are brought along with the collapsing regions, but is more pronounced in the sub-Alfvénic cases.

The slope of the curves presented in Figure 3.14 also behaves in a similar way as in Figure 3.12, changing for different \mathcal{M}_s in the sub-Alfvénic case, while in the super-Alfvénic case, the slope does not change much. Once again, no positive values of Z_B are seen, but the change of the slope as time passes indicates that regions where $\nabla\rho$ is parallel to \mathbf{B} at higher densities become more important at later times. This is of course, due to the action of gravity creating collapsed regions to where the flow of matter converges. Compared to the models with no self-gravity where filaments are formed by compression forces only, in the models with self-gravity we see that lower density regions are still dominated by the interplay between turbulent motions and the magnetic field while higher density regions become dominated by an interplay between the action of gravity and magnetic fields.

Similarly to Figure 3.13, Figure 3.15 shows the HRO curves for two self-gravitating models, *Ms7.0-Ma0.6_grav* and *Ms7.0-Ma2.0_grav*. This was evaluated over the last output of these models, when $t = 0.3t_{ff}$ (see the right side of Figure 3.4 which shows the filamentary 3D distributions for these models). Compared to the models that do not include self-gravity, there is an enhancement in the number of regions perpendicular to the magnetic field at higher densities. With the action of gravity, even the super-Alfvénic model shows a change in the number of counts of $\cos\phi = \pm 1.0$. Z_B is still negative to all values of density, but the influence of gravity interacting with denser regions is clear.

The critical density (vertical green dashed line in Figure 3.14) seems to be related to

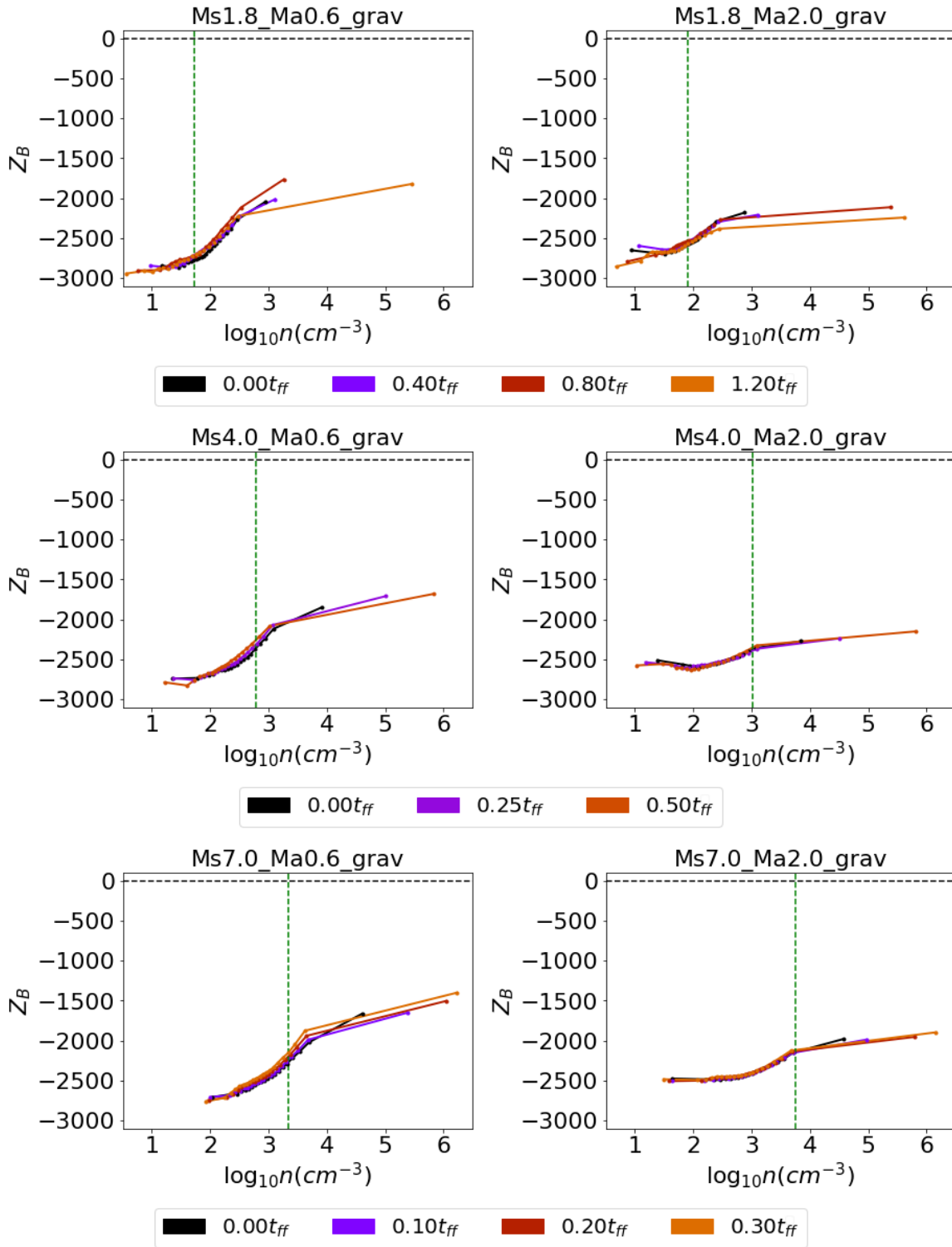


Figure 3.14: Z_B analysis (equation 2.21) applied to the 3D distribution of density and magnetic fields for all simulated models with self-gravity (see table 2.1). On the left are presented the sub-Alfvénic (initial $M_A = 0.6$) and on the right, super-Alfvénic (initial $M_A = 2.0$) models. From top to bottom initial $M_s = 2.0, 4.0$ and 7.0 , respectively. The green dashed line indicates the critical density for star-formation (eq. 2.14).

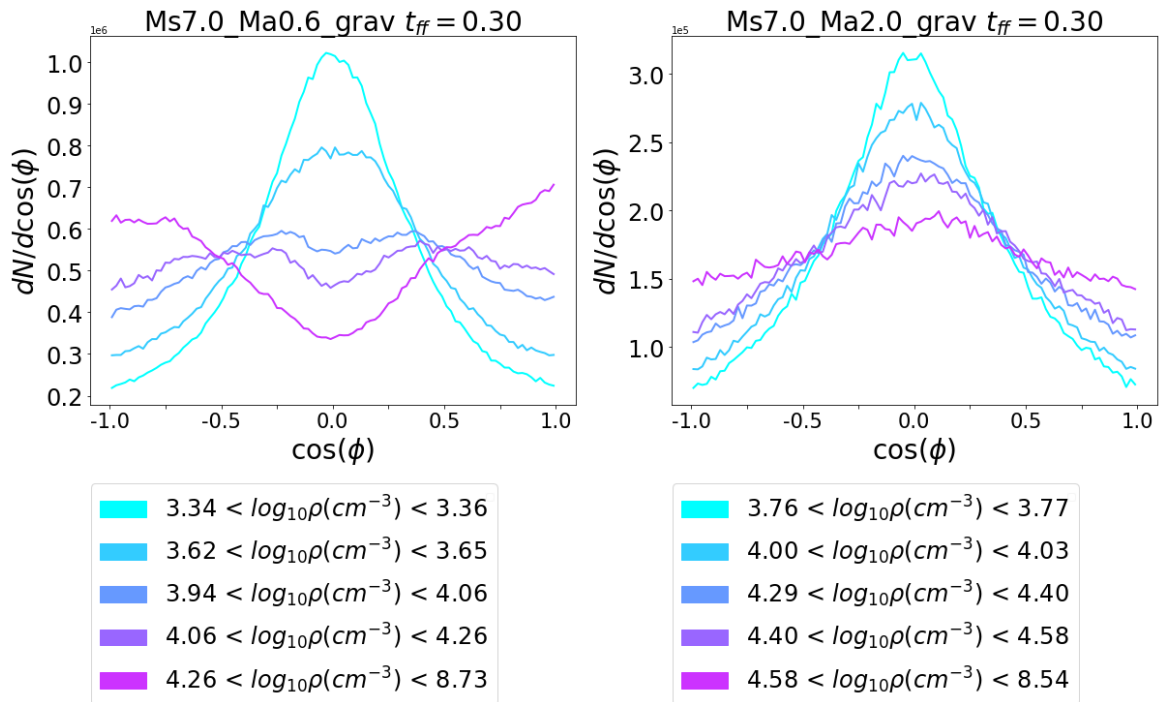


Figure 3.15: Histograms of $\cos(\phi)$ (eq. 2.15, see section 2.2) for different bins of density for the sub-Alfvénic (initial $\mathcal{M}_A = 0.6$, left) and super-Alfvénic (initial $\mathcal{M}_A = 2.0$, right) models with self-gravity. Only bins 1st, 10th, 17th, 18th, 19th and 20th are shown.

the densest bins, for models with sonic Mach numbers $\mathcal{M}_s = 4.0$ and 7.0 . There is a “jump” in the values of density between the penultimate and last points in the diagrams that comes from the density range considered in the bins (as can be seen in Figure 3.15, the 20th bin has a wider range of densities compared to the 19th). While the last point is related to densities that are part of the power-law tail of the PDF, the penultimate point is near the transition between the lognormal and power-law. In the super-Alfvénic case, the penultimate point is very close to ρ_c for all times considered, while in the sub-Alfvénic the penultimate point approaches ρ_c as the system evolves.

Tracing the critical density of a system using the PRS is an interesting possibility, and the exact relation between the two can be further explored following the evolution of the alignment between structures and the magnetic field at smaller scales and at latter times of the collapse. However due to the lack of an adaptive mesh with increasing resolution in densest regions in our models, this is out of the scope of this work.

Still, the results discussed up to this point are very similar to what was shown in the previous section for models without self-gravity. We note that self-gravity does increase the number of denser regions where \mathbf{B} is parallel to the gradient of density in the sub-Alfvénic

models, but it has little or no effect when it comes to the simulations with $\mathcal{M}_A = 2.0$. At smaller scales this is probably not true, since we expect that magnetic fields should be brought along with the fluid during collapse, at some point these cores must become sub-Alfvénic and once again \mathbf{B} would influence how the gas collapses. However, the simulations do not have enough resolution to follow the process up to this point.

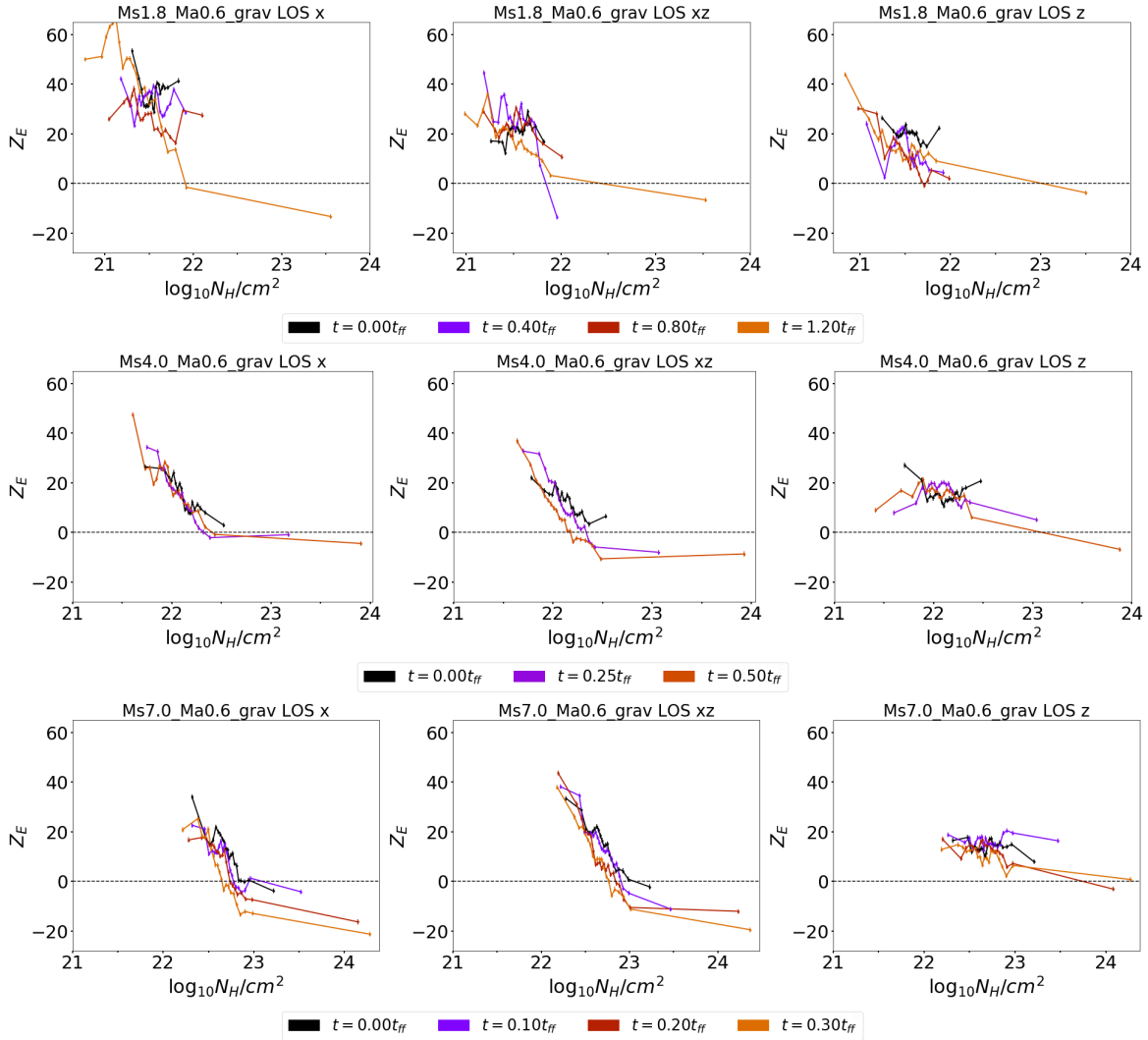


Figure 3.16: PRS time evolution for all sub-Alfvénic (with $\mathcal{M}_A = 0.6$) models with self-gravity. From left to right the PRS is applied along Z (the direction perpendicular to the initial field), XZ (45° with regard to the initial field) and X (perpendicular to the initial field) directions. From top to bottom initial $\mathcal{M}_s = 2.0, 4.0$ and 7.0 , respectively.

In order to compare these simulations with observations we need to once again integrate along a defined LOS. We will follow same directions used in section 3.2, just note that for this set of simulations, the initial magnetic field was initially parallel to the Z axis and not the X axis. Figures 3.16 and 3.18 show the PRS analysis (Z_E) for the integrated density

(column density) distribution along the three different LOS. As in Figures 3.8 (for initial $\mathcal{M}_A = 0.7$) and 3.10 (for initial $\mathcal{M}_A = 2.0$), the first column represents the LOS parallel to the initial magnetic field, the middle column shows Z_E for a LOS making an angle of 45° with regard to the initial field, and the right column, is for a LOS perpendicular to the initial magnetic field. From top to bottom, each line has, respectively, $\mathcal{M}_s \sim 1.8, 4.0$ and 7.0 .

As we have seen before, the fragmentation and collapse of the structures in the cloud depends on the sonic Mach number, the higher, the faster the collapsing very dense regions appear, and the PDF of density reaches a power-law tail with a slope $\alpha = 1.5$ (see section 3.1). First, in the sub-Alfvénic cases (Figure 3.16), the initial distribution of Z_E (black curve) is similar to the simulations without self-gravity. However, as the densest regions collapse, the effect seen in Z_B (Figure 3.14) is more pronounced for Z_E .

From the sub-Alfvénic models that do not consider self-gravity (see Figure 3.8) we saw that for higher sonic Mach numbers, and when the LOS is not parallel to initial magnetic field, Z_E decreases as the density increases. That is exactly what is seen in the models from Figure 3.16 when $t = 0.0 t_{ff}$. However, with gravity acting over the system all models evolve to a similar distribution of Z_E , with lower densities having positive (\mathbf{B} aligned with the filaments) values and higher densities showing negative values (\mathbf{B} perpendicular to the filaments). This turns out to be the case even when the LOS is parallel to initial field (where we see less of the original magnetic field orientation and more of the random component, see the first column of Figure 3.16). In particular, for $\mathcal{M}_s = 1.8$, this trend is not initially present, but the action of gravity results in negative values of Z_E at later times for all LOS. In summary, self-gravity does affect the Z_E distribution of dense regions of sub-Alfvénic models more clearly than in models with no gravity, as we should expect, and may help to distinguish between different observed IS regions (see Chapter 4).

With the LIC method applied to the projected magnetic field to the sky (\mathbf{B}_\perp), Figure 3.17 shows the column density maps at the latest time considered in each simulation (when $\alpha_{powerlaw} = 1.5$), for the sub-Alfvénic models ($\mathcal{M}_A = 0.6$) with self-gravity. The magnetic field is coherent over a large distance when the integration is made along the inclined LOS (45°) or perpendicular to the initial field. As the system is sub-Alfvénic, very dense structures should form mostly perpendicular to the magnetic field even in highly supersonic turbulence, however this can only be realized in the integrated maps if

the LOS is not aligned to the initial field (X and XZ LOS in the figure). Once self-gravity becomes important the collapse of structures naturally occurs along the magnetic field lines, which means that negative values of Z_E appear at higher densities for all LOS (as we have seen in Figure 3.16). From the LIC maps in Figure 3.17, it is easy to see dense structures perpendicular to \mathbf{B}_\perp for the LOS X and XZ , but not so much for Z . Still these regions are present, as was highlighted in Figure 3.16.

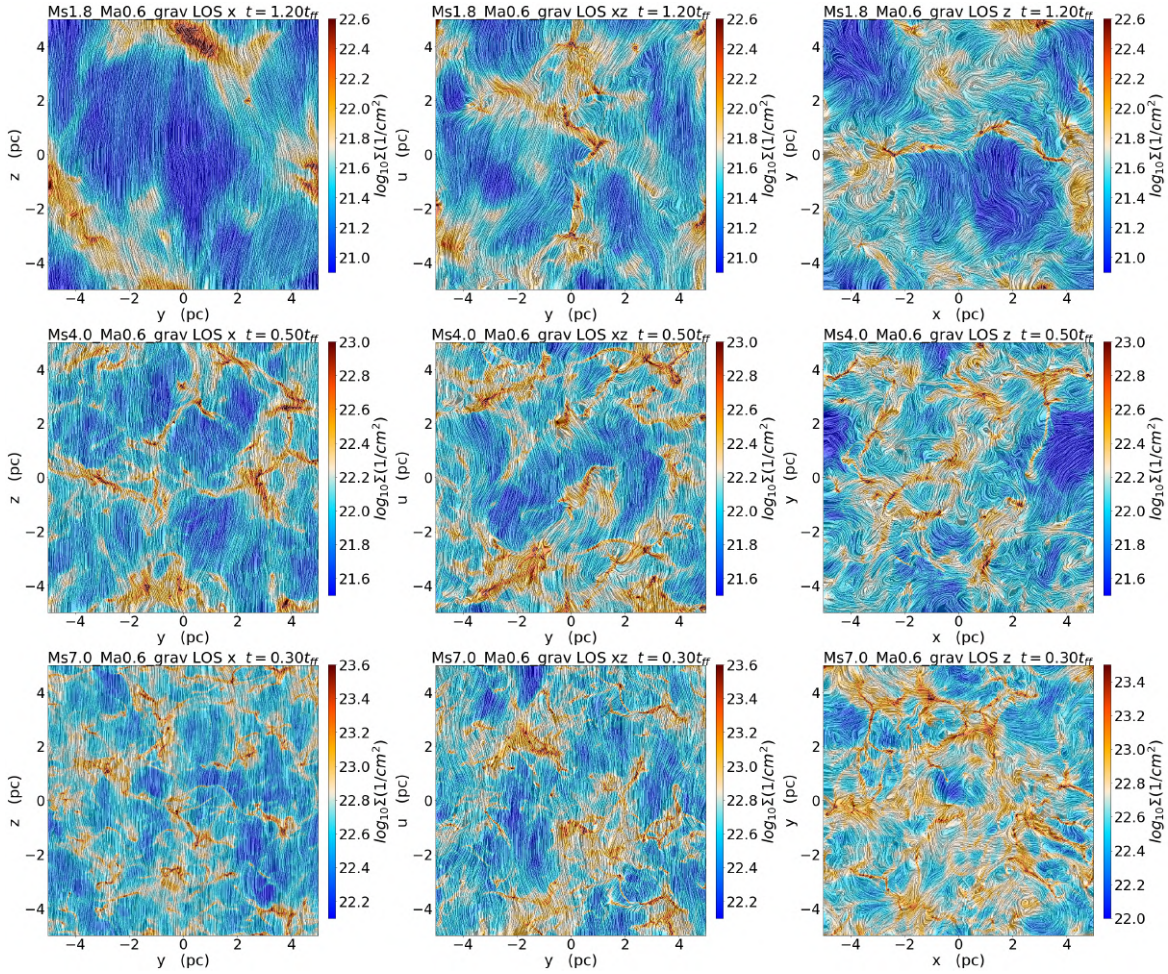


Figure 3.17: Column density maps with LIC method applied to \mathbf{B}_\perp for the same sub-Alfvénic models with self-gravity presented in Figure 3.16. The time considered for each map is indicated above each diagram. From left to right the integration is along X (the direction perpendicular to the initial field), XZ (45° with regard to the initial field) and Z (perpendicular to the initial field) defined directions. From top to bottom initial $\mathcal{M}_s = 1.8, 4.0$ and 7.0 , respectively.

For the super-Alfvénic case ($\mathcal{M}_A = 2.0$; see Figure 3.18) the scenario is different, the polarization vector \mathbf{E} appears mainly aligned to the column density gradient ∇N_H (i.e. $Z_E > 0$ always, eq. 2.21), which means that the projected magnetic field is more frequently

parallel to the structures. This is similar to the no-gravity super-Alfvénic models (Figure 3.11), but in Figure 3.18 larger column densities and Z_E values are achieved. Smaller values of Z_E at higher densities also appear for $\mathcal{M}_s = 7.0$ at later times, but for sonic Mach numbers 1.8 and 4.0 higher values of Z_E are seen at these densities, indicating that denser structures are still aligned to the projected field to the sky.

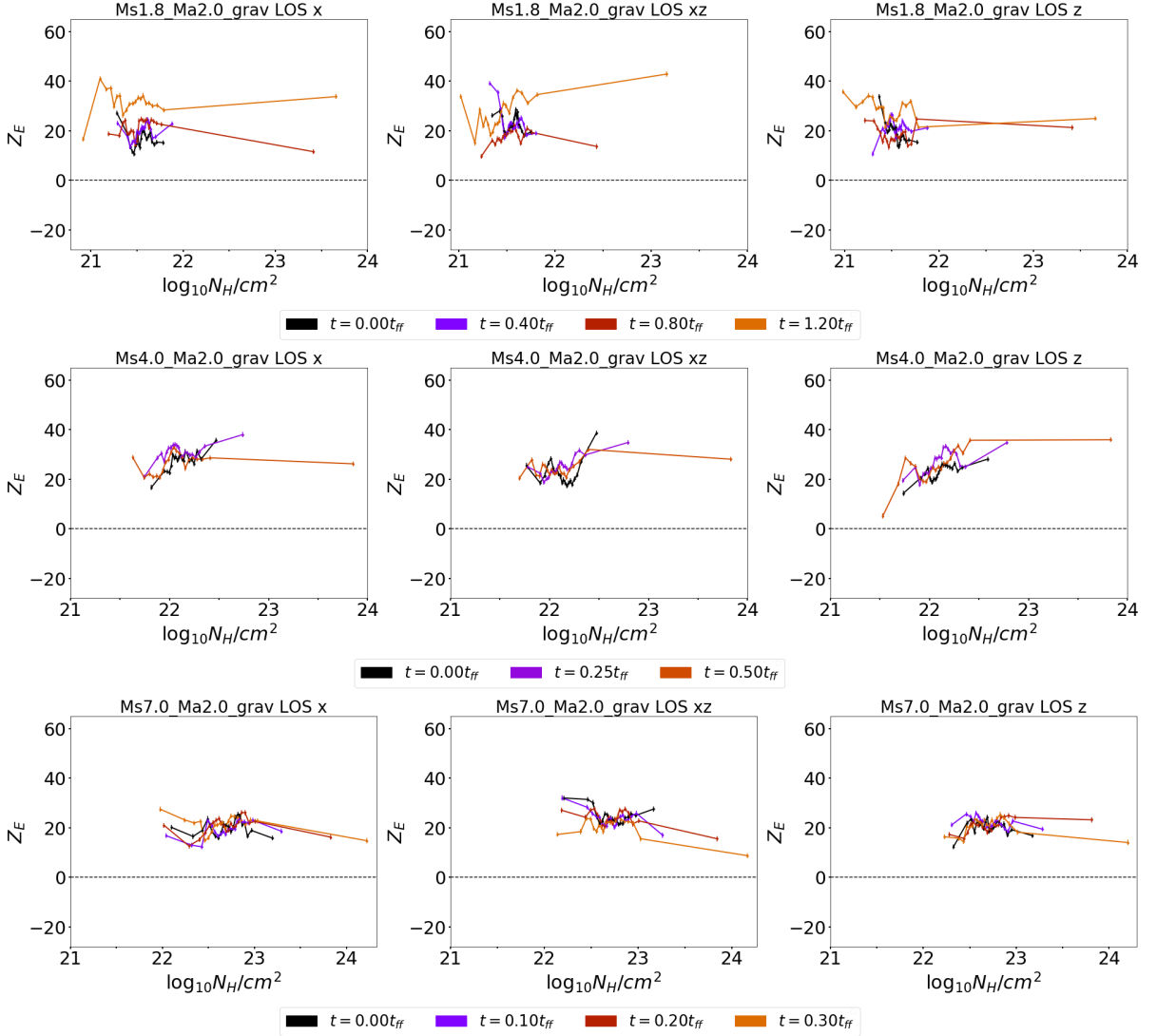


Figure 3.18: PRS time evolution for all super-Alfvénic (with $\mathcal{M}_A = 2.0$) models with self-gravity. From left to right the PRS is applied along Z (the direction perpendicular to the initial field), XZ (45° with regard to the initial field) and X (perpendicular to the initial field) directions. From top to bottom initial $\mathcal{M}_s = 2.0, 4.0$ and 7.0 , respectively.

With lower sonic Mach numbers, less fragmentation occurs. While the compression of the gas can bring together field lines along the filaments, the *voids* (dark blue regions in Figure 3.19) are left with a coherent \mathbf{B}_\perp . When we consider a higher sonic Mach number

this effect is still present, but with the larger fragmentation, inside the filaments there are several cores at later times. The field is still mainly aligned to the filament, but due to the action of gravity, in the several collapsing cores, where locally the system can become sub-Alfvénic, there are regions where the gradient of density is parallel to the field lines.

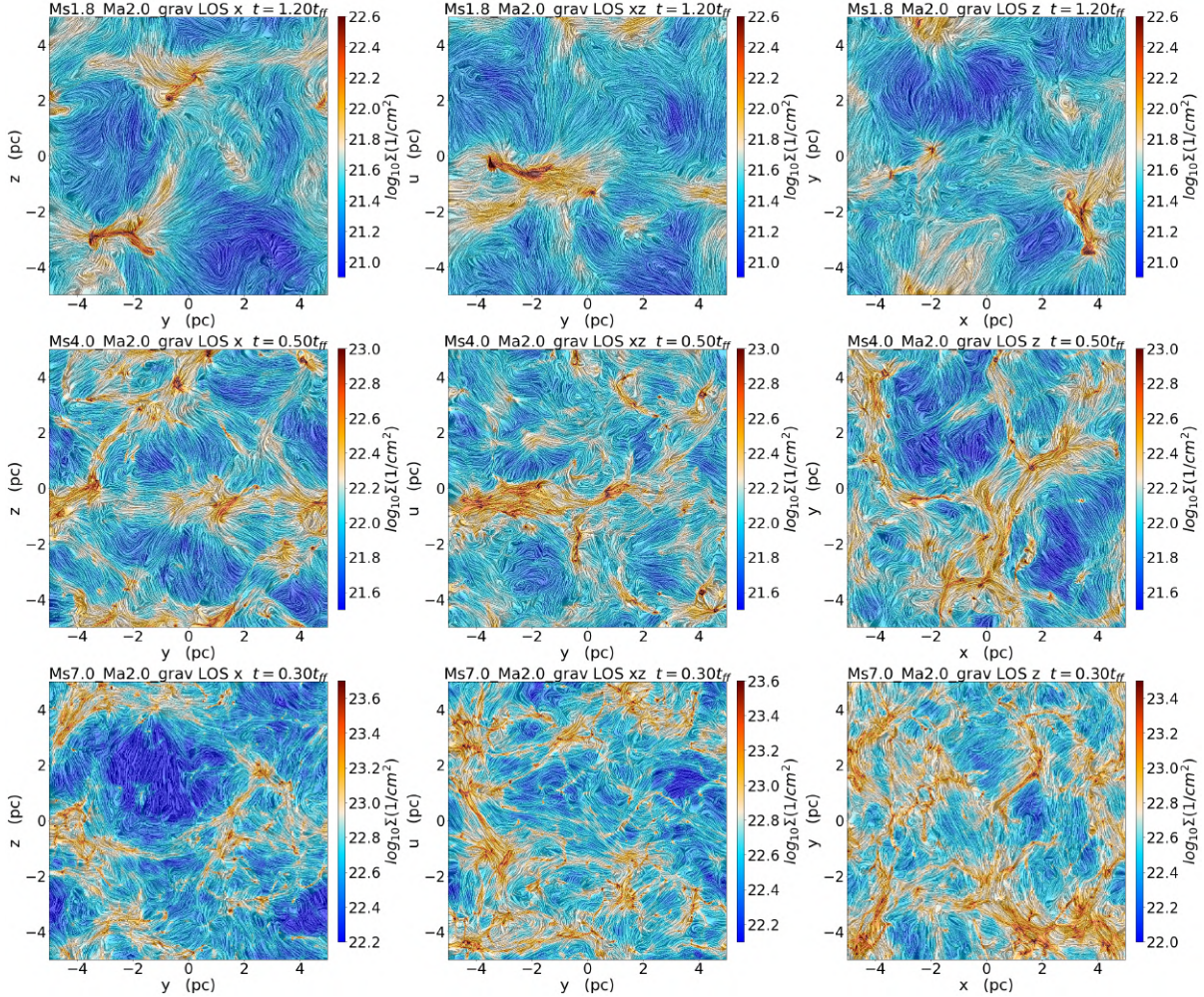


Figure 3.19: Column density maps with LIC method applied to \mathbf{B}_\perp for the same super-Alfvénic models with self-gravity presented in Figure 3.18. The time considered for each map is indicated above each diagram. From left to right the integration is along X (the direction perpendicular to the initial field), XZ (45° with regard to the initial field) and Z (perpendicular to the initial field) defined directions. From top to bottom initial $M_s = 1.8, 4.0$ and 7.0, respectively.

3.3.1 Turbulence, gravity and magnetic field interlinks

From what has been shown, the mere presence of the magnetic field creates an anisotropy inside the cloud. Naturally, compression induced by the supersonic turbulent

motions will bring magnetic field lines together, which in turn can make the motion locally sub-Alfvénic. Figures 3.12 and 3.14 show that Z_B steadily grows for all cases, which is an indication of this characteristic of MHD systems.

To better understand how gravity affects different density intervals, in Figure 3.20 we present again the histograms of $\cos(\phi)$ distribution (HRO) for sub-Alfvénic and super-Alfvénic models, with the same sonic Mach number ($\mathcal{M}_s = 7.0$). On the left, we have these models in the initial state at which only turbulence is present ($t = 0.0t_{ff}$). This snapshot is also representative of what is commonly seen in the simulations that do not consider self-gravity (and is similar to Figure 3.13). On the right, it is presented the final step for the same models, when self-gravity is operating and several regions have collapsed. Only regions with densities higher than ρ_c , as defined in equation 2.14, have been considered (these diagrams are the same as in Figure 3.15). In Figure 3.21 the green lines are the PDFs of the models in the aforementioned figure.

In all diagrams of Figure 3.20, lower density regions (bright blue color) have a peak around $\cos(\phi) = 0$, indicating \mathbf{B} is mostly aligned with the filaments due to compression. At higher densities, we have a more interesting scenario, showing how much these regions are affected by gravity, as discussed before. While Z_B shows only a variation, but is still negative across all density range (see Figures 3.12 and 3.14), the histograms of Figure 3.20 reveal a clearer role of gravity.

In the sub-Alfvénic case ($\mathcal{M}_A = 0.6$), when only turbulence is present the distribution of $\cos(\phi)$ is almost flat at higher densities, but once these regions collapse the number of cells where $\cos(\phi) = 0$ (i.e. \mathbf{B} parallel to the filaments) reduces immensely. Each of the curves in Figure 3.20 represents one density bin. Since we are considering 21 bins, the effects only become really important in the last three or four bins. In Figure 3.20 only bins 1st, 13th, 19th, 20th and 21st are shown.

In the super-Alfvénic case ($\mathcal{M}_A = 2.0$), without gravity, there is very little trace of regions where the magnetic field lines are parallel to the gradient of density (i.e., normal to the filamentary structures). This is, of course, only possible to be seen in highly super-sonic systems, as indicated by Z_B diagram previously (Figure 3.14).

To complete our analysis, Figure 3.21 shows the PDF of the densities for all models investigated, for two snapshots, the same initial one (when turbulence has fully developed to steady state just before self-gravity is turned on, $t = 0.0t_{ff}$) and the final snapshot

(which is different for each model). Figure 3.21 also indicates, with vertical dashed lines, the critical density at which each model will form stars (eq.2.14).

A comparison of this figure with Figure 3.14 for the super-Alfvénic model, shows that the highest density regions with \mathbf{B} normal to the filaments are all in the power-law tail, which also indicates that gravity is the responsible for creating this kind of alignment. Even though the system starts with a homogeneous magnetic field along Z direction, it does not take too long before the initial coherence of the field is lost. While in the sub-Alfvénic case, turbulence pushed by magnetic pressure gradients can be enough to create structures perpendicular to the field, with $\mathcal{M}_A = 2.0$ the HRO analysis shows this sort of distribution cannot be achieved without the help of gravity, as previously remarked.

The projection (and integration) of structures along a given LOS can also provide hints about the relation between gravity and magnetic fields, even though the relation with what is seen in the three dimensional distribution of density is not straightforward.

The integration along the LOS has an effect of “averaging ” what is happening inside the volume of the system. For example, even for lower sonic Mach numbers ($\mathcal{M}_s = 1.8$), if the LOS is parallel to the initial magnetic field, most \mathbf{B}_\perp appears parallel to the iso-contours of the column density, when self-gravity is not important. The first column of Figure 3.8 shows this behaviour, as all PRS’s are close to a flat distribution. This is clearly not the case when self-gravity is considered, since this force will dominate the system at higher densities and, combined with the magnetic pressure forces, will make the gas to flow mostly along the lines. From the left column of Figure 3.16, in sub-Alfvénic models ($\mathcal{M}_A = 0.6$) at later times, negative values of Z_e are present for all sonic Mach numbers used, as a reflection of this property.

The projection along different lines of sight does not show any particularity when $\mathcal{M}_A = 2.0$. Varying the sonic Mach number does seem to produce a substantial change in Z_e . While for $\mathcal{M}_s = 7.0$ the behaviour at later times is similar to the sub-Alfvénic case, for lower sonic Mach numbers show Z_e has opposite behaviour. Figure 3.19 shows a lot of filaments and overdense regions inside those filaments when $\mathcal{M}_s = 7.0$ produce negative values of Z_e , i.e. have the projected magnetic field to the sky \mathbf{B}_\perp , perpendicular to the structure, as concluded before). This property is also present in models with lower sonic Mach number, but the fragmentation of the cloud is smaller in these cases. This means that the number of filaments and cores is smaller and the statistics of less dense regions

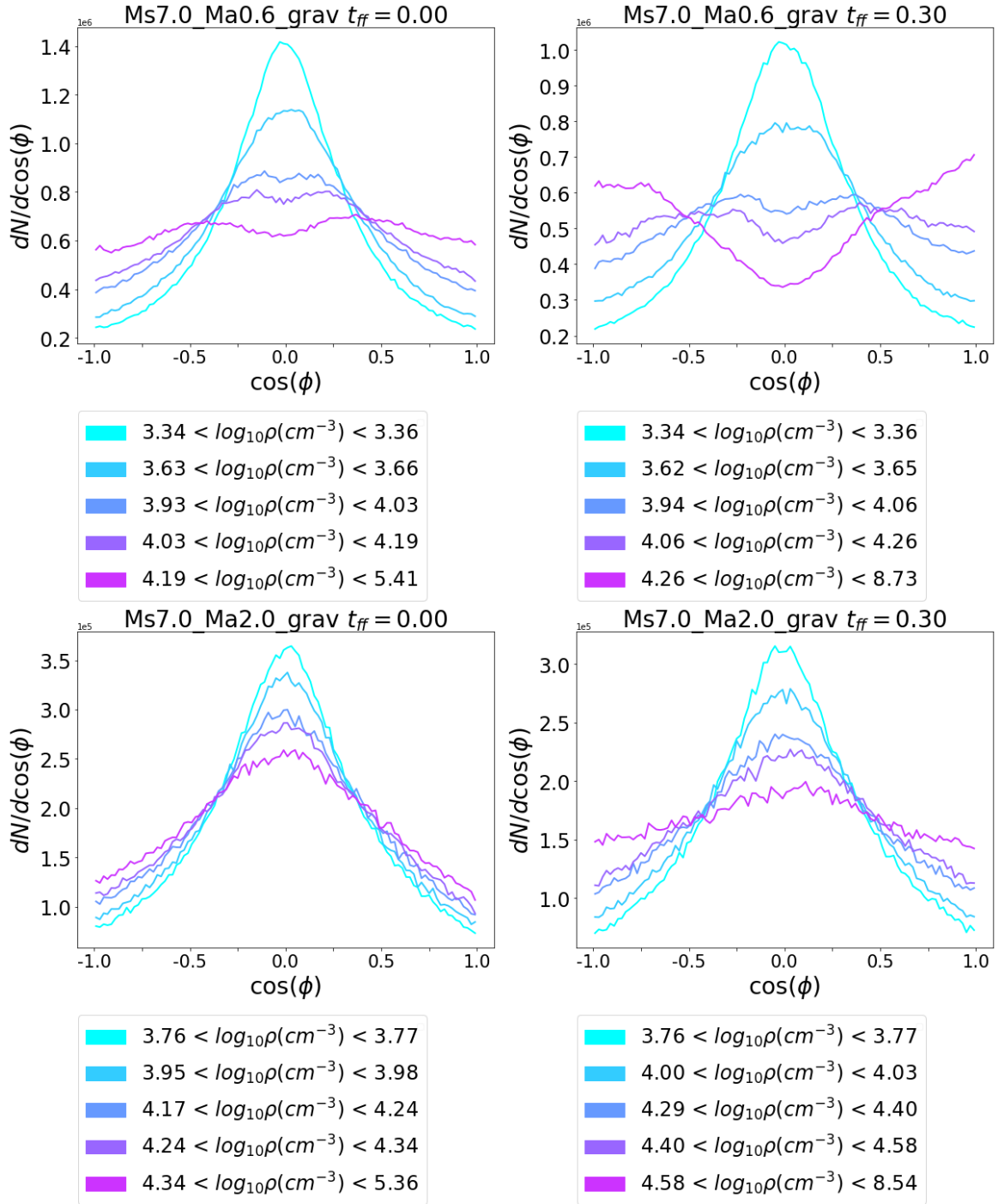


Figure 3.20: Histograms of $\cos(\phi)$ (eq. 2.15, see section 2.2) for different bins of density for the sub-Alfvénic (initial $\mathcal{M}_A = 0.6$, top) and super-Alfvénic (initial $\mathcal{M}_A = 2.0$, down) models with self-gravity. The initial time $t = 0.0t_{ff}$ is presented on the left, and the final state $t = 0.3t_{ff}$ on the right side. Only bins 1st, 10th, 17th, 18th, 19th and 20th are shown.

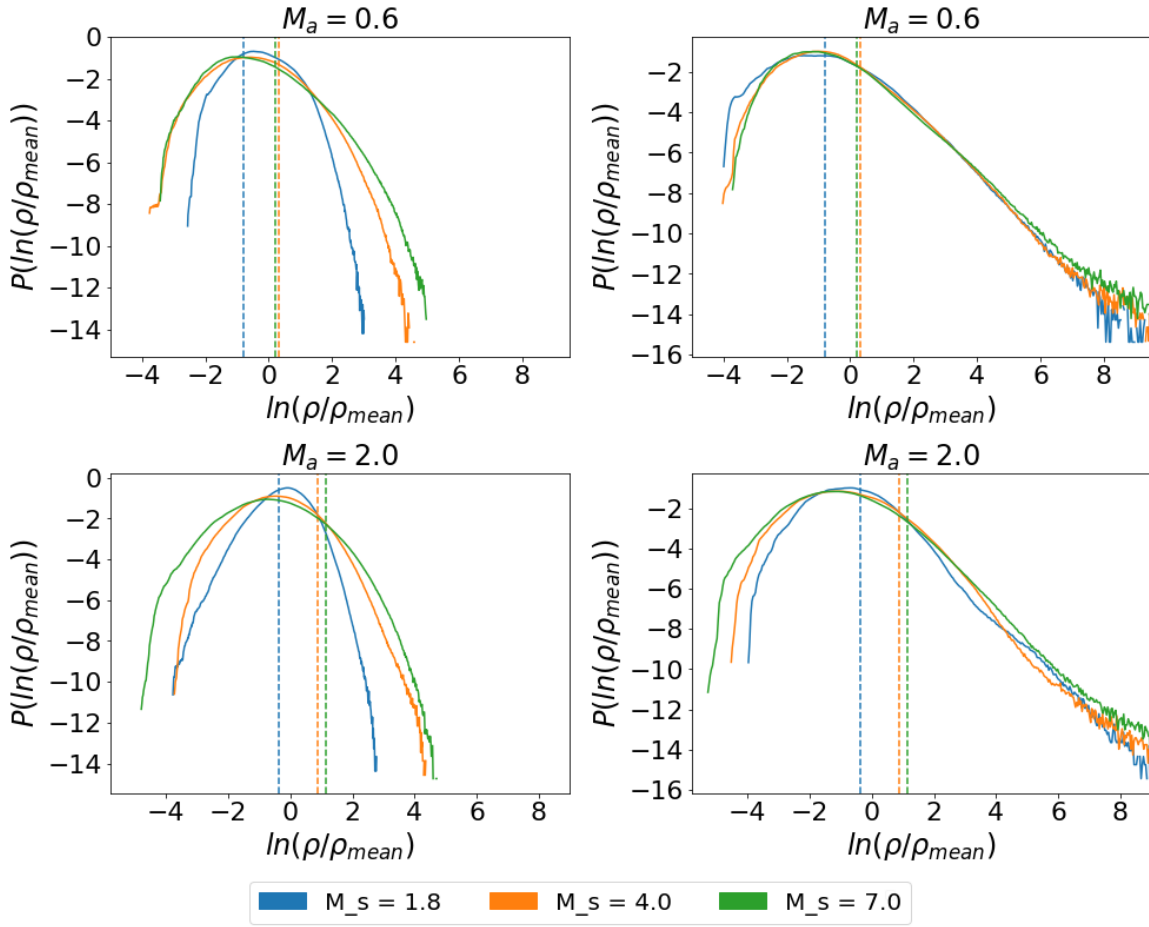


Figure 3.21: Density PDF's of all models with self-gravity. The top diagrams show the sub-Alfvénic and the bottom ones, the super-Alfvénic models. On the left, $t = 0.0t_{ff}$ is shown. On the right, $t = 1.2t_{ff}$, $0.4t_{ff}$ and $0.3t_{ff}$ is considered for $\mathcal{M}_s = 1.8, 4.0$ and 7.0 , respectively. The dashed vertical lines are the critical density for star formation according to equation 2.14 for each of the models.

prevails over the PRS.

3.4 Summary of the results

We can summarize our findings as follows:

1. Considering the results from the analysis of the integrated density (column density) maps along different LOS of the models that do not consider self-gravity (section 3.2) we have found that:
 - For sub-Alfvénic models, the magnetic field introduces an anisotropy in the system, and the direction of the LOS with regard to the initial magnetic field is

important. First, this affects the general morphology and coherence of the field projected on the sky. When the LOS is parallel to initial field, only perpendicular random components to the intrinsic field are seen. When the LOS is not parallel, the main component of the intrinsic field appears as more coherent projected coherent field across large length scales. The LOS in these cases also changes the PRS distribution (Z_E ; equation 2.21), and this is also affected by the sonic Mach number. For smaller sonic Mach numbers ($\mathcal{M}_s \sim 2.0$) most of the polarization vector \mathbf{E} appears parallel to the gradient of column density (∇N_H), $Z_E > 0$ in all models, that is, the magnetic fields are mainly aligned to the filaments, due to action of supersonic turbulent compression motions. For larger sonic numbers, the fragmentation increases and smaller values of Z_E can be seen for denser regions (specially if the LOS is not parallel to the initial magnetic field). This indicates that these denser smaller regions have a greater contribution of structures perpendicular to \mathbf{B}_\perp , due to the dominance of the magnetic forces that prevent gas motion across the lines, facilitating their flow along them.

- For super-Alfvénic models, the less intense magnetic field does not show the same kind of coherence along large length scales, since the lines are more easily twisted by the turbulent motions, and the column density maps show similar characteristics at different LOS. The PRS analysis also reflects this, with Z_E presenting only positive values (often ranging between $\sim 5 - 20$) for all LOS. Different sonic Mach numbers also show no clear effect in the alignment of the structures with the field.

2. Considering the results of the analysis of the column density maps along different LOS for the models that include self-gravity (section 3.3) we have found that:

- With the presence of self-gravity there is an enhancement of dense structures perpendicular to the projected magnetic field to the sky. When the system is sub-Alfvénic, smaller values of Z_E are present for all LOS at higher column density values. At later times, all models show at some degree a change from positive to negative values in Z_E which implies the presence of dense collapsing structures with magnetic fields normal to them, as one should expect, since the

collapse is easier along the magnetic fields.

- For the super-Alfvénic models, as in the case with no gravity, Z_E is positive for all LOS indicating that most structures are aligned with the projected magnetic field to the sky. This effect is less prominent for $\mathcal{M}_s = 7.0$, where more fragmentation again propitiates the formation of denser collapsed cores inside filaments, and since magnetic fields are aligned to them, these cores appear as perpendicular structures to the field and therefore yield lower values of Z_E .

3. With regard to the 3D analysis of the density structures, we have found that:

- For the sub-Alfvénic models, turbulence alone can create perpendicular filaments to magnetic field, since the strong field is resistant to compressions perpendicular to its direction, leading the supersonic turbulence to compresses the gas in directions parallel to the field. The inclusion of gravity helps the creation of structures perpendicular to the field, and less dense filaments parallel to it (see Figure 3.4). This is more easily realised through the histograms of $\cos(\phi)$ (left diagram of Figures 3.13 and 3.15), with $\cos(\phi) = \pm 1$ having a higher number of counts for the bin of largest density. In accordance to what is observed in the column density maps for Z_E (Figures 3.9 and 3.17), the PRS analysis of the density shows higher values of Z_B with higher sonic Mach numbers, specially at higher densities.²
- For the super-Alfvénic models, magnetic field lines appear mostly aligned to filaments when only turbulence is considered, with the sonic Mach having little or no effect. However, models that consider gravity have a change in the behaviour of dense regions, with structures appearing perpendicular to the magnetic field at later times.

Finally, taking into consideration what has been shown in this Chapter, we can conclude that self-gravity gravity can create several structures perpendicular to the magnetic field, regardless of the mean Alfvénic mach number of the cloud. As evidenced by the PDF and power spectrum, the smaller scales of the clouds are clearly being dominated by gravity,

² Note that positive values of Z_E should be reflected as negative values of Z_B , and vice-versa (see Section 2.2.1).

while less dense regions are mainly affected by turbulence, as lower densities still sit in the lognormal branch of the PDF (see Figure 3.21). Effects of projection due to the LOS may change the observed alignment for less dense regions, but still overdense regions show smaller values of Z_E .

In the next chapter, we will use these models to compare with observations made by *Planck Satellite*, *Herschel* and *BLASTPol*.

Comparison of the models with Observations

4.1 Introduction

To compare the results of the simulated models presented in the previous chapter with observations, we will use as main sources, the clouds observed by *Planck Satellite* (Planck Collaboration et al. (2016)) and BLASTPol (Soler et al. (2017)). These results have been revised by Jow et al. (2018), which serves as direct comparison to our results.

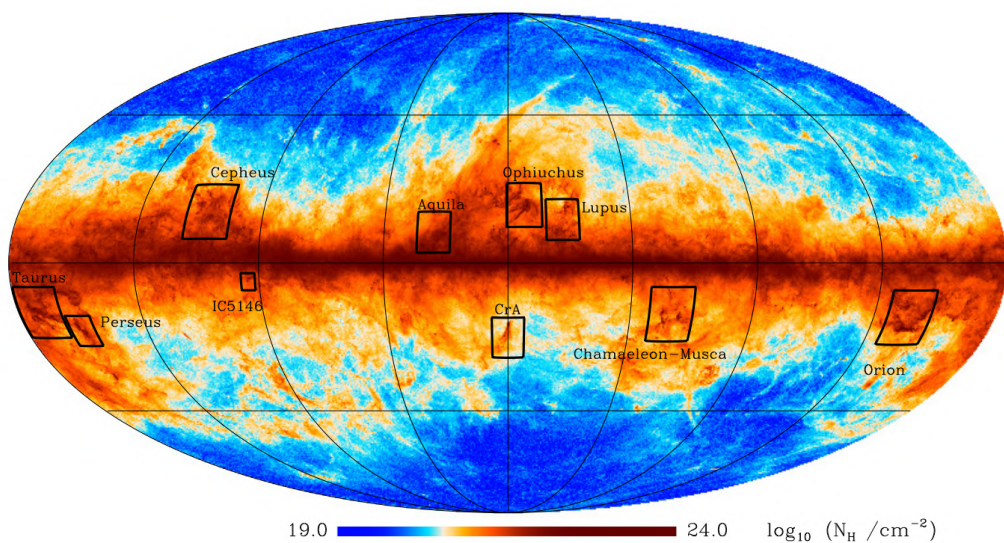


Figure 4.1: Column density map of the entire sky observed by *Planck* at 353 GHz. Black squares indicate the location of the molecular clouds observed. Extracted from Planck Collaboration et al. (2016).

Planck Satellite observed thermal emission and dust polarization in 7 bands between 30 and 353 GHz. In the case of Planck Collaboration et al. (2016), the observations were made using the High Frequency Instrument at 353 GHz. The molecular clouds reported have distances estimated between ~ 150 pc and ~ 450 pc. Given their angular sizes of

about $15^\circ \times 15^\circ$, these distances imply that the clouds have sizes up to ~ 100 pc. The sonic Mach number estimated for these regions may vary, e.g. Polaris MC has \mathcal{M}_s varying between $\sim 3 - 7$ depending on the region inside the cloud. Orion has $\mathcal{M}_s \sim 8$ (Schneider et al. (2013)). Temperatures range between $\sim 10 - 30K$ (Kirk et al. (2013)). Our models are compatible with these values. Figure 4.1 depicts the observation of the whole sky made by *Planck Satellite* and the black squares show the location of the MCs reported in Planck Collaboration et al. (2016).

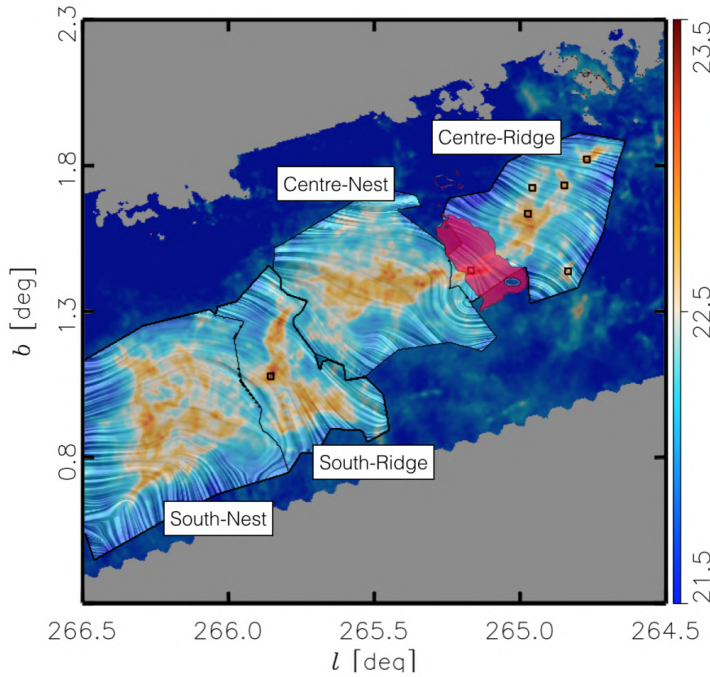


Figure 4.2: Column density map of Vela C observed by Herschel using SPIRE and PACS instruments and projected magnetic (line pattern produced using a LIC method) field derived from BLAST-Pol observations. Extracted from Soler et al. (2017).

Figure 4.2 depicts the derived column density maps and projected magnetic field onto the sky for Vela C, obtained using BLAST-Pol to estimate the magnetic field direction (Galitzki et al. (2014); Fissel et al. (2016); Gandilo et al. (2016)), and *Herschel*, to derive the column density maps (Hill et al. (2011)). BLAST-Pol used three wavelengths centered at 250, 350 and 500 μm . For the column density, *Herschel*, SPIRE and PACS data were used, with observations made at 160 (PACS), 250, 350 and 500 μm . Previous studies place the cloud around a 700 pc distance, with a total mass of more than $10^5 M_\odot$. Despite being a massive cloud, it is still at an early stage of evolution, and some authors claim that only one or two O-type stars have been formed (Soler et al. (2017) and references therein). The

estimated temperature ranges between $\sim 10 - 30K$ inside the cloud (Hill et al. (2011)).

4.2 PRS and angular distribution analysis

Jow et al. (2018) have revised the data presented in the works mentioned above in order to apply the PRS method described in section 2.2.1. Figure 4.3 shows the comparison of the PRS presented in section 3.3 with the results obtained for Vela C and a few of the clouds observed by Planck Collaboration et al. (2016).

The PRS analysis is sensitive to the number of points in the sample. This means that directly comparing the values of Z_E with the ones obtained in observations may need a little caution, this will be discussed later in this section. Nonetheless, our results can offer some insight of how the magnetic field is reflected in observations and what kind of structure distribution we can expect inside the observed MCs.

The first point that can be remarked is the general distribution of the projected magnetic field on the sky \mathbf{B}_\perp for most clouds. Although part of \mathbf{B}_\perp may appear randomly distributed on some regions of the same cloud, a main component can still be perceived, generating some coherence of the projected field inside the clouds along a single direction. Chamaleon-Musca and Aquila, for instance, are good examples of this (see Figure 4.4, left). As discussed in the previous chapter, this is a characteristic observed mainly in our sub-Alfvénic models.

From the integrated maps obtained from our supersonic, sub-Alfvénic models (Figures 3.9 and 3.17), B_\perp becomes more chaotic as the LOS gets closer to the direction of the mean magnetic field. The LOS has then the effect of regions where locally the field can appear as a random twist, while still showing a general coherence for most of the cloud. This indicates that clouds where this characteristic is present can be compared to our sub-Alfvénic models with the LOS making an angle with the local mean magnetic field.

A strike evidence in favor of a sub-Alfvénic description of the turbulence in these clouds, rather than super-Alfvénic, is the PRS analysis presented in Figure 4.3. This reveals that the observed relation between density gradients and the projected magnetic field in the sky is similar to the sub-Alfvénic models we simulated, going from positive to negative as density grows, i.e. less dense regions appear more aligned to the magnetic field, while dense regions appear more perpendicular to it. For most clouds, the turbulent models

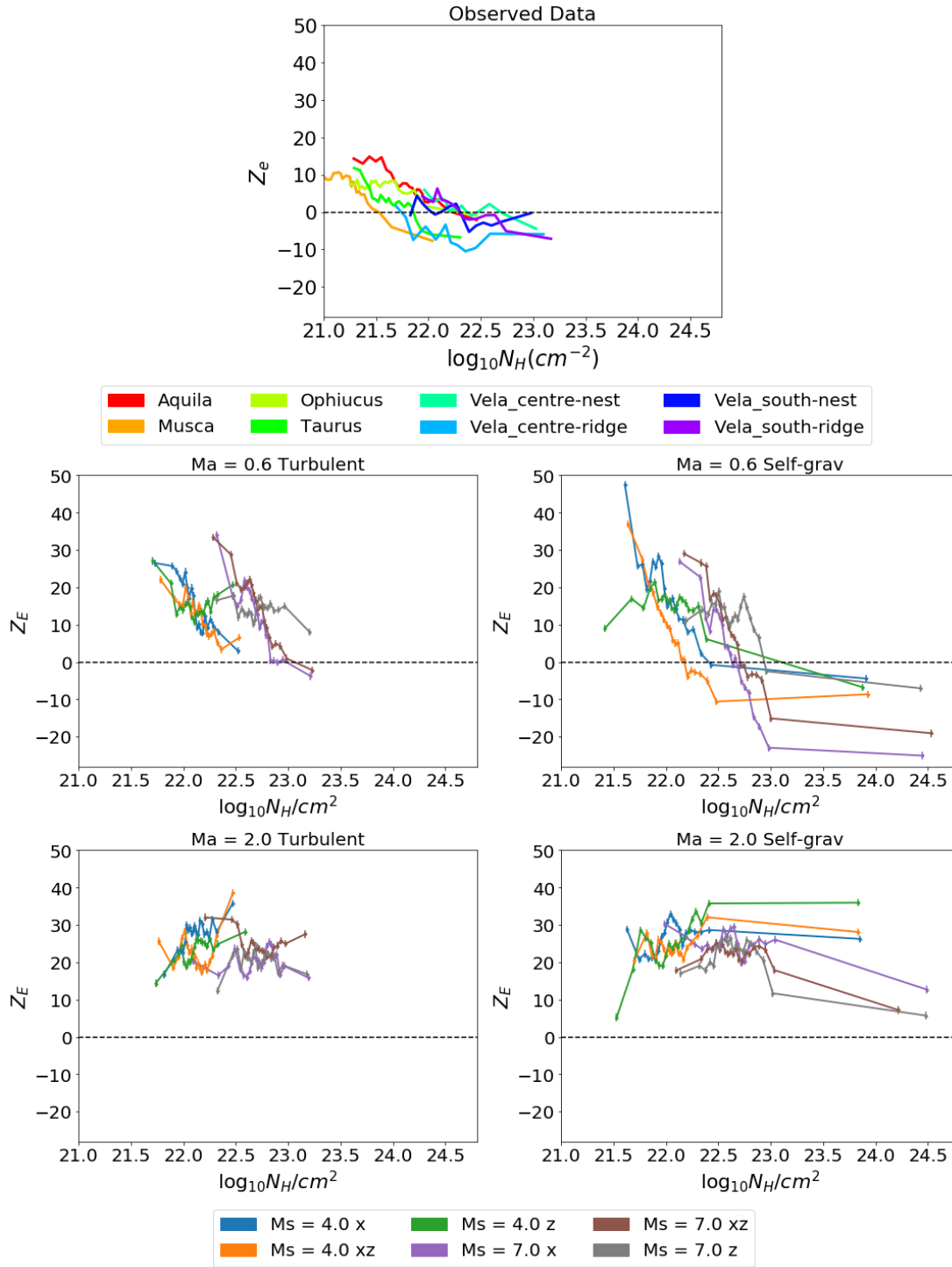


Figure 4.3: Top: Z_E (eq. 2.21) calculated from observations (Planck Collaboration et al. (2016); Soler et al. (2017)). Bottom: Z_E (eq. 2.21) calculated from our simulated models considering all LOS for models with $\mathcal{M}_s = 4$ and 7. The PRS when only turbulence is presented on the left. The PRS calculated for the final state of models that consider self-gravity is shown on the right. The Alfvénic Mach number of the models is indicated above each plot.

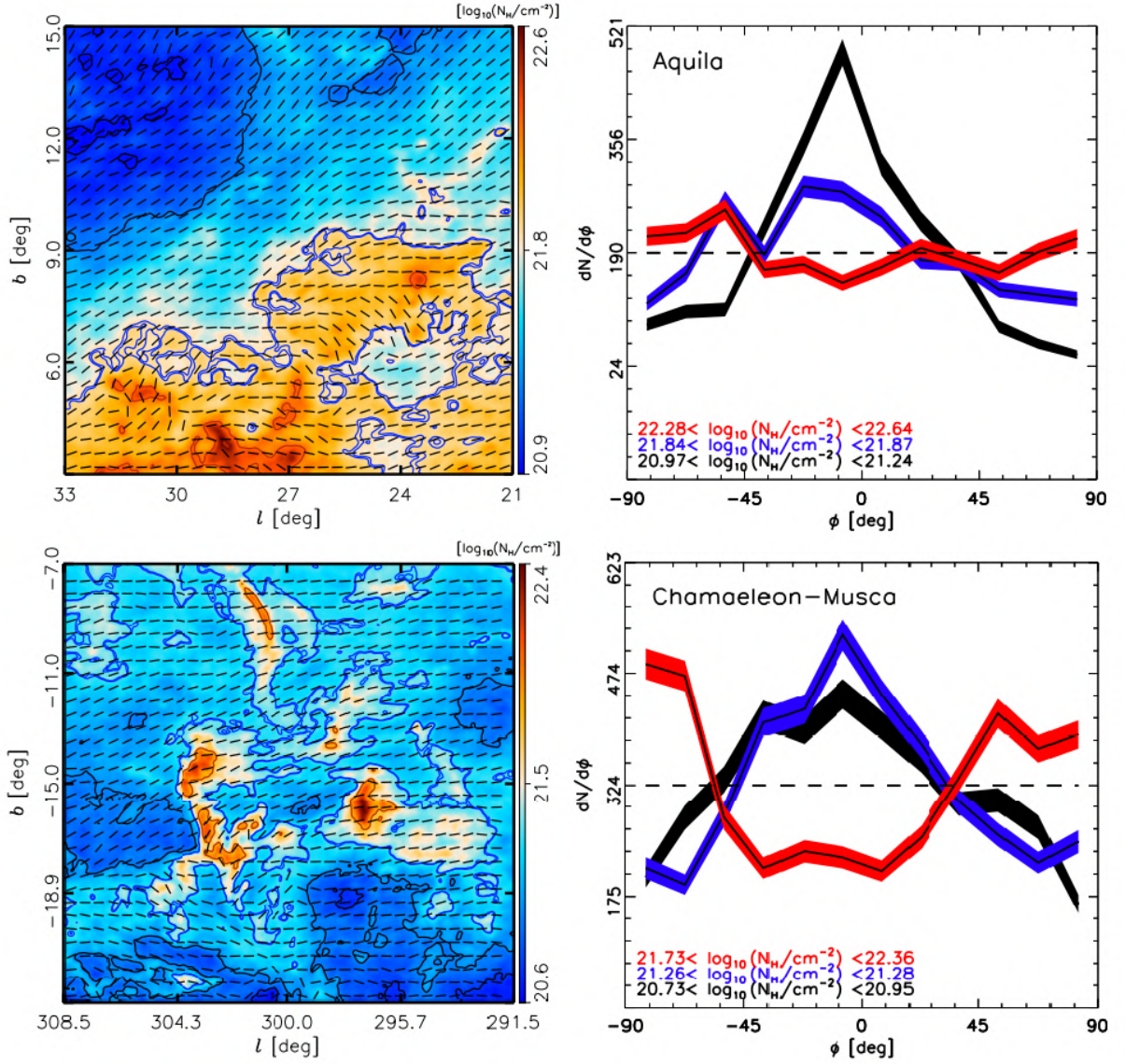


Figure 4.4: Left: Column density maps overlaid with the estimated magnetic field direction estimated from the polarization observations at 353 GHz from *Planck* Satellite from Aquila and Chamaeleon-Musca. Right: Histogram of relative orientations similar to what was presented in Figure 3.20. Extracted from Planck Collaboration et al. (2016).

approximately produce a behaviour of Z_E compatible with the observations. The different regions of Vela C in particular show higher column density values and most of the structures appear perpendicular to the projected magnetic field, since they have a negative tail of Z_E at higher densities. Which is only achieved in the sub-Alfvénic models that consider self-gravity (see Fig. 4.3). Aquila, on the other hand can be described by a sub-Alfvénic model without gravity.

Complementary information is provided in Figures 4.4 and 4.5 that present the ob-

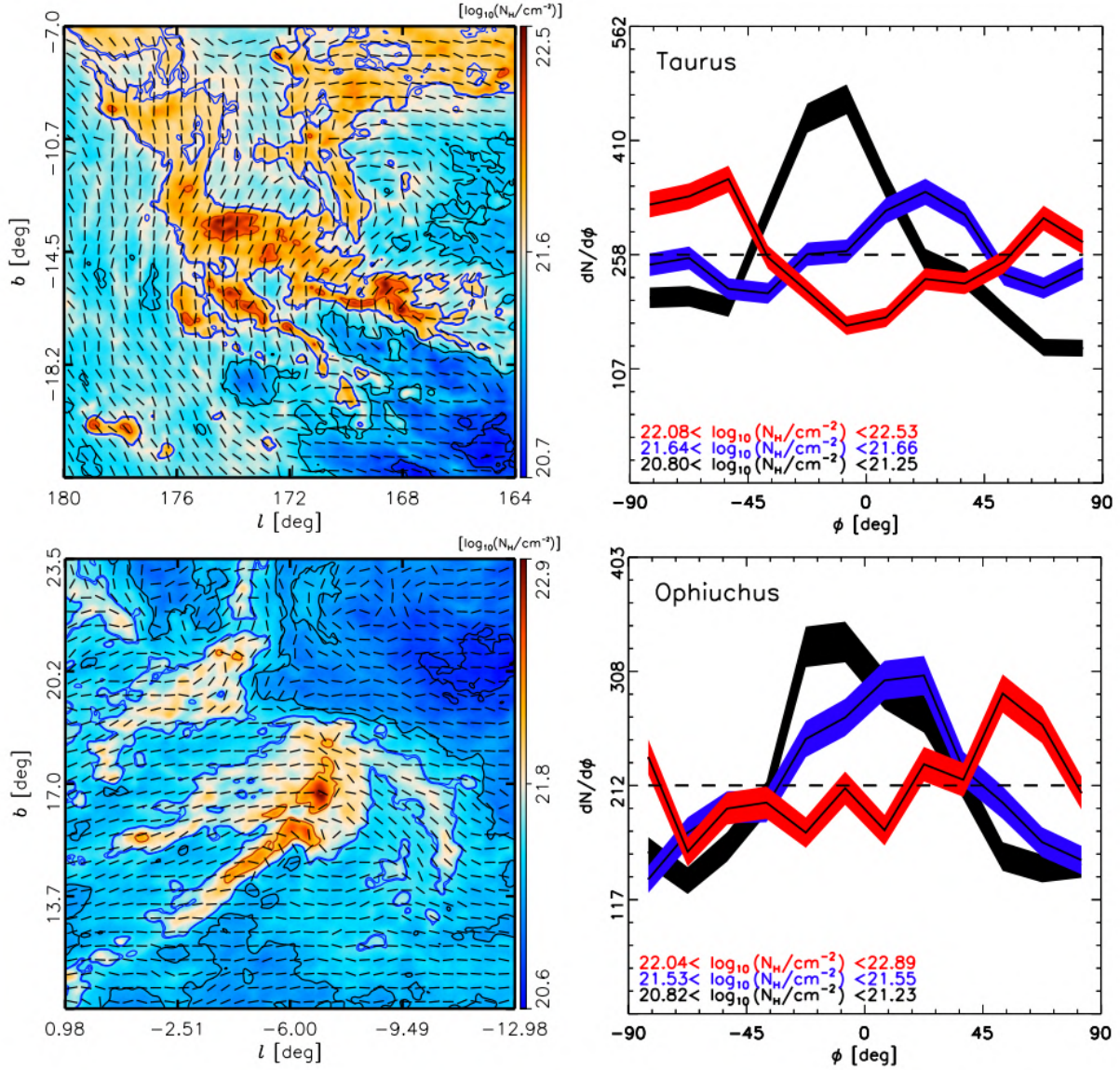


Figure 4.5: Left: Column density maps overlaid with the estimated magnetic field direction estimated from the polarization observations at 353 GHz from *Planck* Satellite from Taurus and Ophiuchus. Right: Histogram of relative orientations similar to what was presented in Figure 3.20. Extracted from Planck Collaboration et al. (2016).

served integrated column densities of the clouds Aquila, Chamaeleon-Musca, Taurus and Ophiuchus on the left side, and the histograms of relative orientations between the projected magnetic fields and the density gradient of the structures in these clouds. Comparing with the histograms of our models in Figure 3.20, we note a similar behaviour with the sub-Alfvénic models, i.e., as we go from less dense to denser structures, the relative orientation between the magnetic field and the filaments goes from aligned to perpendicular, particularly in the case of Chamaeleon-Musca and at some extent Taurus. Note that Fi-

Figure 3.20 shows the HRO applied to the 3D structures and not to column density maps, still the behaviour is similar.

One effect that can also influence the comparison of the PRS from observations with our simulated models is related to the resolution and field of view that is possible to achieve with the telescopes. The size of the clouds in our simulations is 10 pc, while the clouds observed can extend up to hundreds of parsecs. This means that our results are more representative of sub-structures inside the clouds and not so much of the global formation of the cloud and their surroundings. The PRS results reported in Jow et al. (2018) are for entire regions observed by the *Planck satellite*. Even though, our study presents results that are qualitatively comparable to the observations and hence, one can always argue that due to the self-similarity nature of the turbulent clouds, the general behaviour at very large scales does not differ much of that in the intermediate scales inside the clouds, at least in scales where self-gravity is not dominant yet.

To account for the scaling effect above, we may take the self-gravity, sub-Alfvénic simulations with $\mathcal{M}_s = 1.8$. It is important to highlight that due to self-gravity, the units considered in the code are scale dependent. When the Poisson equation is calculated, it actually considers the normalized potential:

$$\nabla^2 \Psi' = \nabla^2 \left(\frac{\Psi}{4\pi G} \right) = \rho \quad (4.1)$$

The normalization implies a gravitational constant in code units as follows:

$$G_{c.u.} = G_N \rho_0 \left(\frac{L}{c_s} \right)^2 \quad (4.2)$$

where G_N is the gravitational constant, ρ_0 is the initial density of the simulation, and L the size of the domain. With this in mind, it is possible to re-scale our models as long as we keep $G_{c.u.}$ the same, i.e. the ratio in the right-hand side of the equation, $\rho_0 \left(\frac{L}{c_s} \right)^2$, must be kept constant.

We consider a region of 40 pc, which is approximately the estimated extension of the observed clouds indicated in Figure 4.1. Considering the same temperature for the re-scaling (10K), the average density in this larger system is around 6 cm^{-3} to keep the ratio $\rho_0 \left(\frac{L}{c_s} \right)^2$ constant. The final result is shown in Figure 4.6.

It is important to highlight that with the re-scaling, the turbulence injection scale may differ from what was considered in our models, but the comparison below is still valid as

a first approximation. In a future work we intend to further explore the findings reported below.

On the left side of Figure 4.6, the original column density and PRS that was extracted from the simulation is shown for the re-scaled system. The integration was made along a direction 45° inclined with respect to the initial magnetic field. On the bottom left diagram of Figure 4.6, the red line is the obtained PRS for from observations of Chamaeleon-Musca (same as in the top diagram of Figure 4.3), and the black line is the PRS calculated for model *Ms1.8-Ma-2.0-grav*. The right-hand side of the figure shows the same column density map of the left, but convolved with a 2D Gaussian kernel (see Soler et al. (2013) for further details). The image has been smoothed to roughly the same spatial resolution of the observations, as it was done by Planck Collaboration et al. (2016). In our simulation, the smoothing length corresponds to about 7 cells. We note that the PRS for the smoothed map is quite different at higher densities, even if the column density is still similar to the original one, thus providing different information. In fact, we see that the PRS calculated for the smoothed map is more similar to the observed one (red curve). Originally, the structures are aligned to the magnetic field for all column densities, but if we take into account the lack of resolution smaller scales of the observations, dense structures actually appear perpendicular to the magnetic field. Both maps may share similarities with Chamaeleon-Musca (Figure 4.4), but the alignment indicated by the PRS in the smoothed map is actually not representative of the real behaviour of the projected magnetic field onto the sky (inferred from the simulations).

4.3 A closer look inside the Molecular Clouds

As discussed in Chapter 1, clouds may form in the WNM where temperature is very high ($\sim 10^4 K$) and the turbulence is subsonic with regard to the hot gas. However, inside molecular clouds, the turbulence is supersonic, with $\mathcal{M}_s \gtrsim 3$. With this in mind, a transition between these two states needs to happen and our simulations with $\mathcal{M}_s = 1.8$ can be reasonable models to compare if we conceive a state where the cloud has started to collapse and the temperature has cooled to around $10K$.

Of course we are limited to an isothermal simulation, which may not be realistic if we think in the scales that these clouds are born, but the analysis from Figure 4.6, which was

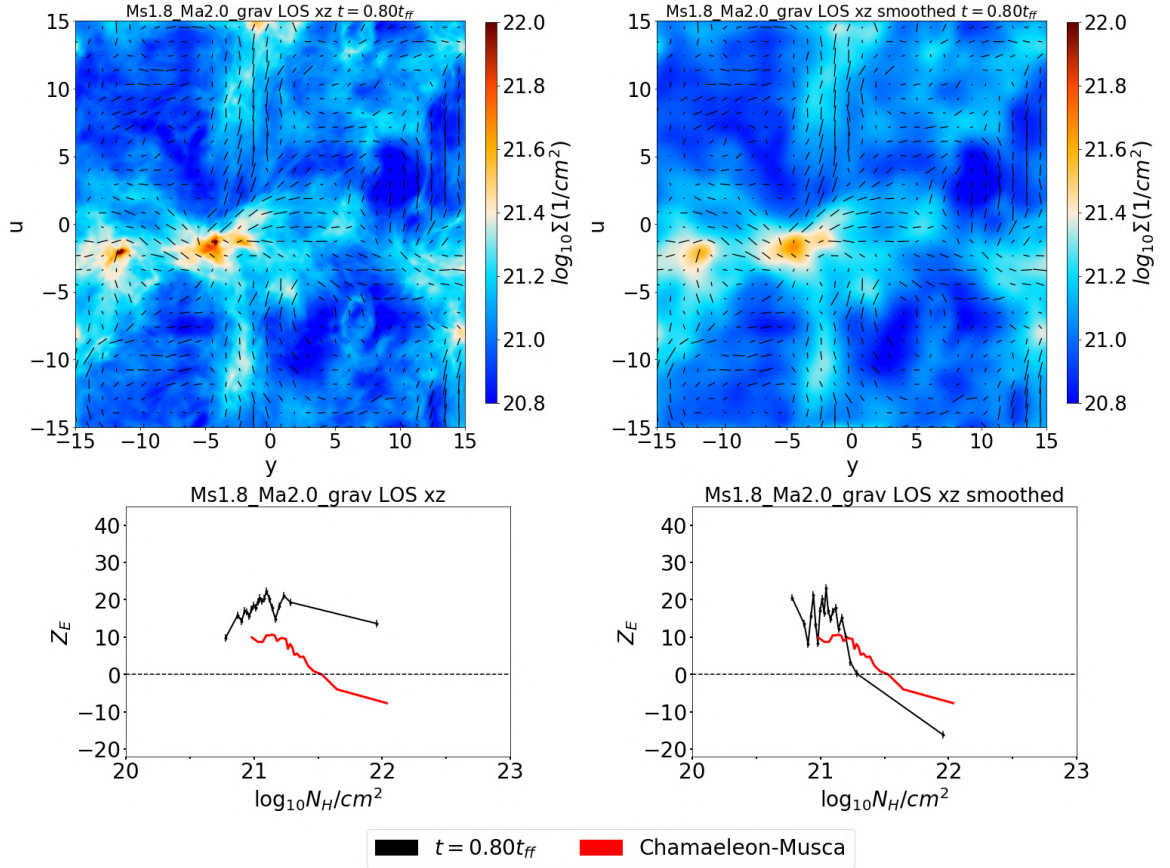


Figure 4.6: Left: Column density map along LOS XZ for our model *Ms1.8-Ma2.0_grav* (top) and the PRS calculated for the respective map (bottom). Right: Same map, but convolved with a Gaussian kernel in a similar processes to the one made for observations from Planck Collaboration et al. (2016) (top) and the PRS of the respective map (bottom) (see also Soler et al. (2013) for further details).

performed to compare with the Chamaeleon-Musca cloud, serves as an illustration of other effects that may influence the results obtained from observations. The similarities seen in the general behaviour of \mathbf{B}_\perp and the formation of larger collapsed regions perpendicular to it, as well as the comparison of the PRS showing a reasonable match in Figure 4.6, can be further explored in a future work. Our models also provide a reasonable description of the evolution inside the cloud.

Observations made by Palmeirim et al. (2013) using *Herschel* Telescope have revealed several smaller structures around the filament B211/3 in Taurus molecular cloud (see Figure 4.7). The dense filament (B211/3) appears perpendicular to the magnetic field around it, while less dense structures (the striations in Figure 4.7) are parallel to the projected magnetic field onto the sky. According to the scale indicated in the Figure, the

size of the region is about $\sim 3 pc \times 4 pc$. The separate regions of Vela C in Figure 4.2 also have similar sizes.

To evaluate the behaviour of these smaller, denser regions, both of Taurus (Figure 4.7) and Vela C (Figure 4.2), Figure 4.8 shows the time evolution of the column density of two regions of similar size to these clouds extracted from our self-gravity models with $\mathcal{M}_s = 7.0$. The density integration was along a LOS making an angle of 45° with respect to the original magnetic field. On the left, we have $\mathcal{M}_A = 0.6$, on the right $\mathcal{M}_A = 2.0$ and the time is indicated on the top of each image. The time considered is indicated above each map. While in the sub-Alfvénic case filaments appear mostly perpendicular to the projected magnetic fields onto the sky, in the super-Alfvénic case they commonly appear aligned with the magnetic fields.

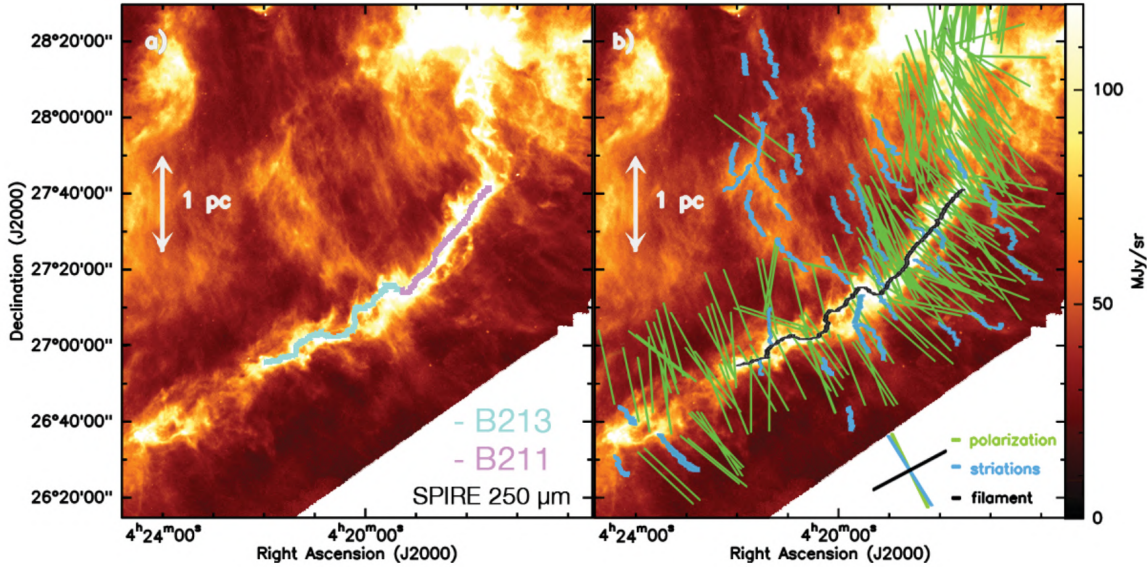


Figure 4.7: *Herschel*/SPIRE 250 μm image of B211/B213/L1495 region in Taurus. On the left-hand side, filaments B211 and B213 are highlighted by the light blue and purple curves. On the right-hand side, the green lines represent the magnetic field direction derived from optical and infrared polarization vectors. Blue curves represents striations, less dense filaments perpendicular to the main filament B211/B213, which is represented by the black line. The diagram on the lower right corner represent the average position of the polarization angles, low-density striations and the main filament, respectively. Extracted from Palmeirim et al. (2013)

In Figure 4.8, initially (at $t = 0.0t_{ff}$), it is possible to see filaments both parallel and perpendicular to the magnetic field in the sub-Alfvénic model. At this time, as only turbulence and magnetic fields are present, the compression motions tend to align the

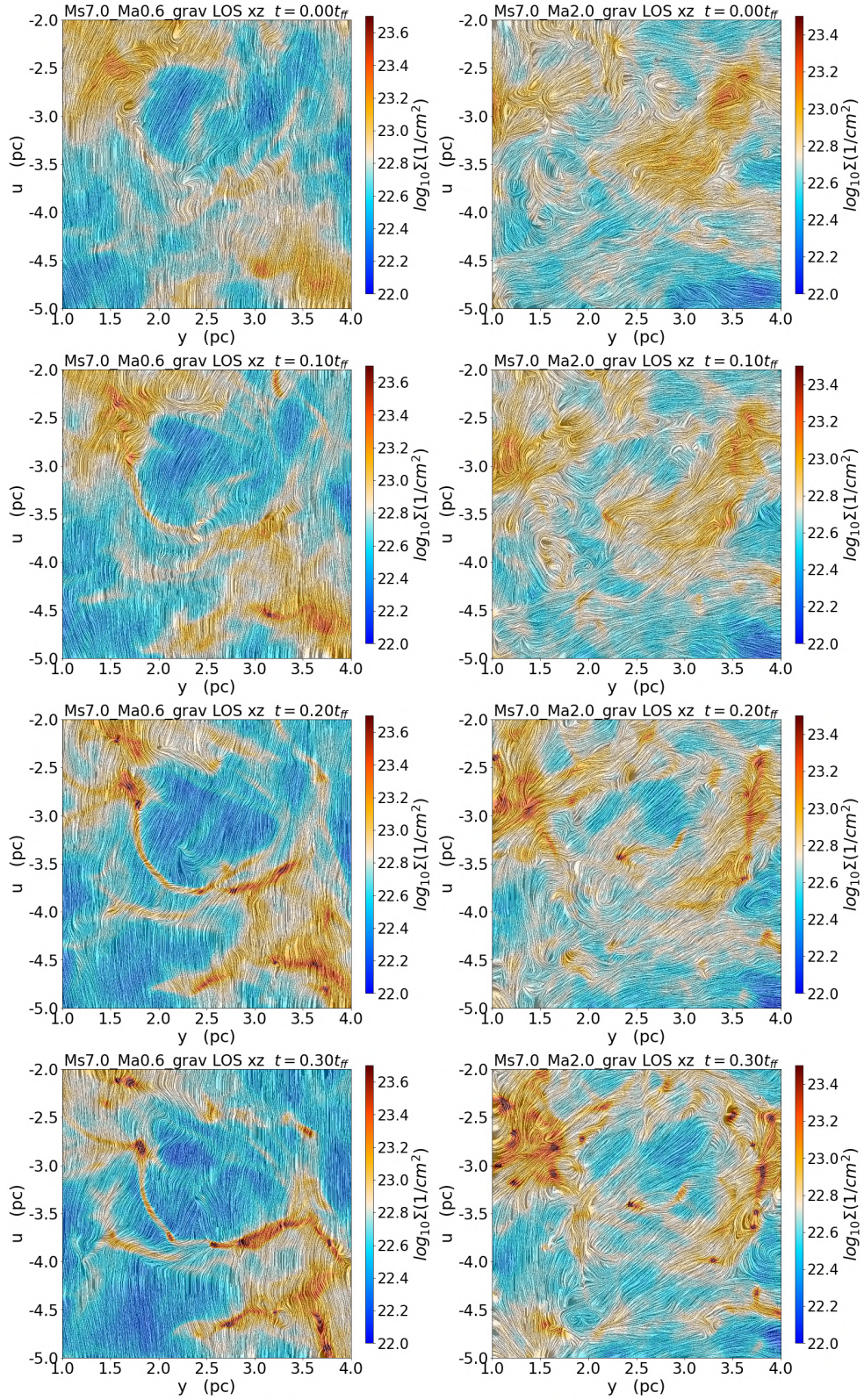


Figure 4.8: Time evolution of zoomed-in regions extracted from models *Ms7.0_Ma0.6_grav* (left) and *Ms7.0_Ma2.0_grav* (right). Both maps were integrated along LOS XZ (45° inclined with respect to the initial magnetic field). The time considered is indicated above each map.

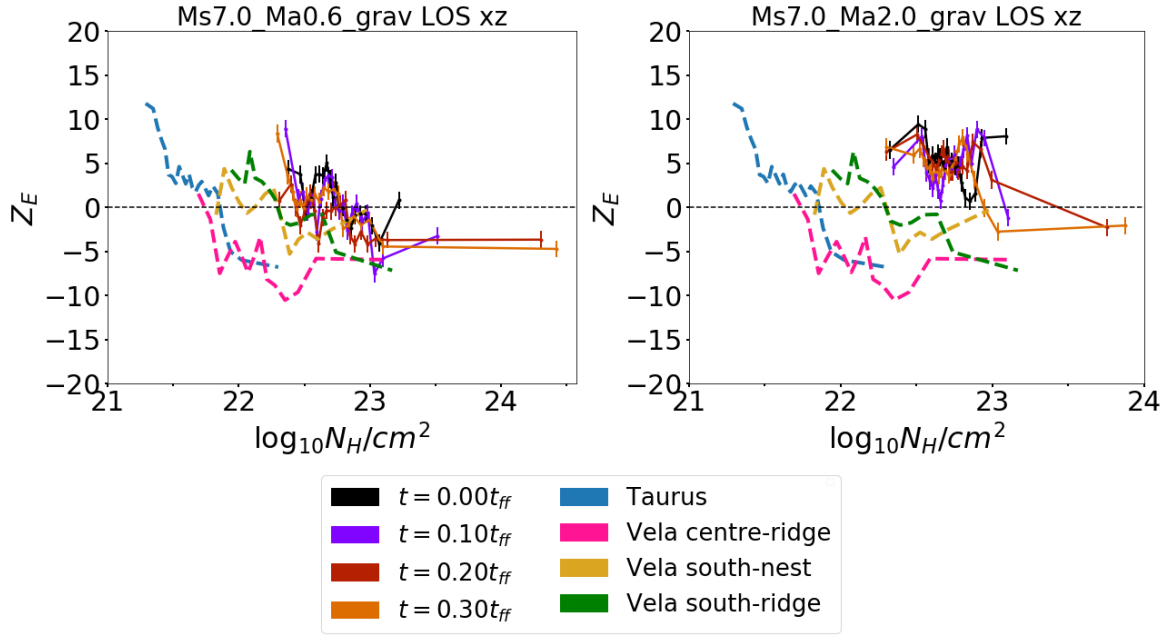


Figure 4.9: Time evolution of the PRS analysis (Z_E , eq. 2.21) for the same maps presented in Figure 4.8. Solid lines represent the PRS along time calculated from our models, sub-Alfvénic on the left-hand side and super-Alfvénic on the right hand side. Dashed lines represent the observed PRS of some regions presented in the top diagram of Figure 4.3.

filaments with the magnetic lines (an effect which is more pronounced in the super-Alfvénic model on the right side of the figure), while the stronger magnetic fields imposed by the sub-Alfvénic regime tend to oppose resistance to alignment, through their tension and pressure gradient forces. As time passes, matter flows along the lines and results in denser filaments perpendicular to the field. In the super-Alfvénic case, the magnetic field is dragged with the flow resulting in projected magnetic fields aligned to the filaments. Along time, it is also possible to see dense regions where the field is perpendicular to the structures, which is evidenced in Figure 4.9 for $t = 0.3t_{ff}$, with $Z_E < 0$ for the highest column densities in both models.

In Figure 4.9, the solid lines show the PRS analysis of the column density maps presented in Figure 4.8. The results for the sub-Alfvénic models are shown on the left-hand side, and the ones for the sub-Alfvénic model are shown on the right-hand side. The dashed lines show the PRS calculated for some of the observations (see top diagram of Figure 4.3) as a comparison.

Once again the distribution of Z_E obtained in our sub-Alfvénic models seems a better representation of what is observed in the sky. Note that the values of Z_E for the

super-Alfvénic case when $t = 0.3t_{ff}$ and several regions have already collapsed, also show negative values for higher column densities, which is expected as discussed in Chapter 3, but the distribution for smaller densities and at previous times is not compatible with the observation. On the other hand, the sub-Alfvénic model shows very similar behaviour when compared to the observation. In particular, the PRS analysis obtained from the sub-Alfvénic model in Figure 4.3 resembles to what is seen in Vela C.

A final remark is in order. Our models were made considering only solenoidal driving turbulence. However as discussed in Chapter 1, compressive modes may change the distribution of the filaments and this may affect the resulting PRS analysis. This will be one of the subjects of forthcoming work.

Conclusions and Future Perspectives

5.1 A summary of our findings

In this work we have performed 3D MHD simulations of MCs aiming at studying the relation between turbulence, magnetic fields and gravity. Our models considered initially homogeneous magnetic field and density ρ_0 in a $10 pc \times 10 pc \times 10 pc$. Two main families of models have been explored, one with self-gravity and one without self-gravity. Turbulence has been driven in the system at an injection scale and allowed to cascade down to the smallest scales, reaching a steady state. For models that considered self-gravity, only after this point gravity was turned-on.

The models considered have initial sonic Mach numbers $\mathcal{M}_s \sim 2.0, 4.0$ and 7.0 , and Alfvénic Mach numbers $\mathcal{M}_A \sim 0.7$, and $\mathcal{M}_A \sim 2.0$. To ensure the gravitational collapse of our clouds when self-gravity is present, we considered an initial density, ρ_0 , such that the turbulent to gravitational energy density ratio is $\alpha_{vir} \sim 0.5$ (eq. 2.12).

We followed the evolution of our simulated models through the density PDF and power spectrum, with our turbulent models with no self-gravity showing a density distribution compatible with a lognormal distribution (eq. 2.7), and a power-spectrum compatible with a Kolmogorov distribution. The PDF of our models with self-gravity show, as structures collapse due to gravity, a power-law distribution for higher densities which becomes shallower over time. The density power-spectrum of the self-gravitating models also deviates from the initial distribution (which is similar to the one seen in the models that do not consider self-gravity), becoming flat over time.

Evaluating the histogram of relative orientations between the magnetic fields and the density gradients (Soler et al. (2013)), and applying the PRS analysis (Jow et al. (2018)) to

our models, we verified that MHD turbulence, to some extent, always creates dense structures perpendicular to the magnetic fields. This is evidenced by an increase in the values of the PRS, Z_B (Figures 3.12 and 3.14), for higher densities, although for super-Alfvénic models this effect is very small. However, the degree at which these structures appear on column density maps depend on the sonic and Alfvénic Mach numbers, as well as on the LOS. For our sub-Alfvénic models without self-gravity, we found that when the LOS is not parallel to the initial magnetic field, and the sonic Mach number is high enough, the PRS for the column density, Z_E , shows higher values for lower column densities (implying a gradient of column density aligned with the polarization vector, i.e., the projected magnetic field onto the plane of sky aligned with filaments) and values near zero or negative for higher densities (implying either no preferential alignment, or the polarization vector perpendicular to the gradient of column density and the projected magnetic field normal to the filaments). When the LOS is parallel to the initial magnetic field or the sonic Mach number is small, the column density structures follow mainly the projected magnetic field. This last result is very similar to super-Alfvénic models without self-gravity, with $Z_E > 0$ for all LOS and all sonic Mach numbers.

When gravity is considered this scenario changes. Gravity enhances the formation of structures perpendicular to the magnetic field at higher densities for all models. In the case of super-Alfvénic models, this effect is more pronounced when the sonic Mach number is higher. For the column density maps, sub-Alfvénic model show $Z_E < 0$ at higher densities for all sonic Mach numbers, and for all LOS, at later times. For super-Alfvénic models, only for $\mathcal{M}_s = 7.0$, smaller values of Z_E are present at higher densities.

In Chapter 4 we have compared the results described above with observations made by *Planck*, *Herschel* and BLASTPol. The comparison indicates that, qualitatively, our sub-Alfvénic models can better reproduce the characteristics of observed clouds. Not only the behaviour of the observed Z_E , but also the general coherence of the magnetic field projected on the plane of the sky (\mathbf{B}_\perp), is compatible with our sub-Alfvénic models for most clouds. There are clouds where twists of \mathbf{B}_\perp could be explained with effects due to LOS. Clouds like Aquila, for instance, can be well represented by models with no self-gravity or in earlier stages of collapse, while Taurus and Vela C have some similarities with the models with a more advanced stage of gravitational collapse.

5.2 Results from previous studies in the literature

Soler et al. (2013) have first analysed the alignment of structures with the magnetic fields in a molecular cloud using statistical tools like those employed in this work. However, in their study turbulence was not constantly driven in the simulated system, and thus was allowed to decay with time. Also, they did not consider sub-Alfvénic models and investigated only a single sonic Mach number. Their highest magnetized model had $\mathcal{M}_A = 3.16$ and $\mathcal{M}_s = 10$, so that they could not investigate most relevant dynamical effects of the magnetic fields in the evolution of star forming systems, as in the present work. Compared to our most similar model, *Ms7.0-Ma2.0-grav*, their results present significant differences. They only consider a LOS perpendicular to the initial magnetic field and find a distribution of Z_E that is closer to our distributions for sub-Alfvénic models. Also, the general coherence of \mathbf{B}_\perp in their column density maps is only observed in our sub-Alfvénic models. This difference is most likely due to the fact that turbulence was not continuously driven. Therefore, as turbulence decays their turbulent regime will approach the sub-Alfvénic regime, with gravity and magnetic pressure becoming the main forces acting over the fluid. Hence, the collapse will primarily occur along the field lines, resulting in dense structures perpendicular to the magnetic field. Turbulence is dominated by the magnetic field and cannot bend the lines, thus explaining why their results are more comparable with our sub-Alfvénic models.

Hull et al. (2017) have also performed 3D MHD simulations in order to study the alignment at smaller scales and compare with observations made by ALMA. As initial conditions, they also consider a single sonic Mach number ($\mathcal{M}_s = 10$), but they do consider different Alfvénic Mach number cases, including a trans-Alfvénic and a sub-Alfvénic one. Their work is complementary to ours, since they focus on regions around collapsed cores, while our results are more representative of the behaviour of larger regions of MCs.

A last remark is in order. More recently Gómez et al. (2018) studied the structure of magnetic fields inside self-gravitating filaments in turbulent environments. They note that the magnetic field around the filament is primarily perpendicular to the structure and the collapse along the filament would later bend the magnetic field lines creating “U”-shapes. However, they argue that the lack of resolution, as well as the decrease of polarization in observations would not be able to detect this. This is compatible with the analysis we

made in Figure 4.6, where the decrease of resolution simulated by the smoothing of the image, changes completely the behaviour observed in the PRS.

5.3 *Future perspectives*

In future works we intend to extend characterization of MCs. Further statistical tools, such as the bispectrum and statistical moments (see Burkhart et al. (2009)), can be applied to our models. As remarked the in Chapter 4, the study of compressive driving turbulence can also be explored, as well as simulations using an adaptive mesh refinement in order to follow further the formation of gravitationally unstable clumps.

Beyond this, Melioli et al. (2006); Leão et al. (2009) and others have previously studied the interaction of supernova remnants (SNR) with MCs. We intend to extend these works by studying the effects of these interactions in small and intermediate scales of the cloud. Clouds like Vela C are known to be associated with SNRs, and in the last decade, besides the usual observations at larger wavelengths, very high energy instruments, like Fermi-LAT satellite, have associated gamma-ray emission with star-forming regions, and its origin is still not well understood. High energy cosmic rays are accelerated in the shock fronts of SNRs and then interact with the local density and magnetic fields, and also with low energy photons, both from the SNRs and also from the surrounding star forming regions, producing gamma-rays. In the near future, the Cherenkov Telescope Array (CTA; Acharya et al. (2013); Cherenkov Telescope Array Consortium et al. (2019)) will be able to explore with much higher resolution and field of view the high-energy emission in these regions. With this in mind, the study of particle acceleration and propagation inside MCs will be important to help in the understanding of the origin of this emission, and it is also our plan to explore this issue.

Bibliography

- Acharya B. S., Actis M., Aghajani T., Agnetta G., Aguilar J., Aharonian F., Ajello M., Akhperjanian A., Alcubierre M., Aleksić J., Alfaro R., Aliu E., Allafort A. J., Allan D., Allekotte I., Amato E., et al., Introducing the CTA concept, *Astroparticle Physics*, 2013, vol. 43, p. 3
- André P., Di Francesco J., Ward-Thompson D., Inutsuka S. I., Pudritz R. E., Pineda J. E., From Filamentary Networks to Dense Cores in Molecular Clouds: Toward a New Paradigm for Star Formation. In *Protostars and Planets VI* , 2014, p. 27
- André P., Men'shchikov A., Bontemps S., Könyves V., Motte et al From filamentary clouds to prestellar cores to the stellar IMF: Initial highlights from the Herschel Gould Belt Survey, *A&A*, 2010, vol. 518, p. L102
- Banerjee R., Vázquez-Semadeni E., Hennebelle P., Klessen R. S., Clump morphology and evolution in MHD simulations of molecular cloud formation, *MNRAS*, 2009, vol. 398, p. 1082
- Bergin E. A., Tafalla M., Cold Dark Clouds: The Initial Conditions for Star Formation, *ARA&A*, 2007, vol. 45, p. 339
- Bergin E. A., Tafalla M., Cold Dark Clouds: The Initial Conditions for Star Formation, *Annual Review of Astronomy and Astrophysics*, 2007, vol. 45, p. 339
- Bertoldi F., McKee C. F., Pressure-confined Clumps in Magnetized Molecular Clouds, *ApJ*, 1992, vol. 395, p. 140
- Bodenheimer P., Laughlin G. P., Rozyczka M., Plewa T., Yorke H. W., Yorke H. W., Numerical methods in astrophysics: an introduction. CRC Press, 2006

- Burgers J., *The nonlinear diffusion equation* (D. Reidel, Dordrecht), 1974
- Burkhart B., *The Star Formation Rate in the Gravoturbulent Interstellar Medium*, *ApJ*, 2018, vol. 863, p. 118
- Burkhart B., Collins D. C., Lazarian A., *Observational Diagnostics of Self-gravitating MHD Turbulence in Giant Molecular Clouds*, *ApJ*, 2015, vol. 808, p. 48
- Burkhart B., Falceta-Gonçalves D., Kowal G., Lazarian A., *Density Studies of MHD Interstellar Turbulence: Statistical Moments, Correlations and Bispectrum*, *ApJ*, 2009, vol. 693, p. 250
- Cabral B., Leedom L. C., , 1993 Technical report *Imaging vector fields using line integral convolution*. Lawrence Livermore National Lab., CA (United States)
- Chepurnov A., Lazarian A., *Extending the Big Power Law in the Sky with Turbulence Spectra from Wisconsin H α Mapper Data*, *ApJ*, 2010, vol. 710, p. 853
- Cherenkov Telescope Array Consortium Acharya B. S., Agudo I., Al Samarai I., Alfaro R., Alfaro J., Alispach C., Alves Batista R., Amans J. P., Amato E., Ambrosi G., et al., *Science with the Cherenkov Telescope Array*, 2019
- Cho J., Lazarian A., *Compressible magnetohydrodynamic turbulence: mode coupling, scaling relations, anisotropy, viscosity-damped regime and astrophysical implications*, *MNRAS*, 2003, vol. 345, p. 325
- de Gouveia Dal Pino E., *Plasmas em Astrofísica. Apostila do Curso*, 1995
- Del Zanna, L. Bucciantini, N. Londrillo, P. *An efficient shock-capturing central-type scheme for multidimensional relativistic flows - II. Magnetohydrodynamics*, *A&A*, 2003, vol. 400, p. 397
- Elmegreen B. G., Scalo J., *Interstellar Turbulence I: Observations and Processes*, *ARA&A*, 2004, vol. 42, p. 211
- Falceta-Gonçalves D., Lazarian A., Kowal G., *Studies of Regular and Random Magnetic Fields in the ISM: Statistics of Polarization Vectors and the Chandrasekhar-Fermi Technique*, *ApJ*, 2008, vol. 679, p. 537

-
- Falceta-Gonçalves D., Bonnell I., Kowal G., Lépine J. R. D., Braga C. A. S., The onset of large-scale turbulence in the interstellar medium of spiral galaxies, *MNRAS*, 2015, vol. 446, p. 973
- Falceta-Gonçalves D., Kowal G., Falgarone E., Chian A. C. L., Turbulence in the interstellar medium, *Nonlinear Processes in Geophysics*, 2014, vol. 21, p. 587
- Federrath C., Klessen R. S., The Star Formation Rate of Turbulent Magnetized Clouds: Comparing Theory, Simulations, and Observations, *ApJ*, 2012, vol. 761, p. 156
- Federrath C., Klessen R. S., On the Star Formation Efficiency of Turbulent Magnetized Clouds, *ApJ*, 2013, vol. 763, p. 51
- Federrath C., Klessen R. S., Schmidt W., The Density Probability Distribution in Compressible Isothermal Turbulence: Solenoidal versus Compressive Forcing, *ApJ*, 2008, vol. 688, p. L79
- Fissel L. M., Ade P. A. R., Angilè F. E., Ashton P., Benton S. J., Devlin M. J., Dober B., Fukui Y., Galitzki N., Gandilo N. N., et al., Balloon-Borne Submillimeter Polarimetry of the Vela C Molecular Cloud: Systematic Dependence of Polarization Fraction on Column Density and Local Polarization-Angle Dispersion, *ApJ*, 2016, vol. 824, p. 134
- Galitzki N., Ade P. A. R., Angilè F. E., Benton S. J., Devlin M. J., Dober B., Fissel L. M., Fukui Y., Gandilo N. N., Klein J., Korotkov A. L., Matthews T. G., Moncelsi L., et al., The Balloon-borne Large Aperture Submillimeter Telescope for Polarimetry-BLASTPol: performance and results from the 2012 Antarctic flight. In *Ground-based and Airborne Telescopes V*, vol. 9145, SPIE, 2014, p. 257
- Gandilo N. N., Ade P. A. R., Angilè F. E., Ashton P., Benton S. J., Devlin M. J., Dober B., Fissel L. M., Fukui Y., Galitzki N., et al., Submillimeter Polarization Spectrum in the Vela C Molecular Cloud, *ApJ*, 2016, vol. 824, p. 84
- Girichidis P., Konstandin L., Whitworth A. P., Klessen R. S., On the Evolution of the Density Probability Density Function in Strongly Self-gravitating Systems, *ApJ*, 2014, vol. 781, p. 91

- Goldreich P., Sridhar S., Toward a theory of interstellar turbulence. 2: Strong alfvénic turbulence, *ApJ*, 1995, vol. 438, p. 763
- Goldreich P., Sridhar S., Magnetohydrodynamic Turbulence Revisited, *ApJ*, 1997, vol. 485, p. 680
- Gómez G. C., Vázquez-Semadeni E., Zamora-Avilés M., The magnetic field structure in molecular cloud filaments, *MNRAS*, 2018, vol. 480, p. 2939
- Guszejnov D., Hopkins P. F., Grudić M. Y., Universal scaling relations in scale-free structure formation, *MNRAS*, 2018, vol. 477, p. 5139
- Hall N., Kowal G., Lazarian A., Cho J., A Comparative Study of Velocity Statistics of Hydrodynamic and Magnetohydrodynamic Turbulence, arXiv e-prints, 2006, pp astro-ph/0611468
- Hennebelle P., On the origin of non-self-gravitating filaments in the ISM, *A&A*, 2013, vol. 556, p. A153
- Hennebelle P., Falgarone E., Turbulent molecular clouds, *A&A Rev.*, 2012, vol. 20, p. 55
- Hennebelle P., Inutsuka S.-i., The role of magnetic field in molecular cloud formation and evolution, arXiv e-prints, 2019
- Hill T., Motte F., Didelon P., Bontemps S., Minier V., Hennemann M., Schneider N., André P., Men'shchikov A., Anderson L. D., Arzoumanian D., et al., Filaments and ridges in Vela C revealed by Herschel: from low-mass to high-mass star-forming sites, *A&A*, 2011, vol. 533, p. A94
- Hull C. L. H., Mocz P., Burkhart B., Goodman A. A., Girart J. M., Cortés P. C., Hernquist L., Springel V., Li Z.-Y., Lai S.-P., Unveiling the Role of the Magnetic Field at the Smallest Scales of Star Formation, *ApJ*, 2017, vol. 842, p. L9
- Iffrig O., Hennebelle P., Structure distribution and turbulence in self-consistently supernova-driven ISM of multiphase magnetized galactic discs, *A&A*, 2017, vol. 604, p. A70

- Jeans J. H., Darwin G. H., I. The stability of a spherical nebula, *Philosophical Transactions of the Royal Society of London. Series A, Containing Papers of a Mathematical or Physical Character*, 1902, vol. 199, p. 1
- Jow D. L., Hill R., Scott D., Soler J. D., Martin P. G., Devlin M. J., Fissel L. M., Poidevin F., An application of an optimal statistic for characterizing relative orientations, *MNRAS*, 2018, vol. 474, p. 1018
- Kirk J. M., Ward-Thompson D., Palmeirim P., André P., Griffin M. J., Hargrave P. J., Könyves V., Bernard J. P., Nutter D. J., et al., First results from the Herschel Gould Belt Survey in Taurus, *MNRAS*, 2013, vol. 432, p. 1424
- Kowal G., Lazarian A., Scaling Relations of Compressible MHD Turbulence, *ApJ*, 2007, vol. 666, p. L69
- Kowal G., Lazarian A., Beresnyak A., Density Fluctuations in MHD Turbulence: Spectra, Intermittency, and Topology, *ApJ*, 2007, vol. 658, p. 423
- Kowal G., Lazarian A., Vishniac E. T., Otmianowska-Mazur K., Numerical Tests of Fast Reconnection in Weakly Stochastic Magnetic Fields, *ApJ*, 2009, vol. 700, p. 63
- Krumholz M. R., McKee C. F., A General Theory of Turbulence-regulated Star Formation, from Spirals to Ultraluminous Infrared Galaxies, *ApJ*, 2005, vol. 630, p. 250
- Landau L. D., Lifshitz E. M., *Fluid mechanics*, 1959
- Lazarian A., Fast Reconnection and Reconnection Diffusion: Implications for Star Formation, *arXiv e-prints*, 2011, p. arXiv:1111.0694
- Lazarian A., Vlahos L., Kowal G., Yan H., Beresnyak A., de Gouveia Dal Pino E. M., Turbulence, Magnetic Reconnection in Turbulent Fluids and Energetic Particle Acceleration, *Space Sci. Rev.*, 2012, vol. 173, p. 557
- Leão M. R. M., de Gouveia Dal Pino E. M., Falceta-Gonçalves D., Melioli C., Geraissate F. G., Local star formation triggered by supernova shocks in magnetized diffuse neutral clouds, *MNRAS*, 2009, vol. 394, p. 157
- Leão M. R. M., de Gouveia Dal Pino E. M., Santos-Lima R., Lazarian A., The Collapse of Turbulent Cores and Reconnection Diffusion, *ApJ*, 2013, vol. 777, p. 46

- Londrillo P., Del Zanna L., High-Order Upwind Schemes for Multidimensional Magnetohydrodynamics, *ApJ*, 2000, vol. 530, p. 508
- Mac Low M. M., de Avillez M. A., Korpi M. J., The Turbulent Interstellar Medium: Insights and Questions from Numerical Models. In *How Does the Galaxy Work?*, vol. 315 of *Astrophysics and Space Science Library*, 2004, p. 339
- McKee C. F., Ostriker E. C., Theory of Star Formation, *Annual Review of Astronomy and Astrophysics*, 2007, vol. 45, p. 565
- Mardia K., Jupp P., Tests of uniformity and tests of goodness-of-fit, *Directional Statistics*. New York: Wiley, 1999, pp 93–118
- Melioli C., de Gouveia Dal Pino E. M., de La Reza R., Raga A., Star formation triggered by SN explosions: an application to the stellar association of β Pictoris, *MNRAS*, 2006, vol. 373, p. 811
- Menon G., Pego R. L., Universality Classes in Burgers Turbulence, *Communications in Mathematical Physics*, 2007, vol. 273, p. 177
- Mestel L., Spitzer L. J., Star formation in magnetic dust clouds, *MNRAS*, 1956, vol. 116, p. 503
- Mouschovias T. C., Static Equilibria of the Interstellar Gas in the Presence of Magnetic and Gravitational Fields: Large-Scale Condensations, *ApJ*, 1974, vol. 192, p. 37
- Myers A. T., Klein R. I., Krumholz M. R., McKee C. F., Star cluster formation in turbulent, magnetized dense clumps with radiative and outflow feedback, *MNRAS*, 2014, vol. 439, p. 3420
- Ntormousi E., Hennebelle P., Core and stellar mass functions in massive collapsing filaments, *A&A*, 2019, vol. 625, p. A82
- Ossenkopf V., Mac Low M. M., Turbulent velocity structure in molecular clouds, *A&A*, 2002, vol. 390, p. 307
- Padoan P., Nordlund Å., The Star Formation Rate of Supersonic Magnetohydrodynamic Turbulence, *ApJ*, 2011, vol. 730, p. 40

-
- Palmeirim P., André P., Kirk J., et al., Herschel view of the Taurus B211/3 filament and striations: evidence of filamentary growth?, *A&A*, 2013, vol. 550, p. A38
- Parker E. N., The Dynamical State of the Interstellar Gas and Field, *ApJ*, 1966, vol. 145, p. 811
- Planck Collaboration Ade P. A. R., Aghanim Planck intermediate results. XXXV. Probing the role of the magnetic field in the formation of structure in molecular clouds, *A&A*, 2016, vol. 586, p. A138
- Powell K. G., Roe P. L., Linde T. J., Gombosi T. I., Zeeuw D. L. D., A Solution-Adaptive Upwind Scheme for Ideal Magnetohydrodynamics, *Journal of Computational Physics*, 1999, vol. 154, p. 284
- Press W. H., Teukolsky S. A., Vetterling W. T., Flannery B. P., *Numerical recipes in C++ : the art of scientific computing*, 2002
- Santos-Lima R., de Gouveia Dal Pino E. M., Lazarian A., The Role of Turbulent Magnetic Reconnection in the Formation of Rotationally Supported Protostellar Disks, *ApJ*, 2012, vol. 747, p. 21
- Santos-Lima R., Lazarian A., de Gouveia Dal Pino E. M., Cho J., Diffusion of Magnetic Field and Removal of Magnetic Flux from Clouds Via Turbulent Reconnection, *ApJ*, 2010, vol. 714, p. 442
- Scalo J., Elmegreen B. G., *Interstellar Turbulence II: Implications and Effects*, *ARA&A*, 2004, vol. 42, p. 275
- Schneider N., André P., Könyves V., Bontemps S., Motte F., Federrath C., Ward-Thompson D., Arzoumanian D., Benedettini M., Bressert E., Didelon P., et al., What Determines the Density Structure of Molecular Clouds? A Case Study of Orion B with Herschel, *ApJ*, 2013, vol. 766, p. L17
- Shu F. H., Adams F. C., Lizano S., *Star formation in molecular clouds: observation and theory.*, *ARA&A*, 1987, vol. 25, p. 23

Soler J. D., Ade P. A. R., Angilè F. E., et al., The relation between the column density structures and the magnetic field orientation in the Vela C molecular complex, *A&A*, 2017, vol. 603, p. A64

Soler J. D., Hennebelle P., What are we learning from the relative orientation between density structures and the magnetic field in molecular clouds?, *A&A*, 2017, vol. 607, p. A2

Soler J. D., Hennebelle P., Martin P. G., Miville-Deschênes M.-A., Netterfield C. B., Fissel L. M., An Imprint of Molecular Cloud Magnetization in the Morphology of the Dust Polarized Emission, *The Astrophysical Journal*, 2013, vol. 774, p. 128

Toro E. F., *Riemann solvers and numerical methods for fluid dynamics: a practical introduction*. Springer Science & Business Media, 2013

Appendix

Appendix A

A.1 Godunov Method

As stressed in Chapter 2, in this work we employ a Godunov based code to integrate the MHD equations (AMUN; Kowal et al. (2009), <https://bitbucket.org/amunteam/amun-code/src/master/>). There are excellent reviews on this numerical method in Bodenheimer et al. (2006) and Toro (2013). Here, we present only a very brief summary.

Equations 2.1 to 2.3 can be compacted in the following form:

$$\frac{\partial \mathbf{U}}{\partial t} + \nabla \cdot \mathcal{F}(\mathbf{U}) = \mathbf{S} \quad (\text{A.1})$$

Where \mathbf{U} , $\mathcal{F}(\mathbf{U})$ and \mathbf{S} are:

$$\mathbf{U} = \begin{bmatrix} \rho \\ \rho \mathbf{v} \\ E \\ \mathbf{B} \end{bmatrix} \quad (\text{A.2})$$

$$\mathcal{F}(\mathbf{U}) = \begin{bmatrix} \rho \mathbf{v} \\ \rho \mathbf{v} \mathbf{v} + (P + \frac{B^2}{8\pi}) \mathbf{I} - \frac{\mathbf{B}\mathbf{B}}{4\pi} \\ (E + P + \frac{B^2}{8\pi}) \mathbf{v} - \frac{\mathbf{v}\cdot\mathbf{B}\mathbf{B}}{4\pi} \\ \mathbf{v}\mathbf{B} - \mathbf{B}\mathbf{v} \end{bmatrix} \quad (\text{A.3})$$

$$\mathbf{S} = \begin{bmatrix} 0 \\ \rho \mathbf{g} + \mathbf{F} \\ \rho \mathbf{g} \mathbf{v} \\ 0 \end{bmatrix} \quad (\text{A.4})$$

\mathbf{U} is the vector of state, that carries the conserved quantities defined in the center of the cells in the domain, \mathbf{F} is the vector of fluxes. The vector of sources, \mathbf{S} , carries the terms that cannot be written in the divergence form.

Integrating eq. A.1 over the volume of a cell in the position i (V_i):

$$\int_{V_i} \frac{\partial \mathbf{U}}{\partial t} dV + \int_{V_i} \nabla \cdot \mathbf{F} dV = \int_{V_i} \mathbf{S} dV \quad (\text{A.5})$$

$$\frac{\partial \mathbf{U}_i}{\partial t} V_i + \oint \mathbf{F} \cdot \hat{\mathbf{n}} dA = \mathbf{S}_i V_i \quad (\text{A.6})$$

where \mathbf{U}_i and \mathbf{S}_i are the average values of \mathbf{U} and \mathbf{S} in the cell, and $\hat{\mathbf{n}}$ is the vector unit normal to the volume of the cell (Powell et al. (1999)). The closed integral is evaluated over the faces of the cell, where a Riemann solver ¹ must be employed due to the interaction of the states in different cells.

Bellow we present a simple example of how a Godunov scheme works. We consider a one-dimensional case (which can be easily extended to three-dimensions) with no sources and therefore, eq. A.1, reduces to:

$$\frac{\partial U}{\partial t} + \frac{\partial \mathcal{F}}{\partial x} = 0 \quad (\text{A.7})$$

We can rewrite eq.A.6 around each cell:

$$\frac{\partial \mathbf{U}_i}{\partial t} = \frac{\mathcal{F}(U(x_{i-1/2}, t)) - \mathcal{F}(U(x_{i+1/2}, t))}{\Delta x} \quad (\text{A.8})$$

¹ Riemann solvers provide solutions to the inter-cell boundary problems. The solver relies on the solutions obtained in each cell in order to obtain the numerical flux of conserved variables through the cell interface (see Toro (2013)).

where the index $i \pm 1/2$ indicates the cell interface and Δx is the size of the cell. If we integrate this equation over time considering an initial time t^n , for t^{n+1} we have:

$$\mathbf{U}_i^{n+1} = \mathbf{U}_i^n + \frac{\Delta t}{\Delta x} [\mathcal{F}_{i+1/2}^n - \mathcal{F}_{i-1/2}^n] \quad (\text{A.9})$$

where $\mathcal{F}_{i\pm 1/2}^n$ are the averaged fluxes in each cell interface. However only the averaged values inside the cells are known. This means that a method of reconstruction is needed to interpolate the center value and allow the calculation of fluxes at the edges. It is also required that the solutions obtained in each interface do not interfere, i.e.:

$$v^{max} \Delta t \leq \frac{1}{2} \Delta x \quad (\text{A.10})$$

where v^{max} is the maximum velocity at which waves resulting from the interaction of the interfaces propagate into the cell. For a complete discussion about this topic we refer to Bodenheimer et al. (2006) and Toro (2013).

A.2 Multigrid Method to solve th Poisson equation

To understand the idea behind the Multigrid method we are using in order to solve the Poisson equation (eq. 2.4) for our self-gravitating models, we describe the example of a two-grid method following (Press et al. (2002)).

Consider a linear elliptic problem:

$$\mathcal{L}u = f \quad (\text{A.11})$$

where \mathcal{L} is a linear elliptic operator and f is the source term. In the case of the Poisson equation we can consider $\mathcal{L} = \nabla^2$, $f = \rho$ and $u = \phi/(4\pi G)$.

Discretizing the system in a grid with size h , our problem can be rewritten:

$$\mathcal{L}_h u_h = f_h \quad (\text{A.12})$$

Writing the approximate solution as \tilde{u}_h and the exact solution as u_h , the *correction* and defect *follow*, respectively:

$$v_h = u_h - \tilde{u}_h \quad (\text{A.13})$$

$$d_h = \mathcal{L}_h \tilde{u}_h - f_h \quad (\text{A.14})$$

The fact that \mathcal{L} is linear implies that the error should follow:

$$\mathcal{L}_h v_h = -d_h \quad (\text{A.15})$$

To solve this equation, we need some approximation so that we can estimate the value of the correction v_h . We can consider a simplified operator $\hat{\mathcal{L}}$ (e.g. the diagonal part of \mathcal{L}_h for a Jacobi iteration). This leads to an approximate solution:

$$\hat{\mathcal{L}} \hat{v} = -d_h \quad (\text{A.16})$$

with:

$$\tilde{u}_h^{new} = \tilde{u}_h + \hat{v}_h \quad (\text{A.17})$$

In the multigrid method, this approximation lies in the idea of finding a relation between our grid of size h with a coarser grid of size $H = 2h$ (for instance). In this alternative approximation we need to choose an appropriate \mathcal{L}_H , so the approximate defect comes from solving the following equation:

$$\mathcal{L}_H v_H = -d_H \quad (\text{A.18})$$

This new grid has less cells than the previous, allowing to solve this equation faster than eq. A.14. When we restrict our defect to a coarser grid, we will use the *restriction*

operator, \mathcal{R} . The inverse process will use the *prolongation operator*, \mathcal{P} . With this, in the coarse grid, the defect is:

$$d_H = \mathcal{R}d_h \quad (\text{A.19})$$

and with this we can find a solution \tilde{v}_H from eq. A.18. Using then the operator \mathcal{P} , we can find the solution in the fine grid:

$$\tilde{v}_h = \mathcal{P}\tilde{v}_H \quad (\text{A.20})$$

Finally, we can calculate the approximation \tilde{u}_h as:

$$\tilde{u}_h^{new} = \tilde{u}_h + \tilde{v}_h \quad (\text{A.21})$$

The full coarse-grid correction consists of:

1. To compute the defect on the fine grid (eq. A.14)
2. To restrict the defect (eq. A.19)
3. To solve eq. A.18 exactly in the coarse grid
4. To interpolate the correction to the fine grid (eq. A.20)
5. To compute the next approximation (eq. A.21)

The complete two-grid method then consists of:

- Computing \bar{u}_h by applying a relaxation method $n_1 \geq 0$ times to \tilde{u}_h
- Applying the coarse-grid correction to obtain \hat{u}_h^{new}
- Computing \tilde{u}_h^{new} by applying a relaxation method $n_2 \geq 0$ times to \bar{u}_h^{new}

We can then extend this idea and apply the coarse-grid correction to grids with $H' = 2H$ and so on. Applying this process several times allows us to achieve the convergence of our problem.

Figure A.1 shows the general structure of the multigrid method. In our models, only V-cycles are used. For further details on this method we refer to (Press et al. (2002)).

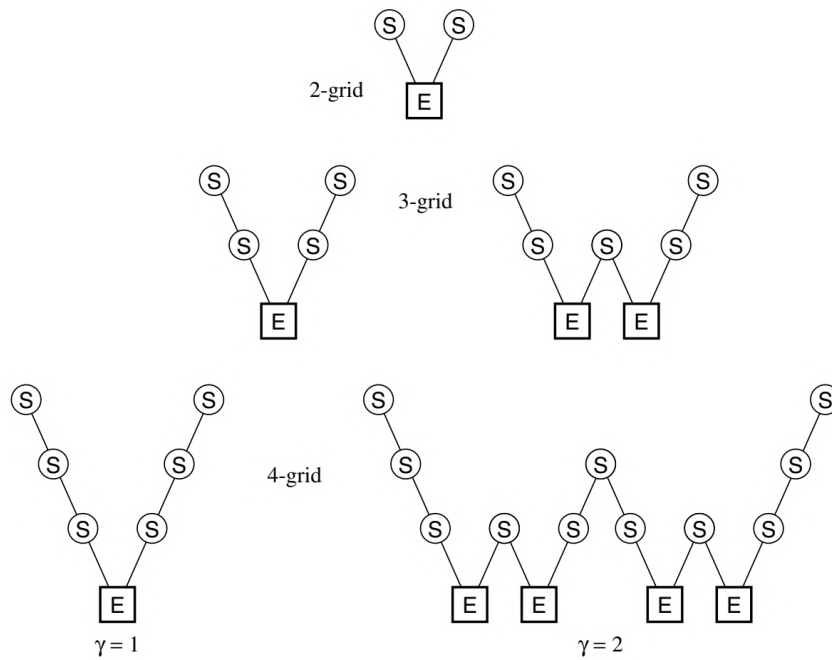


Figure A.1: Multigrid cycle scheme. S denotes the smoothing process, E denotes the exact solution in the coarsest grid. Starting on the left, each line downwards represents a restriction (\mathcal{R}) and each line upwards represents a prolongation (\mathcal{P}). For V-cycles ($\gamma = 1$), E represents one two-grid iteration each time the number of grid levels is increased by one. For the W-cycles ($\gamma = 2$), each E step gets replaced by two two-grid iterations. Extracted from Press et al. (2002).

Appendix B

Other models

In this Appendix we show the results of the PDFs and power spectrum analyses of the other models considered in this work which are not in Chapter 3, see Section 3.1 and Table 2.1 for details.

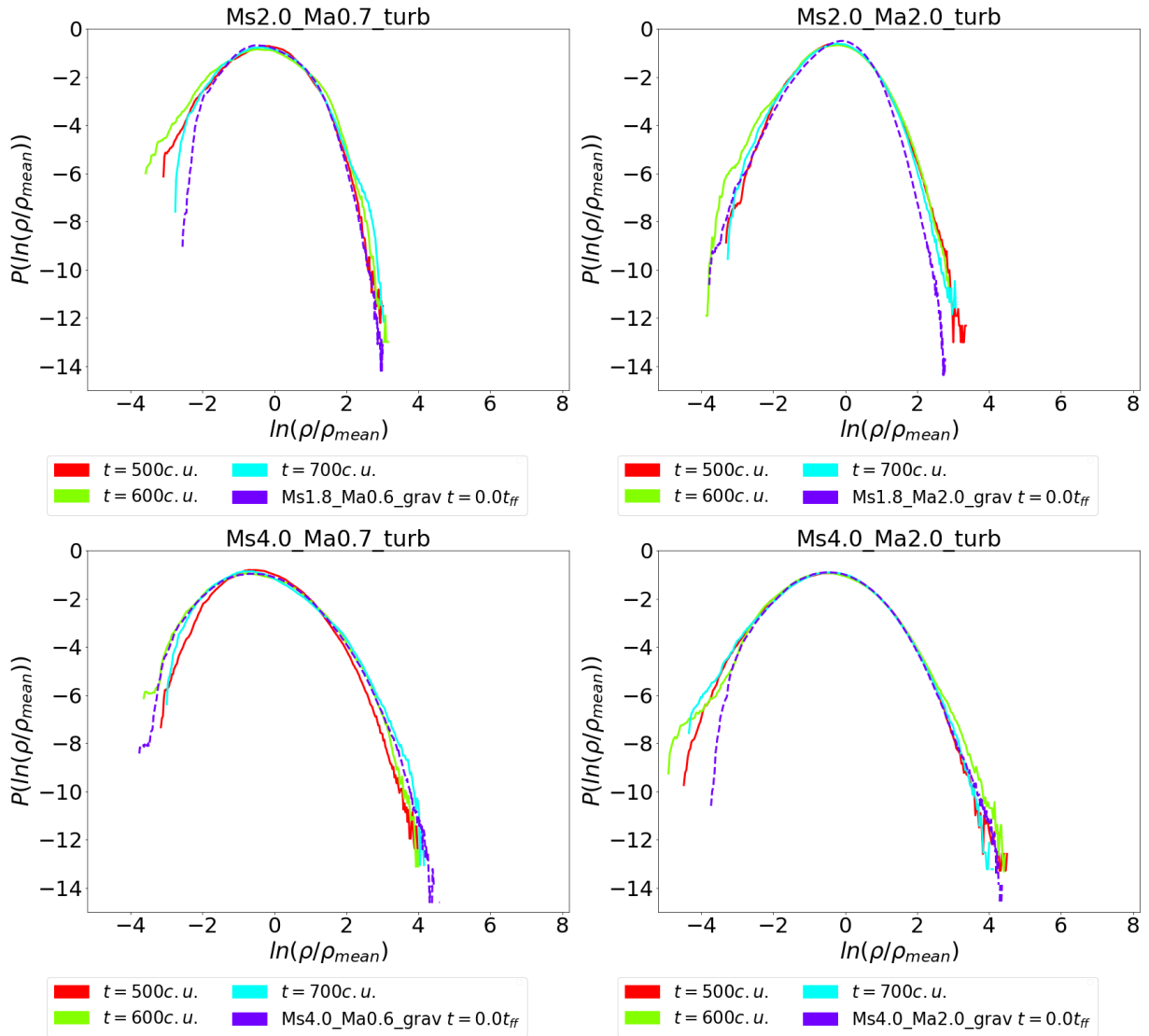


Figure B.1: Comparison of the 3D PDF of density between turbulent models with no self-gravity (solid lines) and the initial state of the corresponding model with self-gravity (dashed line). The sub-Alfvénic models are presented on the left and the super-Alfvénic ones are presented on the right side. Similar to what is presented in Figure 3.3

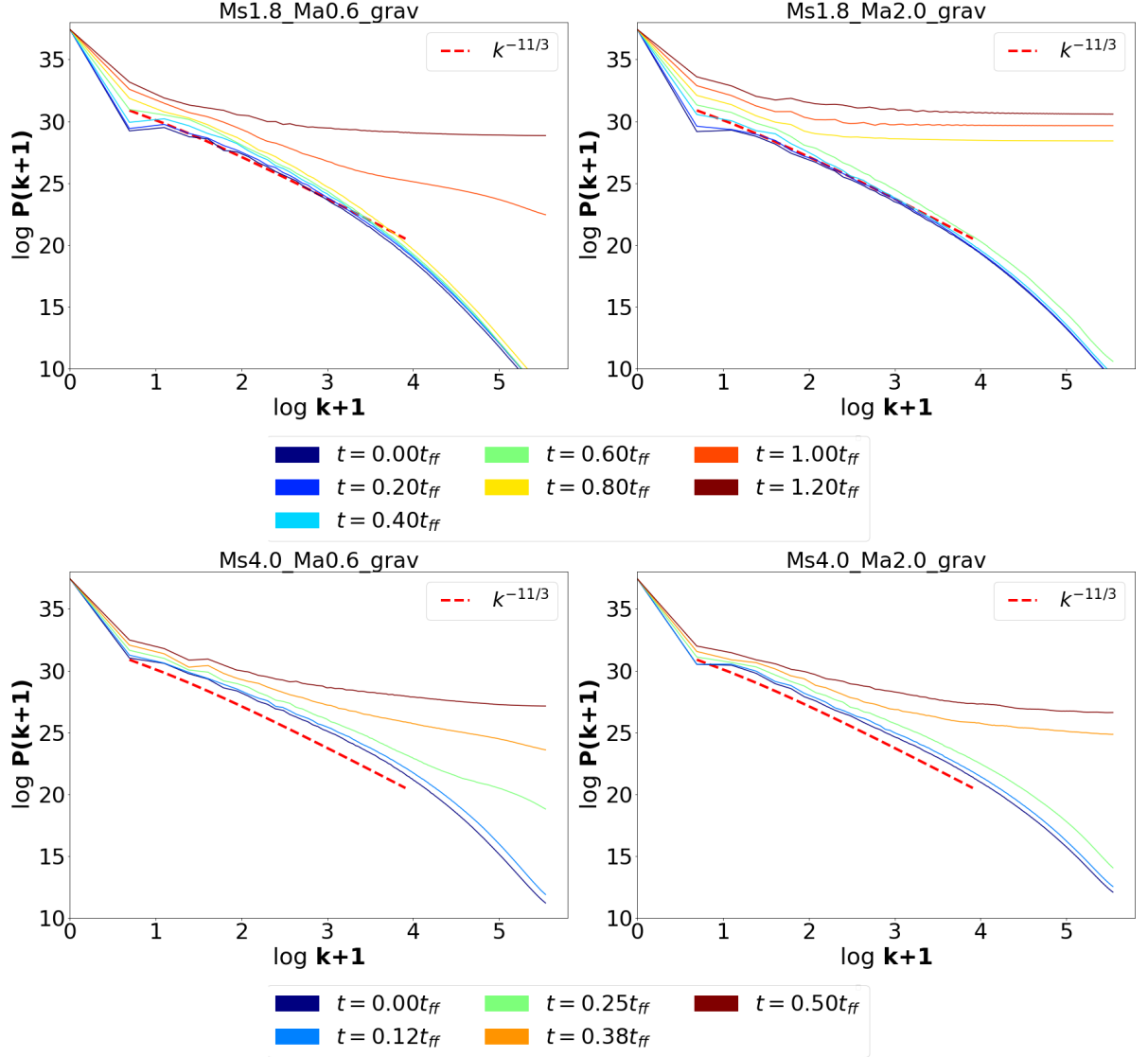


Figure B.2: 3D power spectrum of density for models with $\mathcal{M}_s = 1.8$ and 4.0 that consider self-gravity. On the left we have $\mathcal{M}_a = 0.6$ and on the right we have $\mathcal{M}_a = 2.0$. The red dashed line represents the Kolmogorov power-law ($k^{-11/3}$) for reference. Similar to Figure B.3.

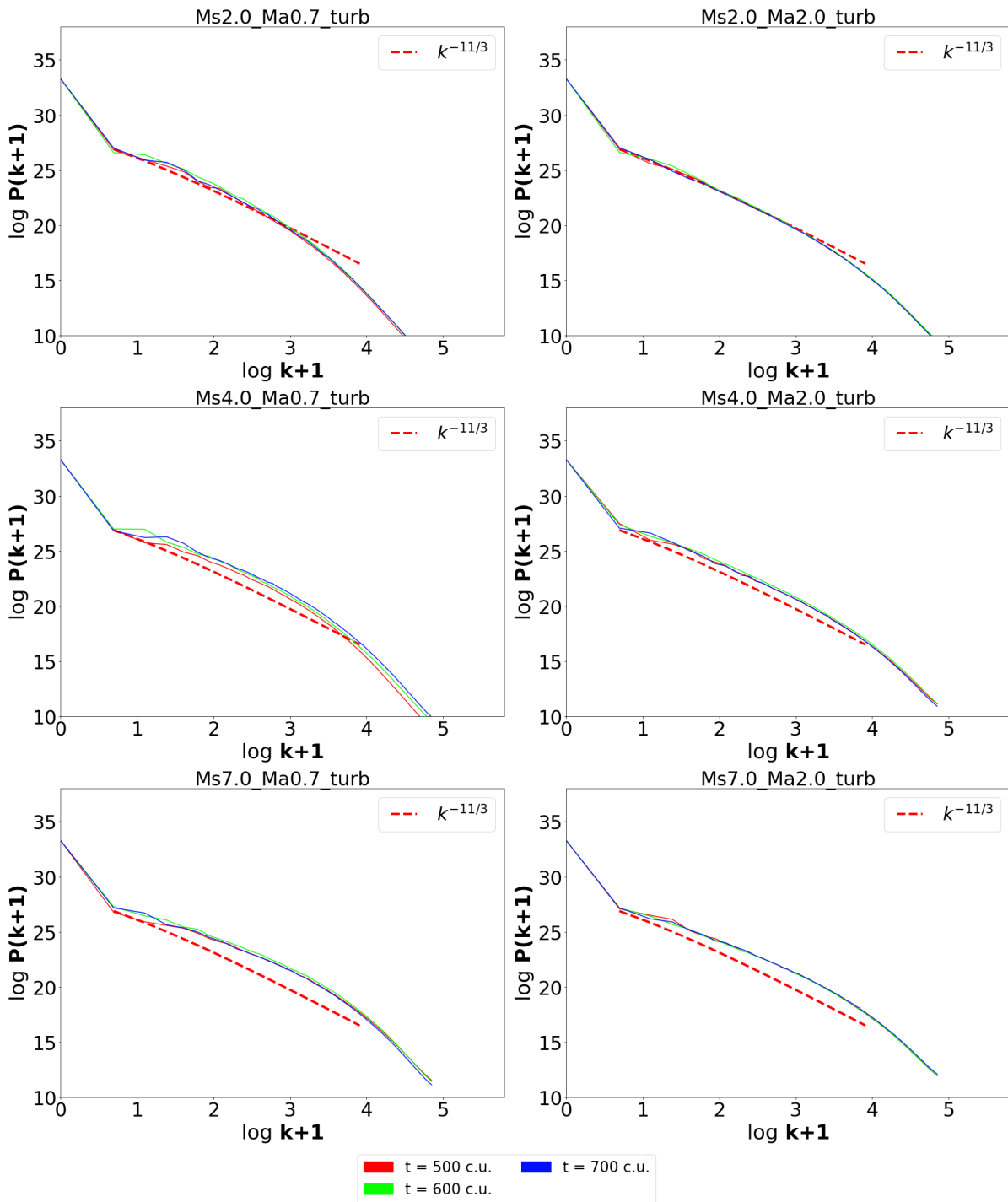


Figure B.3: 3D power spectrum of density for models all the models that do not consider gravity, similar to Figures B.3 and B.2. On the left we have $\mathcal{M}_a = 0.6$ and on the right we have $\mathcal{M}_a = 2.0$. The red dashed line represents the Kolmogorov power-law ($k^{-11/3}$) for reference.